UNIVERSIDAD **NACIONAL** DE COLOMBIA

On the Generation of Subphotospheric Acoustic Sources

Angel Daniel Martínez Cifuentes

Universidad Nacional de Colombia
Observatorio Astronómico Nacional
Facultad de Ciencias
Bogotá, Colombia
2021

On the Generation of Subphotospheric Acoustic Sources

Angel Daniel Martínez Cifuentes

Tesis presentada como requisito parcial para optar al título de:
Magíster en Ciencias Astronomía

Director:
Prof. Benjamín Calvo-Mozo
Observatorio Astronómico Nacional, Colombia
Co-Director:
Ph.D. Juan Carlos Martínez Oliveros
Space Sciences Laboratory- University of California, Berkeley

Línea de Investigación:
Atrofísica Solar
Grupo de Investigación:
Astronomía, Astrofísica y Cosmología
COL0007041

Universidad Nacional de Colombia
Observatorio Astronómico Nacional
Facultad de Ciencias
Bogotá, Colombia

2021

Thesis Committee

Referees

Dr. Dominik Utz
University of South Bohemia
České Budějovice, Czech Republic

Dr. Santiago Vargas Domínguez
Observatorio Astronómico Nacional
Universidad Nacional de Colombia
Bogotá, Colombia

Chair of thesis

Dr. Eduard Larrañaga
Observatorio Astronómico Nacional
Universidad Nacional de Colombia
Bogotá, Colombia

(A mi familia)

Agradecimientos

En esta sección quiero agradecer a quienes de forma directa o indirecta me han apoyado en el proceso de la realización de la tesis.

La vida y la familia están primero ante todo y tengo la fortuna de que la vida me haya brindado una sustancial. Quiero expresar mi infinito agradecimiento a mis papás y mi hermana, de quienes puedo decir que no solo son familia de sangre, sino también de corazón. Todo el apoyo emocional en esta etapa ha sido incondicional aún en situaciones de las cuales pensaba que la solución no era posible.

Doy gracias al profesor Benjamín por decidir acompañarme en este proceso, no solamente en la maestría ni únicamente a nivel académico, sino porque a través de sus charlas he aprendido a ver de una forma más amplia el sentido de la vida. En mi forma de pensar es muy complicado admirar y apreciar al mismo tiempo a una persona, un lugar que sin embargo el profe ocupa.

A Juan Carlos, mi codirector de tesis, quien hace que con sus aportes específicos y únicos pero sustanciales se aclaren los temas más complicados. De él he aprendido a ver el mundo académico desde una perspectiva diferente y más amplia a la que jamás pude haberme imaginado.

Quisiera agradecer a dos egresados quienes con sus aportes puntuales hicieron posible que se pudiese llevar a cabo varias partes este trabajo: a Sebastián Castellanos, Sebas y a Juan Camilo Buitrago, Milo, personas que admiro y que han sido parte de la cantera del GoSA que hoy está alrededor del mundo.

Al doctor Charles Lindsey, Charlie, cuya paciencia, dedicación y emoción hicieron posible que se pudiese dar inicio a esta investigación.

A toda la comunidad OAN, en especial a Islena, a Willy, Sebas Lozano y Andrés Rincón, a la señora Luz Marina, al grupo de profesores, y a los que encuentran y hacen del Observatorio un lugar único en la Universidad. Al grupo de investigación, GoSA, del cual hago parte desde ya varios años y al que le tengo cariño. En mi recuerdo siempre llevo que los momentos académicos de mayor alegría los he pasado siendo parte de él.

Resumen

Sobre la Generación de Fuentes Acústicas Subfotosféricas

Este trabajo exploró la posibilidad de generación de señales sísmicas en el Sol a partir de un confinamiento de energía localizado en el interior solar. Esta idea se desarrolló a través de dos secciones. En la primera sección, correspondiente a la parte observacional, se aplicó la técnica de heliosismología holográfica computacional a series de mapas de velocidad fotosféricos. Los resultados se contrastaron con observables físicos de la superficie del Sol. Los datos analizados correspondieron a imágenes de la intensidad del continuo y del campo magnético y de velocidades en la línea de la visual. Las imágenes fueron obtenidas con el instrumento HMI a bordo del observatorio SDO, cuyos datos de ciencia brindan mediciones del disco solar completo en la línea de absorción Fe-I a 6173.3 Å con una resolución espacial de 0.504" por píxel y una cadencia temporal de 45 s. Con este método, encontramos señales acústicas a altas frecuencias que se extienden más allá de 10 mHz. Dichos resultados permiten tener una mejor discriminación de la morfología espacial de transientes acústicos. Ahora bien, teniendo en cuenta la técnica de enfoque-desenfoque en holografía computacional, fue posible analizar dichas señales ultra-impulsivas a diferentes profundidades en el interior solar. Descubrimos que las señales que se observan no están confinadas estrictamente a la superficie solar sino que tienen un grado de extensión vertical en la región activa.

En la segunda parte se desarrolló una simulación magnetohidrodinámica en 2 y 3 dimensiones. En dicho esquema numérico se perturbó la estructura magnética inmersa en un modelo solar del interior. Encontramos que perturbaciones localizadas a diferentes profundidades son capaces de generar señales sísmicas que pueden ser detectadas en la superficie, reforzando la hipótesis planteada en la sección observacional.

Dichos resultados abren la posibilidad a una rama de estudio más profunda dentro de la heliosismología, la cual involucra la generación de señales acústicas en eventos de fulguraciones solares. Esto permitiría entender mejor los procesos que se llevan a cabo en el interior solar así como su relación con la generación de señales acústicas, un misterio que permanece todavía en la astrofísica solar.

Palabras clave: Física solar, Fulguraciones solares, Heliosismología, Interior solar, Magnetohidrodinámica.

Abstract

On the Generation of Subphotospheric Acoustic Sources

This work explored the possibility of the generation of seismic signals on the Sun from a confinement of energy located in the solar interior. This idea was developed through two sections. In the first section, corresponding to the observational part, the computational heliseismic holographic technique was applied to a series of photospheric velocity maps. The results obtained were contrasted with physical observables in the surface of the Sun. The analyzed data corresponded to images of the intensity of the continuum and of the line of sight magnetic and of velocity fields. The images were obtained with the HMI instrument on board the SDO spacecraft, which provides measurements of the entire solar disk at the 6173.3 Å Fe-I absorption line with a spatial resolution of 0.503" and a cadence of 45 s. With this method, we found acoustic signals at high frequencies extending beyond 10 mHz. These results allow to have a better discrimination of the spatial morphology of acoustic transients. On the other hand, taking into account the focus-defocus technique in computational holography, it was possible to analyze these ultra-impulsive signals at different depths in the solar interior. We discovered that these signals are not strictly confined to the solar surface but have a significant degree of vertical extension in the active region.

In the second part, a magnetohydrodynamic simulation in 2 and 3 dimensions was developed. In this numerical scheme the magnetic structure immersed in a solar model of the interior was disturbed. We found that disturbances located at different depths are capable of generating seismic signals that can be detected on the surface, reinforcing the hypothesis raised in the observational section.

These results open new prospects in helioseismology, which involves the generation of acoustic signals in solar flare events. This would allow a better understanding of the processes that take place in the solar interior as well as their relationship with the generation of acoustic signals, a mystery that still remains in solar astrophysics.

Keywords: Solar physics, Solar flares, Helioseismology, Solar interior, Magnetohydrodynamics.

Contents

1. Introduction

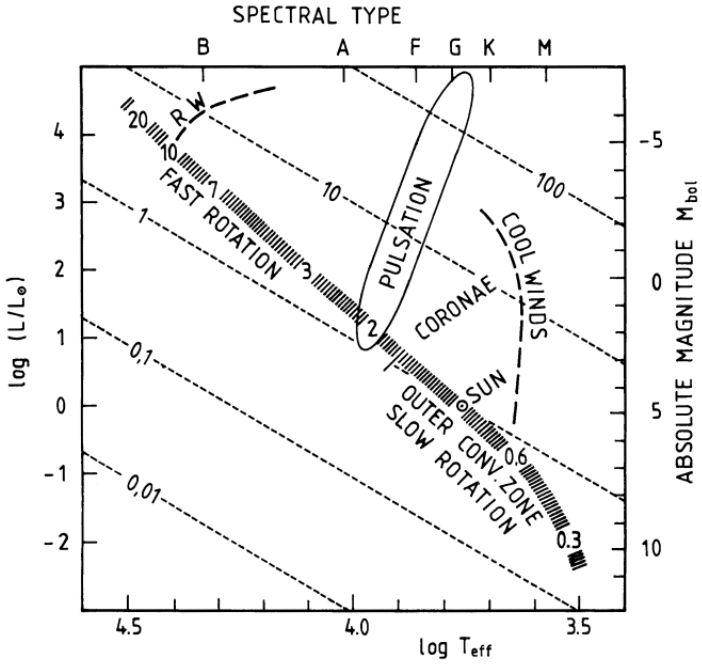

Figure **1-1**.: Hertzsprung-Russell diagram. The Sun is placed according to its effective Temperature and the Luminosity. It is cataloged as a G2V star.

Among the many stars in the universe, the Sun is the most important of all. It is the closest to Earth, influencing the evolution of life and the rise and development of societies and cultures up to the present day. According to the Harvard spectral classification, the Sun is classified as a G2 yellow dwarf with an estimated age of 4600 Myr, which is half of its average life. Among its stellar parameters, are the effective temperature with a value of 5780 K, a luminosity of 3.82×10^{26} W, and a color index $B - V$ of 0.66. Figure 1-1 shows the location of the Sun in a HR diagram. The main energy production of hydrogen fusion into helium is given by the proton - proton chain, accounting for the 99% of total energy production in the solar core. The other 1% corresponds to the carbon - nitrogen - oxygen cycle, CNO cycle (Bahcall et al., 2005). As the Sun is located *only* at 1.5×10^8 km (the next star, α Centaury, is at a distance of 3.7×10^{13} km) it becomes a great laboratory to study not only solar, but stellar physics, magnifying the importance to studying our host star.

Although there are no direct mechanisms to observe the solar interior, scientists use theoretical models and observations under some assumptions to estimate the composition and

distribution of matter along the radius. The actual solar model solves the equations of stellar structure considering a star with spherical symmetry in hydrostatic equilibrium, whose whole configuration at some age is determined by its radial-dependent mass, luminosity and radius.

There are 5 main layers of the internal solar structure: the *core* whose density, pressure, and temperatures reaches values of $\rho = 160$ g/cm^3, $p = 2.70 \times 10^{17}$ dyn/cm^2, $T_c = 1.5 \times 10^7$ K respectively (Stix, 2004). This provides the necessary conditions to favour the proton - proton and CNO chains. This is the inner part of the Sun extending up to 0.25 $R_\odot$, and is where almost all of the energy of the Sun is generated. The *radiative zone* is a region where the energy transport occurs mainly by radiative diffusion rather than convection, extending from 0.25 to 0.7 $R_\odot$. Although the density decreases to ~ 10 g/cm^3, it is still sufficiently high to keep the mean free path, *mfp*, of photons small. This leads to consecutive emissions and absorptions of photons at the same temperature along the mfp, resulting in a situation of Local Thermodynamical Equilibrium, LTE. In the *convection zone*, the energy is transported both by radiation and convection. In this region, a fluid parcel rises from the bottom of the convective zone upwards, reaching an environment with lower temperature. This causes the parcel to cool down, so that its density is increased compared to the surroundings resulting in a posterior descend of material. These are referred as convection currents. Between the radiative and convective zones, there is a transition layer of ~ 0.05 $R_\odot$ called the *tachocline*. The large shear marks the region where the Sun ceases to rotate like a rigid body to have differential rotation. The *photosphere* is the last visible layer of the Sun. It is the most inner shell where light is radiated, defined though its optical depth $\tau(5000\text{Å}) = 2/3$, within a 300 km thickness, and with an effective temperature of 5777 K (see Eddington relation Mullan, 2009). The magnetic field in this region can be manifested, among others, as *sunspots*. These are regions of large magnetic flux concentrations ($\sim 10^3$ G) where the temperature decreases down to 4000 K.

In the solar atmosphere above the photosphere, the temperature, density and pressure decrease in a few hundred km to then increase up to 35000 K in a region called the *chromosphere*. It extends 2000 km in height from the photosphere, and opposite to the photosphere, feature spectral emission lines, with Hα being the most prominent one. The *transition region* is the region located above the chromosphere, where there is a sudden increase in temperature from tens of thousands to a few million of Kelvin. As the density decreases, the dynamics is fully described with magnetohydrodynamics, rather than fluid mechanics. The upper region of the solar atmosphere, the *corona*, extends several million km from the solar surface, maintaining a temperature of 10^6 K. It has been of great interest to describe the process by which the temperature rises up to the corona, a widely known phenomena called the coronal heating problem (see Pontin and Hornig, 2020, and references therein).

The solar atmosphere is host of impulsive processes releasing huge amounts of energy towards the solar interior as well as to the interplanetary medium. These are known as *solar flares*

whose impulsiveness can even affect communications on Earth.

1.1. Impulsive solar events: Solar flares

Solar flares are energetic events with occurrence on the solar atmosphere. These could be represented as a brightening across the electromagnetic spectrum, with time scales varying from minutes to hours. Figure **1-2** displays a solar flare right before the maximum energy release. The first solar flare ever recorded date from September 1, 1859 at 11:18UT (SOL1859-09-01T11:18[1]) by R. C. Carrington and independently by R. Hodgson (Carrington, 1859).

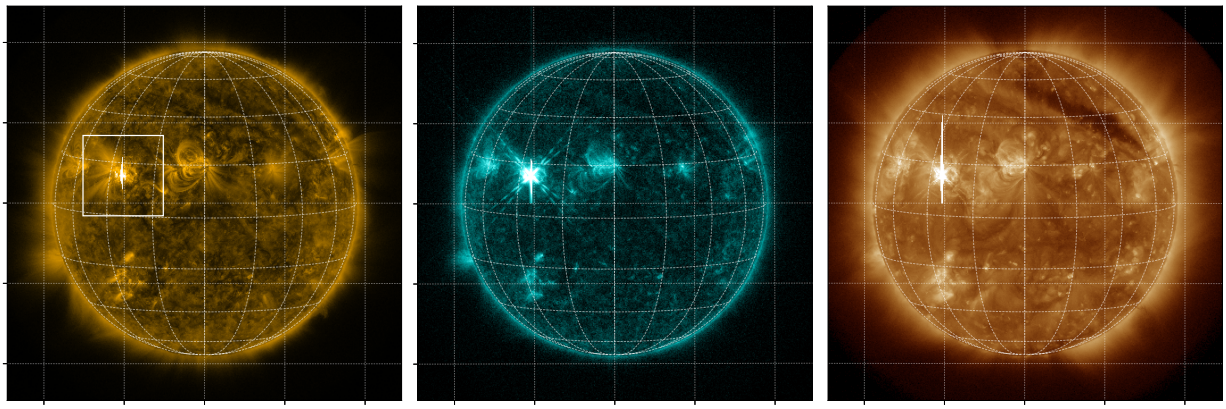

Figure **1-2**.: Solar flare event of SOL2011-07-30 at 02:08:45. A conspicuous increase in brightness is seen from the flaring region in the square of the left side, which manifests also in the middle and left panel. The images are related to three specific filters from the SDO/AIA instrument (see section 3.1), at 171, 131, and 193 Å.

Coronal X-Ray and radio emissions from flaring regions suggests that the energy source of solar flares comes from the magnetic field stored in coronal loops. The energy outputs depend on both the flare duration and its spatial extent ($10^4 - 10^5$ km); as the magnetic energy density, in CGS units, is $\varepsilon_{mag} = B^2/8\pi$, then an estimate of the energy stored on a typical region of length L, is $E_{mag} \simeq (B^2/8\pi)L^3 \simeq 10^{33}(B/10^3\ \mathrm{G})^2(L/10^9\ \mathrm{cm})^3$ erg, resulting in a classical energy release of $\sim 10^{32}$ erg (as a comparison, the total energy supply of Earth in 2017 was 9.71 Gtoe $\sim 10^{27}$ ergs). Other energy resources from different contributions are the gravitational $\varepsilon_{grav} = m_p ngh$, the thermal $\varepsilon_{thermal} = nkT$, and the kinetic $\varepsilon_{kinetic} = nm_p v^2/2$ (see Schrijver and Siscoe, 2010). However, they only account for a small fraction of the energy density required for a solar flare.

[1] (Leibacher et al., 2010). This is a standard notation for the identification of solar flare events and will be used along the document.

The process of energy release from the magnetic field is called *magnetic reconnection*. The magnetic reconnection aligns the magnetic field lines so that they exhibit an X shape configuration. This configuration heats the plasma up to 10^7 K, thus accelerating particles. Under specific conditions, a solar flare can be accompanied by a plasma release into the interstellar space. This "eruption" is known as a Coronal Mass Ejection (CME), and although its nature is also magnetic, there is no clear cause/consequence relationship with a solar flare.

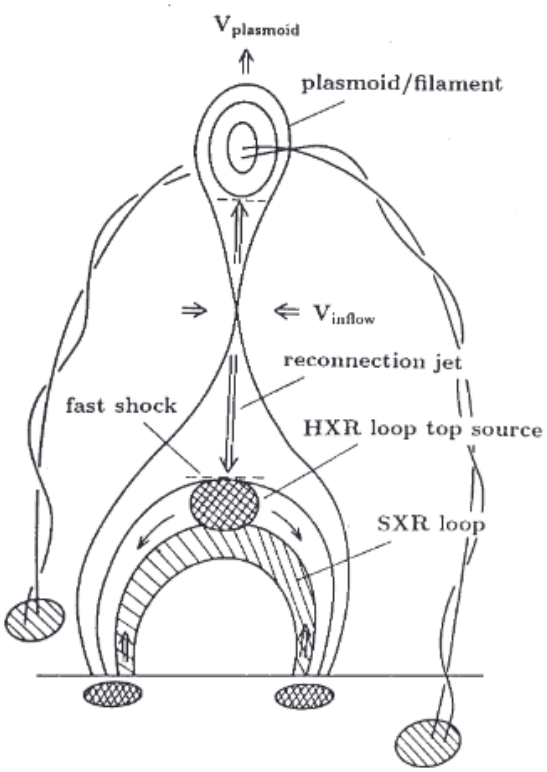

Figure **1-3**.: Basic schematic view of a solar flare in a modern CSHKP model. The energy release takes place in the "X" point, where the particles are thereafter transported in the flare loops towards lower regions of the solar atmosphere. Image taken from (Shibata and Magara, 2011).

The current model that describes the formation of flare loops as well as the scenario for the magnetic reconnection is the *CSHKP* model (also referred as *Classical Two Ribbon Flare Model*), named after Carmichael (1964), Sturrock (1966), Hirayama (1974), and Kopp and Pneuman (1976). In the CSHKP model, the flare is represented by a two-dimensional geometry, and refers to a magnetic reconnection process due to current sheets above a closed loop (see Shibata, 1999). With the improvements of observations, new features are added to the CSHKP model. An example of this is the addition of plasmoid ejections after observations of X-Ray plasmoid ejections in solar flares, which play an important role in the reconnection process (Shibata and Magara, 2011). A schematic view of the model is shown in **1-3**.

In the temporal evolution of solar flares, four main *phases* can be distinguished. Each phase

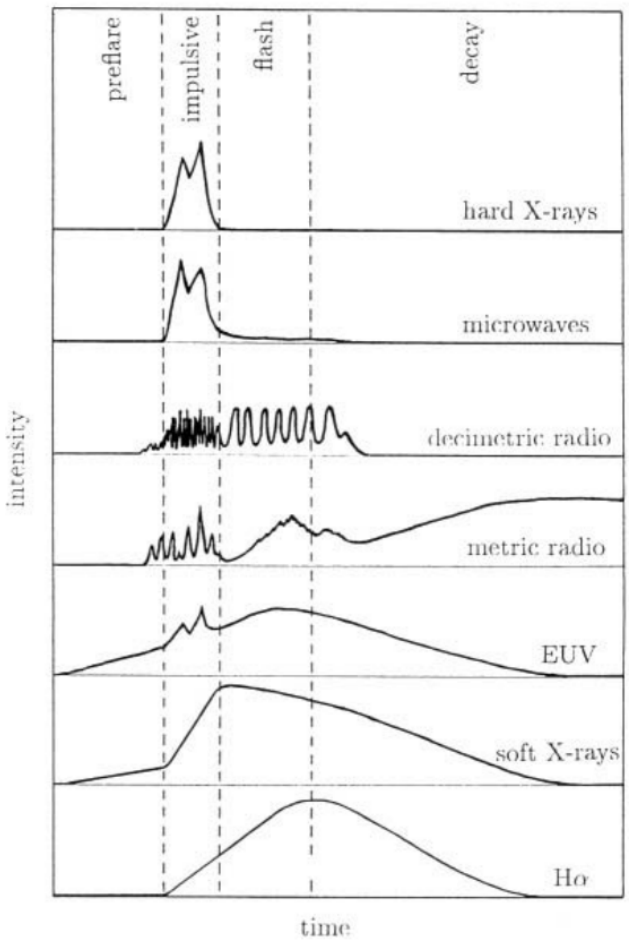

Figure **1-4**.: Temporal evolution of solar flares. A notorious increase in a wide range of the spectrum is seen from the impulsive phase, which marks the beginning of the solar flare. Image taken from Benz (2017).

marks a radiation increase in specific wavelengths. Figure **1-4** shows the time of every radiation release associated to the flare progression. It is usual to identify four main phases of a solar flare. The *preflare* phase, where there is an enhancement in soft X-Rays and EUV radiation. This increase refers to a gradual heating of coronal plasma. The energy is also gradually stored in the magnetic field, until a disruptive mechanism releases the energy. This destabilization marks the beginning of the *impulsive* phase. As the energy stored in the corona is set free, there is a sudden increase in all wavelengths. Given the amount of energy available in the flare loop, particle collisions are dominant and the energy spectrum is mainly due to *Bremsstrahlung* radiation. This collisions produce photons of energies of $10-20$ keV, increasing Hard X-Ray radiation (HXR). In the same way, ions could be accelerated along the magnetic field lines and interact in a similar way electrons do, giving rise to $\gamma-$rays radiation. On post impulsive phases, there is a manifest increase in Hα intensity, while the radio band emissions are a manifest of energetic particles trapped in post - flare loops (*fash*

phase). Finally, the magnetic field structure in the corona returns to its original state in the *decay phase*, where remaining particles are still accelerated through the interplanetary medium (Benz, 2017).

To classify solar flare events, the Solar X-ray Imager (SXI) onboard *Geostationary Operational Environmental Satellite* (GOES[2]), measures the coronal intensity in X-Rays in the spectral range $(1-8)$ Å (Table **1-1**). It uses a logarithmic scale, with letters A, B, C, M, and X for its identification, spanning across flare energetics. To identify a specific event within a class, this classification is subdivided in nine sub categories ranging from 1.0 to 9.9. For example, Figure **1-2** corresponds to a solar flare of class M9.3, with a corresponding flux peak of 9.3×10^{-4} W m^{-1}. The most powerful event registered from the past 24$^{\text{th}}$ solar cycle was an X9.3 flare, SOL2017-09-06 T12:02.

Table **1-1**.: GOES classification for solar flares according to its intensity peak flux in the band of $(1-8)$Å. X-Class flares have the largest intensity, and have the lowest probability to occur.

Class	Flux peak $(1-8)$ Å [W m^{-2}]
X	$I \geq 10^{-4}$
M	$10^{-5} \leq I < 10^{-4}$
C	$10^{-6} \leq I < 10^{-5}$
B	$10^{-7} \leq I < 10^{-6}$
A	$I < 10^{-7}$

1.1.1. Solar flare effects

Solar flares release energy and particles into the solar interior and atmosphere manifesting various solar phenomena which can be detected by ground and space instruments. Among the several signatures, waves induced by flare events are of particular interest. These are products of the restructuring coronal magnetic fields, inducing radiation. Among these atmospheric signatures are Type II Bursts, Chromospheric Waves, and EIT and Moreton waves. Along MHD simulations, these set the base of HMD coronal seismology (see Nakariakov, 2006).

Solar flares could also affect the solar interior in the form of *seismic waves* (see Section 2.1.3). These were predicted by Wolff (1972), and thus creating the field of *helioseismology*, oscillations in the Sun. Although the Sun is the nearest star to us, it is not the only one known to oscillate. Shapley (1914) noticed that for a polytropic Lame-Emden sphere, the oscillation period of a Cepheid varies as $T \sim (R^3/M)^{1/2}$, being T approximately the dynamical time scale. This leads to the study of *asteroseismology*, the study of interior of stars measuring its oscillation signatures.

[2]see www.swpc.noaa.gov.

1.2. Asteroseismology

In 1926, Sir Arthur Eddington (Eddington, 1926) stated that the interior of stars were one of the most difficult regions to study in space. Given the theory of radiative transfer (see Chandrasekhar, 1960), it *is* true that light could be either scattered or absorbed when passing through a medium. Then, when we measure light coming from a source passing through media, we observe a different amount of intensity; if the medium is *optically thick* ($\tau \gg 1$), then all the initial (direct) light is absorbed and none of the intensity could escape shine to be registered by the observational instruments.

However, although the interior of stars is *opaque* to conventional measurements of light or other electro-magnetic wave emission, theoretical models along with stellar surface observations can be used to calculate its oscillations. The study of oscillations in stars is the scope of asteroseismology. These oscillations represent primarily *p-modes*, a sound wave driven by pressure that propagates through the stellar interior up to the surface. Since the oscillations are sensitive to different parts of the star, with proper mode identifications it is possible to render a model of its interior (see Gough (1985), Christensen-Dalsgaard (2002) and the review of Aerts et al. (2010)) with wide applications in the solar context (e.g. Basu (2016) and Christensen-Dalsgaard et al. (1985)).

The sound waves propagate at the sound speed, $c^2 = \Gamma_1 p/\rho$, so, in principle, with calculating the sound speed throughout the star (along with an equation of state), it could be possible to determine interior parameters. Nevertheless, there are not only waves driven by pressure, but also by buoyancy (g - modes), and the surface gravity modes (f - modes), which will be discussed later in this section.

1.2.1. 3-D Stellar Oscillations

By linearly perturbing the equations of state of stellar structure, taking into account spherical symmetry, the solutions for a variable x can be represented as a superposition of eigenmodes:

$$\xi_x(r,\theta,\phi,t) = \sum_{n,l} \sum_{m=-l}^{l} f_{x,n}(r)\ g_x\big(Y_l^m(\theta,\phi)\big)\ \exp[-i2\pi\nu t] \tag{1-1}$$

where $f_{x,n}(r)$ represents the amplitude of the oscillatory variable, g_x is a function of the spherical harmonics $Y_l^m(\theta,\phi)$, and ν is the cyclic frequency of oscillation. As to identify oscillatory modes, given a 3 dimensional geometry, a total of three quantum numbers are required: the radial number n specifying the number of radial nodes, the degree order l accounting for the number of surface nodes, and the azimuthal number m, where $|m|$ is the number of modes along the equator. A simple example radial mode, with $l = 0$, would correspond to spherically symmetric contraction and expansion, leading changes in

luminosity and temperature. This would be similar in nature to Cepheids. In fact, this is a primarily oscillation mode for these variable stars. A similar example of non radial modes, $l, n \geq 1$, pulsate the star in dipole $l = 1$, quadrupole $l = 2$ or even octupole modes $l = 3$.

If p-mode waves are non radial (i.e. not directly along the radius), then thermodynamical differences at the base and the top of the wave will cause to have gradients in the sound speed. As a consequence, this results in a refraction of the wave back to the surface. It is precisely this refraction (and posterior reflection in the surface), that allows to study the structure of the star. Figure **1-5** shows a diagram of the cyclic frequency as a function of the quantum degree number l. For p-modes, the higher the l number is, the shallower will be the refraction. Thus waves with smaller l will penetrate deeper in the star contrary to large l modes. On the other hand, g-mode waves are trapped for Sun-like stars in the interior, thus it is difficult to detect them.

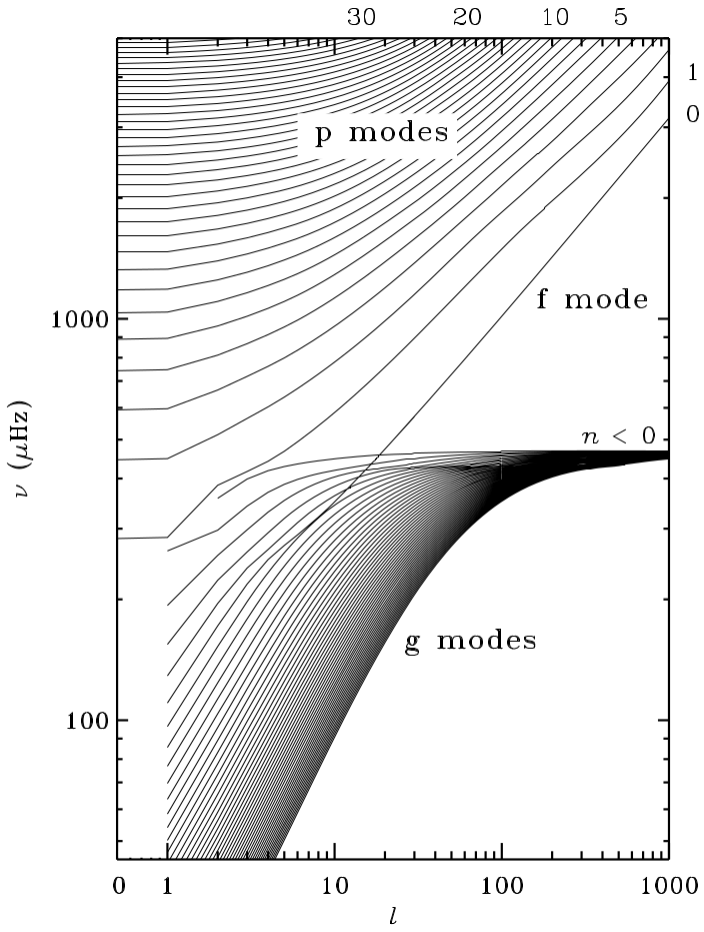

Figure **1-5**.: Cyclic frequency as a function of the degree quantum number for a Sun-like star. For p-modes, the frequency increases as the radial number increase (top right). g-mode waves have a frequency limit and are trapped inside the star. Image taken from Aerts et al. (2010). Note there are no radial resonant modes for g-modes.

In order to compute the characteristic oscillation frequencies, the Fourier formalism is applied on a time series of Doppler images. This gives rise to the oscillation power density spectrum. Figure 1-6 shows the power spectrum of the Doppler solar surface integrated over the solar disk. There is a characteristic *predominant* frequency around 3000 μHz. In temporal terms, this has a corresponding time period of $\sim$ 5 min, known as the 5 minute oscillation of the Sun. This a frequency to consider when performing analysis in solar active regions. Many times a usual Gaussian mask is applied to remove the action of these frequencies on the investigated solar dynamics.

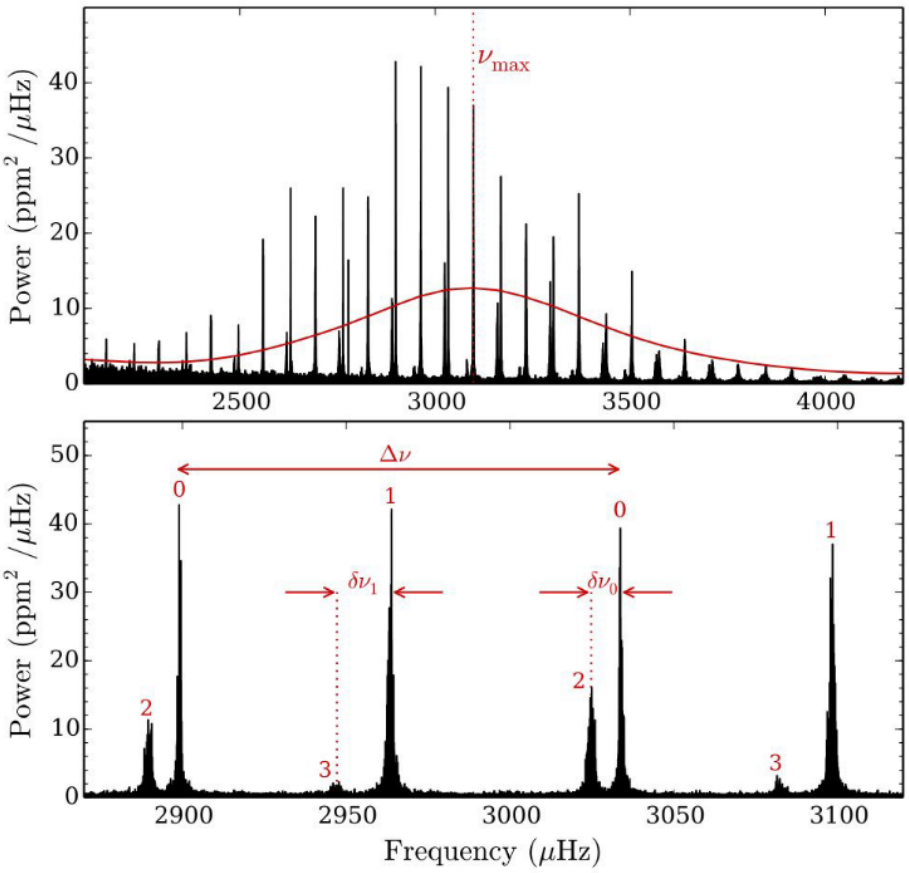

Figure **1-6**.: Solar power density spectrum. At the top, the power density spans from 2000 to 4250 μHz, showing a Gaussian fit showing the most characteristic frequency. The bottom panel shows a close look around the peak, placing different frequency separations. The integration time as well as the instruments by which the image was taken can be found at Figure 1, Cunha (2018).

An asymptotic theory is developed to compute the frequencies, and thus eigenfunctions, of the perturbed equations. Tassoul (1980) found the following expression for the frequency of p-modes (for large radial orders n):

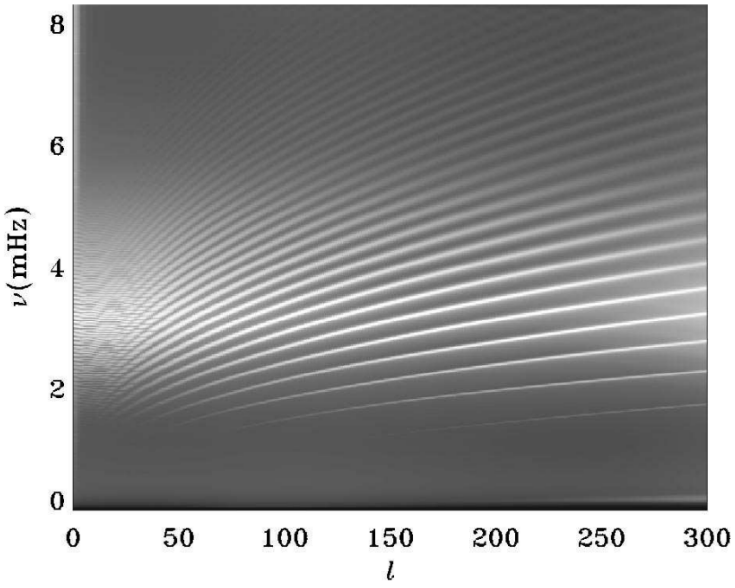

Figure **1-7**.: Acoustic power as a function of cyclic frequency and the degree quantum number l averaged over azimuthal number m. Image from Lindsey (2017).

$$\nu_{nl} \approx 2\pi\Delta\nu_0\left(n + \frac{l}{2} + \frac{1}{4} + \alpha\right) \tag{1-2}$$

where

$$\Delta\nu_0 = \left[2\int_0^R \frac{dr}{c(r)}\right]^{-1} \tag{1-3}$$

which represents the inverse of twice the time for a p-mode wave to travel from the surface to the core. The *large separation* of two frequency peaks is defined as the difference of p-mode waves of successive radial order n,

$$\Delta_{n,l} = \nu_{n+1,l} - \nu_{n,l}$$

while the *small separation* at first order is defined as:

$$\delta n, l = \nu_{n,l} - \nu_{n-1,l+2}$$

These two separations can be visualized on the bottom panel of figure **1-6**. Figure **1-7** shows a Fourier-analyzed plot of the solar oscillations for averaged m number of tracked Doppler images over the disk center. Each of the rings represent an order n of oscillations.

In the next chapter, we describe how asteroseismolgy applied to the solar case can help us to understand more about the solar interior by measuring the spatial and temporal progression of waves on its surface.

2. Helioseismology

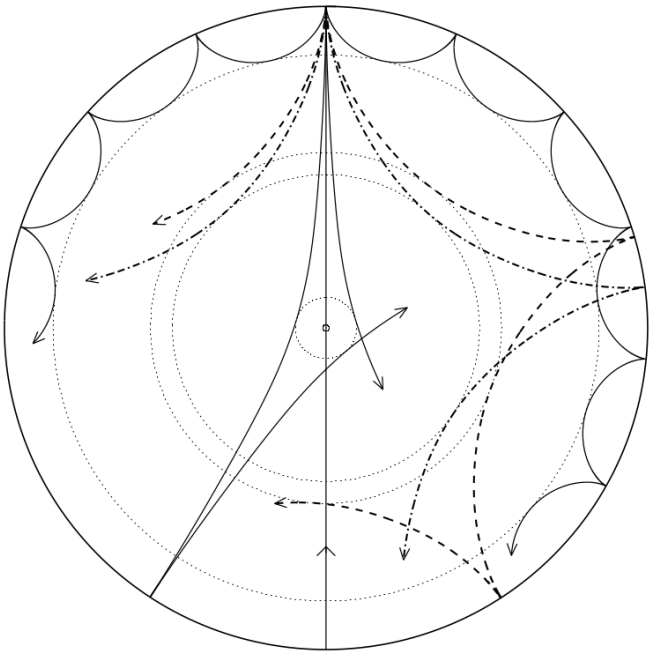

Figure **2-1**.: Ray path propagation in the solar interior for a given standard model. Image shows frequencies of 3000 μHz. The shallower refracted rays correspond to high-degree modes with $l = 75$, whereas deep penetrating rays have small degree values. Image taken from (Christensen-Dalsgaard, 2014).

There is a question that arises from the study of the Sun: "How is it possible to study the solar interior given that light can not escape from the interior to outside regions beyond the photosphere?". There are two phenomena which are known to travel across deep Sun layers and emerge with coherent information to its surface; neutrinos and solar oscillations. The latter is the subject of *helioseismology*. In helioseismology, there are two branches intended for global and local diagnostics. *Global helioseismology* analyses the Sun as a whole, taking data for a considerable length of time in order to improve in spectral resolution to characterize single peaks and oscillation modes in a power density spectrum (Figure **1-6**). Major findings of global helioseismology relate to the discovery of a thin layer where the Sun ceases to rotate like a rigid object (tachocline, see Spiegel and Zahn, 1992), the internal rotation as a function of depth and latitude (Schou et al., 1998), and the discovery of normal oscillation modes with period of 5 minutes (Leighton et al., 1962), about 3.3 mHz.

On the other hand, *local helioseismology* (first developed by Gough and Toomre, 1983) intends to construct the topology and dynamics of local regions below the photosphere, taking into account the evolution of magnetic field structures. This constructions are based on the

measurements of wave time travels on the solar surface. For this constructions to become reliable, high-resolution of high-degree modes are required; local helioseismology takes full advantage of the proximity of the Sun, as it is the only star which we can study in enough resolution to detect high degree modes in great detail. The main goal of helioseismology is to infer solar structure and dynamics via the study of linear and adiabatic oscillations. These provide the basis for the *theory of stellar pulsations*, which besides solar-like stars, also applies for several types of multi periodic pulsation stars, as δ Scuti, β Cepheids and pulsating white dwarfs.

To study global oscillations, global seismology analyzes long time series of Doppler or Intensity diagrams (Chapter 3). As these oscillation frequencies depend on the solar interior, it is possible to apply *inversion techniques* to infer proper models of structure. Inversion techniques include inversions for solar rotation, for solar structure, inversions for sound speed and so on. These have included several approximations (as the asymptotic theory known as Duvall's law, in Duvall, 1982), whose results are constantly improving given a better computational capacity. To learn more about these inversion techniques, as well as the state of art of global seismology, see the reviews of Gough and Thompson (1991), Basu (2016) and section XI. C of Christensen-Dalsgaard (2002).

It is agreed that solar oscillations are excited stochastically near the surface by turbulent convection causing random fluctuations (Goldreich et al., 1994). Thus, the power spectrum for a single line profile, given by an exponential decay, takes the form of a Lorentz profile (a full development on Fourier analysis of time strings can be found in section 2.2 of Christensen-Dalsgaard, 2014, *Fourier analysis of time strings*). To model wave excitation of solar oscillations, a source term $\vec{\mathcal{S}}$ is added to the perturbed Euler equation as a function of the displacement (Gizon and Birch, 2005). A derivation of Euler equation could be consulted in Lynden-Bell and Ostriker (1967), where the momentum equation turns into:

$$\mathcal{L}\vec{\xi} = \vec{\mathcal{S}}$$

for adiabatic oscillations. Here, the operator $\mathcal{L}$ is a linear operator acting on the displacement vector $\vec{\xi}$, where only small amplitude waves take place. This source term accounts for granulation. When an impulsive source acts on the solar surface, Green's functions can be solved to give impulse responses for a given wave field. Hence, for an impulse reaction on a 3 dimensional point $\vec{r}'$ in a time t', the impulse at some other point $\vec{r},\ t$, the Green's function is:

$$\mathcal{L}G(\vec{r}, t; \vec{r}', t') = \delta(\vec{r} - \vec{r}')\delta(t - t') \tag{2-1}$$

Approaches to solve directly the Green's functions vary from a representation in Fourier space to an expansion in normal modes. The formalism of Green's functions will be used in the *Acoustic holography*, an helioseismic technique which we will introduce further. In this chapter we focus on the description of local helioseismology, as well as some of its results.

2.1. Local Helioseismology

As global modes are influenced by general surface properties of the Sun, these oscillations are not affected by local structure, say magnetic fluxes or meridional flows. Braun et al. (1987) found that sunspots are regions of an important absorption of acoustic waves. They showed, by means of a Hankel transformation in cylindrical coordinates of the incoming/outgoing wave field, that sunspots either absorbed or scattered acoustic energy. This opened the prospect of how magnetic fields interact with the wave field in regions beneath the solar surface. This linkage, as well as with other photospheric dynamic phenomena, allows a 3 dimensional reconstruction of the local interior. This constitutes the basis of local helioseismology.

2.1.1. Techniques

For a local perspective, there are five well known techniques to provide information about shallow regions below the photosphere: the Fourier Hankel method, Ring diagram, Direct modeling, Time-distance, and Helioseismic holography. The *Fourier Hankel spectral method* (Braun et al., 1987) consists of a wave field decomposition into Hankel functions in cylindrical coordinates. The goal is study both the absorption (and scattering) of waves entering a magnetically active region, and the phase shifts between incoming and outgoing waves. Several results of the Hankel method and its mathematical description can be found in Braun et al. (1987), Braun et al. (1992) and Braun (1995).

The *Ring diagram analysis* (Gough and Toomre, 1983) is based on frequency changes due to the presence of a local velocity field (and variations of the sound speed) in a small portion of the Sun. Changes are computed via Doppler shifts from power density spectra of Postel projected maps (Section 3.2.2). The diagrams are plotted as a function of horizontal wavevectors (k_x, k_y) for a given frequency ω. This results in ring shaped like structures, whose shifts and distortions are a direct consequence of variations in the horizontal velocity field and in sound speed. The description of the technique can be found at Hill (1988). For the *Direct modeling* shallower flows are estimated from inversions of the correlation functions of the wave field in the Fourier formalism. Ideas behind this technique follow the full procedure developed by Woodard (2002).

The *Time-Distance helioseismology* procedure (Duvall et al., 1993) takes precedent on the time travel of waves between any two points on the photosphere. This time travel represents an integral of the sound speed along the path of minimum energy of the wave (equation (A-2)), path which is given by a suitable theory of wave propagation, such as Snell's law. Measurements of the time travel for a great number of rays allow further inversions to yield both the sound speed and velocity flow inside the Sun up to a depth given by the *turning point*. Temporal cross-covariance functions between two locations on the solar surface, as

well as proper time travel measurements for inversion methods can be found in the review of Kosovichev et al. (2000).

2.1.2. Helioseismic Holography

Helioseismic holography is a method to study acoustic sources inside the Sun via holography. Although the idea of holography was suggested in 1975 by Roddier (1975), Lindsey and Braun (1990) introduced the idea of holographic observations to visualize the acoustic field in sunspot regions. The central idea is to use the velocity field observed on the solar surface (e.g. via Line-Of-Sight, Doppler maps, Chapter 3) to make an estimate of the acoustic field as a function of time for a given depth.

The principles of the computational helioseismic holography are the application of electromagnetical wave optics to solar oscillations; as perturbations in the solar interior produces acoustic sources traveling both upwards and downwards, the acoustic signal mapped onto the surface can be used to infer the location and size of this source. Image **2-2** shows the wavefronts of two submerged acoustic sources at different depths, with a 3 dimensional propagation from the source point.

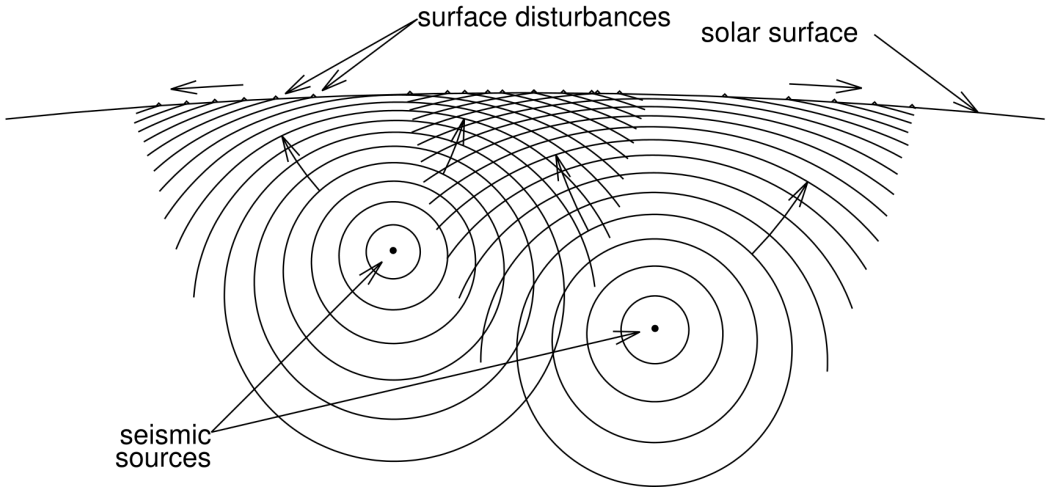

Figure **2-2**.: 2-D representation of the wavefront diagram of two acoustic sources beneath the solar surface. These seismic sources appear in the surface as ripples propagating outward from the projected point of the source at the photosphere. Image taken from Lindsey and Braun (2000).

The calculation of the sources reduces to the calculation of the Green's function at the desired depth, rendering images for the *acoustic egression* (or egression maps) for a given frequency range:

$$H_+^{\mathcal{P}} = \int_{\mathcal{P}} \Psi(\vec{x}', \omega) G_+(\vec{x} - \vec{x}', \omega, z)\ d^2x' \tag{2-2}$$

Where $\mathcal{P}$ represents the *pupil*, the annular region where the integration takes place. The depth z at which the computation takes place represents the electromagnetic analogy of the focal plane. Figure **2-3** shows an application of the holographic method to sunspot in NOAA 7973. In the figure, egression maps provide images of acoustic deficits (as pointed by Braun et al. (1987)).

Wide applications of helioseismic holography have been developed to imaging solar structures. Major insights include solar phenomena related to acoustic transients. Full reviews of its applications can be found at Lindsey and Braun (1990), Lindsey and Braun (1998), Donea et al. (1999), Lindsey and Braun (2000) and Donea and Lindsey (2005). In appendix A there is a brief description of the computational task developed in acoustic holography. Many results from this technique will be applied through this document.

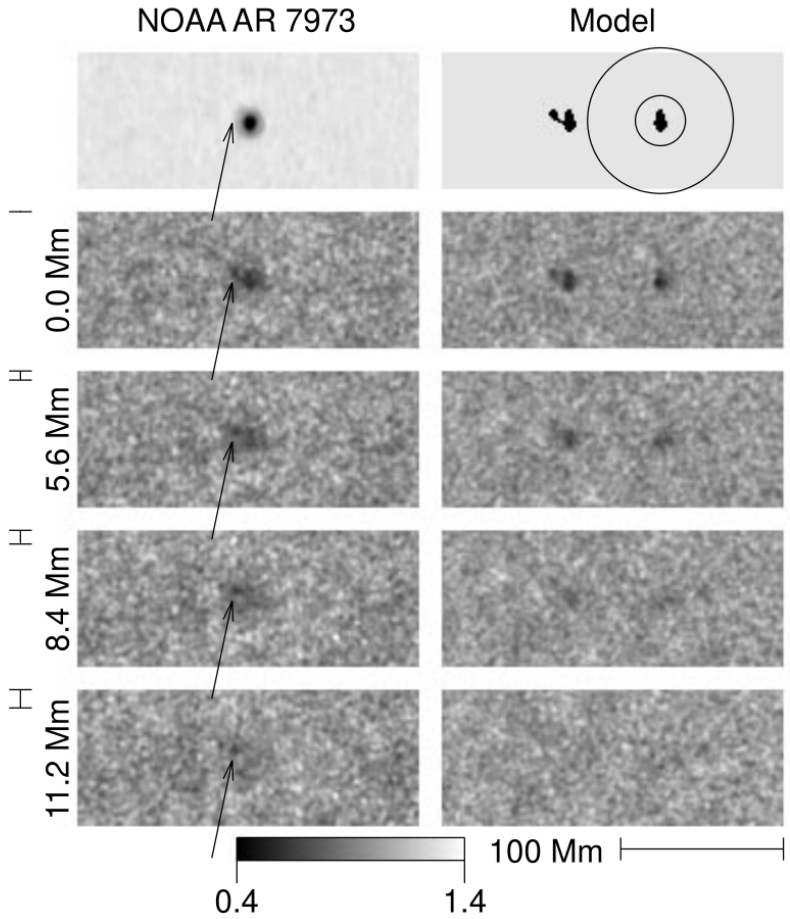

Figure **2-3**.: *Left column:* egression power maps for the NOAA AR 7973 (*top left*) at (6 ± 0.5) mHz for an integrated temporal range of 24 h at different depths. *Right column:* egression power maps for an acoustic noise given by the Solar standard model (*top right*, inside the pupil) to replicate the real signature. The different depths represent the focal plane at which acoustic holography is calculated. Image taken from Lindsey and Braun (2000).

2.1.3. Seismicity associated to solar flares

One of the applications of helioseismic holography is to study solar phenomena apparently caused by solar flares. One of these phenomena are *sunquakes*, which are observed as ripples on the solar surface (Figure **2-4**). Being first predicted by Wolff (1972), the first observation of a sunquake was made 26 years later by Kosovichev and Zharkova (1998) with improvements made to solar observatories. These are acoustic waves which are believed to be excited by *some* mechanism near the photosphere in the outer atmosphere. Furthermore, since these are waves driven by changes in pressure, sunquakes travel into the Sun refracting back to the surface due to the in-depth increase of sound speed. As the waves approach the photosphere, abrupt changes in pressure and density at the boundary interior-atmosphere make part of the energy of the waves to escape and part to be reflected back into the solar interior. Along acoustic holography, time-distance has encouraged the detection and study of sunquakes (e.g. Kosovichev and Zharkova (1998), Zharkov et al. (2013), Martínez-Oliveros et al. (2008) and Zharkov et al. (2011) and reference therein).

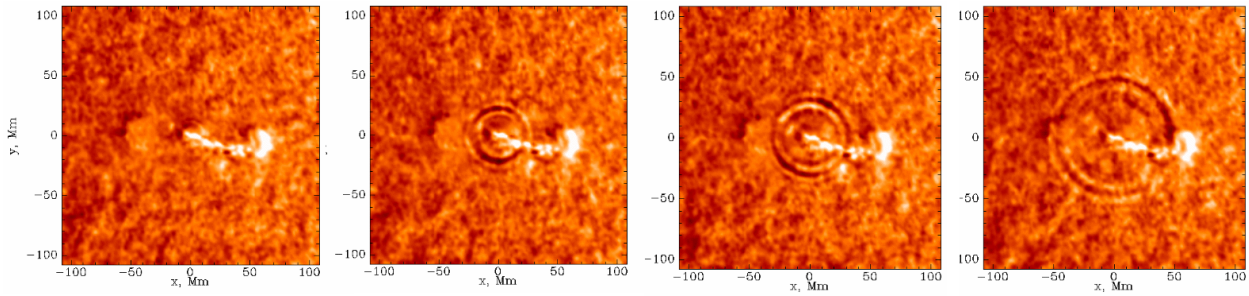

Figure **2-4**.: Temporal image sequence of the first sunquake detected (Kosovichev and Zharkova, 1998). By the rules of linear optics, waves driven by pressure perturbations travel from the surface into the solar interior, then refracting back into the solar photosphere, signature recognized as the sunquake wavefront. The images have a temporal cadence of 1 minute.

Several hypotheses for sunquake generation have been postulated. The most common ideas state that its nature is either by particles or by magnetic field interaction. In the particles scenarios, authors estimate three possible mechanisms based on high energetic electrons and X-rays reaching the photosphere. In the backwarming radiation hypothesis (Machado et al., 1989), heating of the surrounding material increases the pressure producing waves to the solar interior. This is usually followed by emission in white light. Observations of gamma ray radiation correlated to seismic signatures reveal the feasibility of direct particle collision to take place (Donea and Lindsey, 2005). Moreover, given the energy released by solar flares, sunquakes could be excited by shock waves, waves produced as a heating and subsequent cooling emitting Hα radiation and X-rays (Sturrock, 1966).

On the other hand, magnetic field changes have been studied as seismic drives (Hudson et al., 2008). After the energy is released of a solar flare, magnetic field lines relax becoming

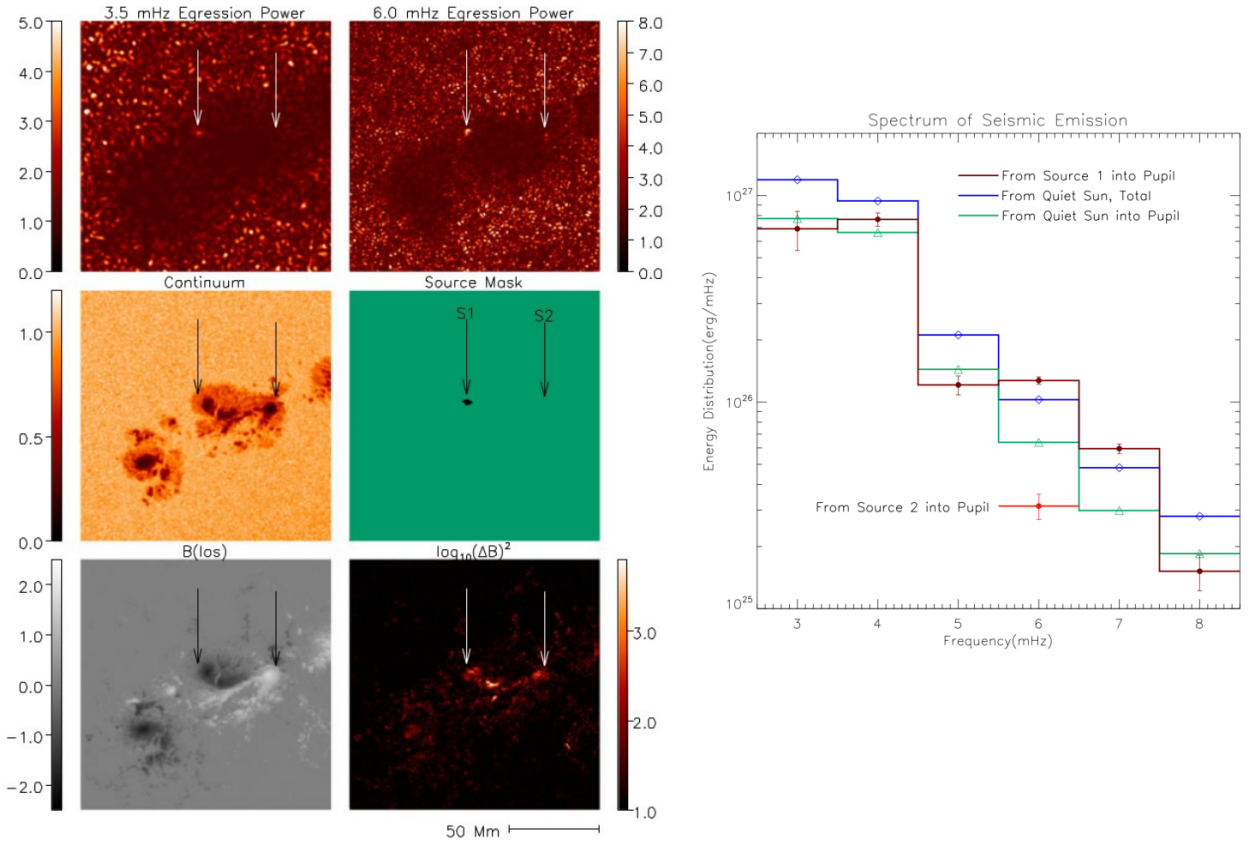

Figure **2-5**.: *Left:* top panel presents two snapshots of egression maps at 3.5− and 6.0 − mHz for the event SOL2011-02-15T01:56 X2.2. Both bandwidths show regions of transients which are labeled as source 1 and source 2 (S1 and S2). *Right:* energy seismic emission spectrum for the two sources. It is evident that the larger the frequency is for which a decrease in seismic emission can be seen, the stronger the source. Overall, the seismic signature has greater energy than the surrounding background. Images taken from Alvarado-Gómez et al. (2012).

more horizontal. This topology causes the Lorentz force to exert a work on the surface which in principle could suffice to generate enough acoustic energy to induce a sunquake. For this mechanism to work, a permanent change in the magnetic field (i.e. permanent increase or decrease of the magnitude of the magnetic flux) is needed. Sudol and Harvey (2005) studied these permanent changes for a large survey of X class solar flares. Important works on the exploration of magnetic field changes as a possible mechanism related to the seismic transients include Martínez-Oliveros and Donea (2009), Russell et al. (2016) and Fletcher et al. (2011). In addition, Castellanos Durán et al. (2018) found several permanent magnetic field changes for a list of 75 solar flares spanning from X to C class. The unusual high appearance of seismic events related more to M-class than X-class solar flares, can be explained as a statistical view of point; Buitrago-Casas et al. (2015) explained the occurrence given that there is a much greater database for these type of M-class solar flares.

An important result of acoustic holography applied to seismically active solar flares is presented in Alvarado-Gómez et al. (2012), which is reflected in Figure **2-5**. As Alvarado-Gómez et al. pointed out, the seismic energy is mainly emitted in the $2.5 - 4.5$ mHz range. For the time-distance technique, it is usual to work within the (6 ± 1) mHz bandwidth, given that the ratio of acoustic emission respect to that of the quiet Sun is large. This feature is effortlessly seen in the histogram at the right side of Figure **2-5**. In the (7 ± 1) mHz bandpass the seismic signature inside Source (S1) is also significant. Nevertheless, Zharkov et al. (2011), again with acoustic holography, found a seismic component extending beyond the (6 ± 1) mHz component (Figure **2-6**).

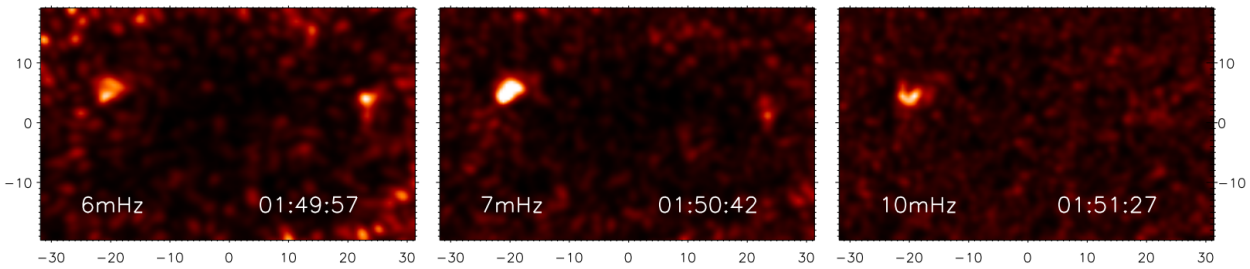

Figure **2-6**.: Multi-frequency snapshots for the SOL2011-02-15T01:56 X2.2 near the GOES flare peak. Image from Zharkov et al. (2011).

This *rare* signature opens new prospects in the study of acoustic transients. It describes faster processes happening in the solar environment related to the emergence of acoustic transients. The detection is achievable thanks to the improvement of instrumentation as the temporal cadence of any instrument limits its spectral study. In signal processing this limitation is known as the *Nyquist* frequency, and represents the maximum allowed frequency in an analog signal without aliasing. The Nyquist frequency, Ω_N, is:

$$\Omega_N \leq \frac{1}{2}\nu = \frac{1}{2T} \tag{2-3}$$

where T represents the temporal cadence of the discrete observation, and ν the sampling rate of the time series. It says, particularly, that a sampling rate ν of at least twice the highest frequency will properly retrieve the time sequence. The HMI instrument (Chapter 3), whose temporal resolution is 45 s, lets a spectral scanning up to $\Omega_N = 1/(2\ 45\ \text{s}) \approx 11.1$ mHz. This work is intended to perform a study on the emission of transients (acoustic transients) from solar flares. We analyze whether there could be a trigger for solar seismic events not necessarily related to solar flares and the mechanisms previously described.

3. Instruments and Data Description

3.1. Solar Dynamics Observatory

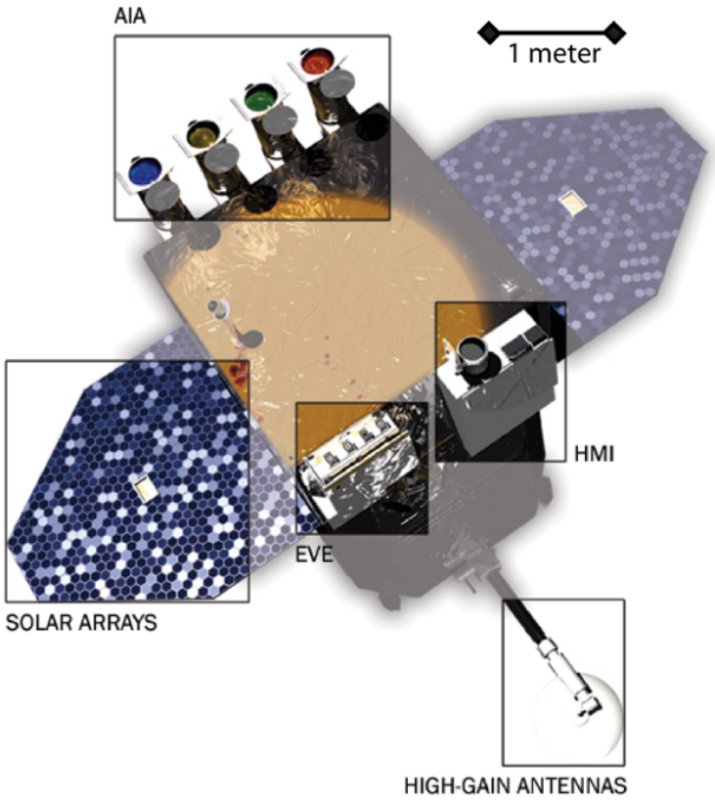

Figure **3-1**.: The Solar Dynamics Observatory spacecraft. The image shows its three main instruments, an overlaid image of the solar atmosphere with various features, a high gain antenna and solar arrays. Image taken from (Pesnell et al., 2012)

For the purpose of this work, we selected data taken by the Solar Dynamics Observatory (SDO) (Pesnell et al., 2012). This is a space observatory launched on February 11, 2010 giving its first light by March 30 of the same year. Its main goal is to study the solar variations that could affect life on Earth, developing a predictive capability of this phenomena. Since then, SDO has been monitoring the Sun covering almost all the Solar Cycle 24. In addition, the spacecraft is also used to study the generation of the magnetic field of the Sun along the main causes of space weather. Among its orbital parameters, SDO has a geosynchronous orbit with 28° of inclination located above the ground service station in New Mexico at 105° longitude west. This allows continuous data transfer between the Satellite and the ground station.

To study different features of the Sun, SDO is shipped with three instruments. The Atmospheric Imaging Assembly (AIA), the Helioseismic and Magnetic Imager (HMI) and the Extreme-Ultraviolet Variability Experiment). From this variety of SDO data, we analyze data taken by the AIA and HMI instruments.

The main motivation of **HMI** (Schou et al., 2012) lies in the study of the solar interior via helioseismology, in addition to the understanding of magnetic field processes on the solar surface. This is achieved by measuring Doppler shift and magnetic flux density (both in the Line−Of−Sight, LOS) and continuum intensity using the Fe I 6173.34 Å absorption line, with six 7.6 mÅ wide narrow band filters spanning a spectral range of ±172.5 mÅ along the central wavelength (Figure **3-2**). Additional measurements for the vector magnetic field are also available. The optics package of the instrument, among others, consists of a front window, a 14-cm refracting telescope, a five-stage Lyot filter and a Michelson interferometer, coupled with a pair of 4096×4096 pixel CCD cameras. The CCD captures a full disk image of the Sun resulting in a spatial resolution of 0.504" (seconds−of−arc, arcsec), with a temporal cadence of 45 s for the LOS and continuum intensity observables.

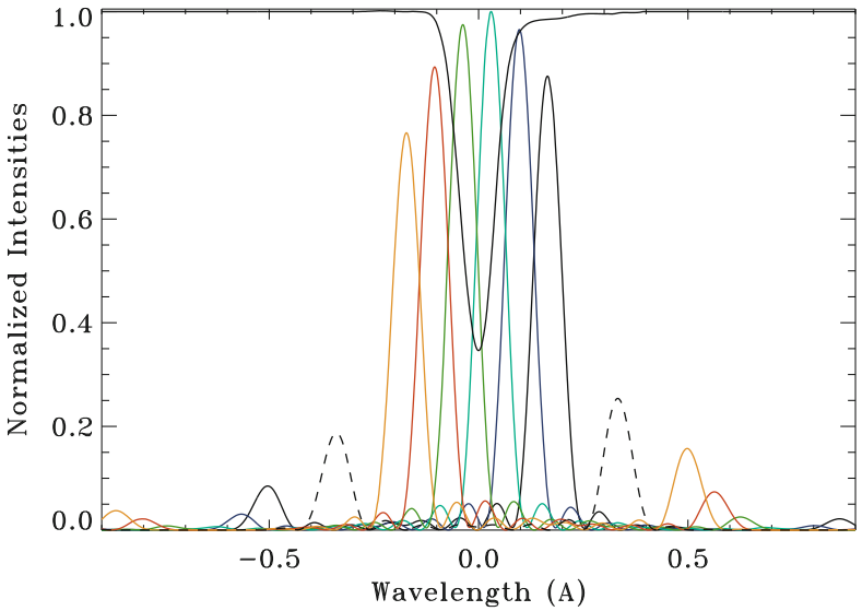

Figure **3-2**.: Transmission profiles for six different filters. The optics package comprises six narrow band filters with a FWHM of 76 mÅ±10 mÅ, spanning ±172.5 mÅ around the central wavelength. Each filter measures left and right circular polarization states in order to retrieve LOS observables through the fitting of the Fe I line, which is represented as the solid black line. Taken from Couvidat et al. (2012b).

The observables are calculated from the images through the MDI-like algorithm (Couvidat et al., 2012a). The algorithm assumes a gaussian-like shape for the Fe I line, calculating its first and second Fourier coefficients so as to retrieve the profile. In order to estimate the

precision of this algorithm, it was tested with an Interferometric Bidimensional Spectrometer (IBIS) observation, which is an instrument with a similar cadence as the one of HMI, but with a three times better spectral and spatial resolution (25 mÅ and 0.165" respectively). The implementation of the algorithm gives rise to velocity maps called *Dopplergrams* which are presented in units of m s^{-1} with a precision of 13 m s^{-1} and a dynamical range of $\pm$6.5km s^{-1}. On the other hand, magnetic field maps, or *Magnetograms*, represent the magnetic flux density measured in Gauss [G] units, with an accuracy of 10 G and a dynamical range of $\pm$4 kG, while the continuum intensity maps account for the number of counts per second on the camera (DN/s) with an accuracy of 0.3% (Figure **3-3**). The vector magnetogram products are data with 720 s (12 m) of cadence and come in "patches", which are observations on a specific active region. These are known as SHARP data (Spaceweather HMI Active Region Patch). The images are computed on ground at the Joint Science Operations Center (JSOC) at Stanford University.

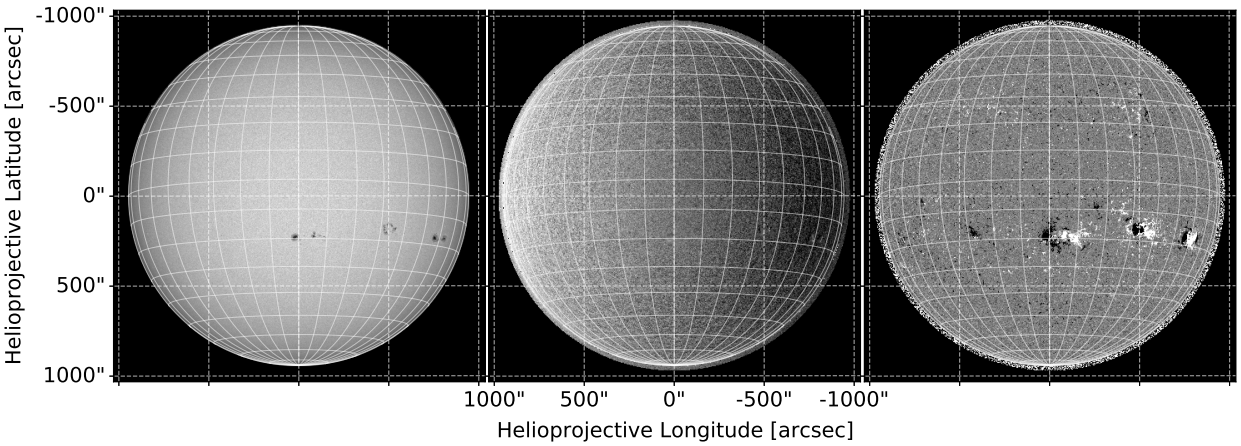

Figure **3-3**.: Continuum intensity, velocity and magnetic field maps from HMI of July 30, 2011 at 02:09 UT. The HMI represents an improvement of the prior Michelson Doppler Imager (MDI) on-board the Solar and Heliospheric Observatory (SOHO) spacecraft, which uses the Ni I line 6768 Å for calculations. The maps show negative values upwards due to the roll angle between the optical array and the heliographic north ($\sim 180°$).

The **AIA** instrument (Lemen et al., 2012) observes the Sun in seven wavelengths of the extreme ultraviolet (EUV) and three of the ultraviolet (UV). The EUV channels allow the reconstruction of the solar corona with images from 1 MK up to 20 MK, and altogether represent full-disk images from the transition region to the corona up to 0.5 $R_{\odot}$. One of the scientific goals of the instrument is to understand the mechanisms of solar variability and storage/release of energy into the interplanetary medium and the heliosphere. The data products are images with spatial resolution of 0.6" per pixel obtained every 12 s. AIA consists of four telescopes, one of which captures two images near the continuum, at 1600 Å and 1700 Å. It has even a continuum image at 4500 Å, but due to an artifact in

visible light (with an arc shape on one of the sides of the image), it is currently in disuse and has a replacement with HMI's continuum image.

All data products are stored in the Flexible Image Transporting System (FITS Pence et al., 2010) which represent a data structure containing a header. The header contains a series of `keywords` with its respective `values` in order to store information of the astronomical object. Keywords include, among others, details such as the datatype (16-bit for continuum and LOS Doppler maps, 32-bit for LOS Magnetic field maps), number of axis, size of the image in pixels, size of the pixel in physical units, date of observation, Wold Coordinate System (WCS), calibration history, comments and so on.

3.2. Data description

The WCS assigns coordinates for each pixel in the FITS file. This assignation is made by setting the value of the coordinate pair (for example latitude/longitude) to a pixel. LOS observables and continuum data from HMI are set in the "Helioprojective Cartesian" coordinate system, which takes the center of the 2 dimensional image as the reference point for the solar latitude and longitude. Both helioprojective latitude and longitude are set in angles given in arcsec ranging from 0" to the solar radius ($\sim$ 938" for the perihelion to $\sim$ 969" at the aphelion).

3.2.1. Coordinate representation

For solar data, three coordinate systems can be identified, the *Heliocentric*, *Helioprojective* and *Heliographic* coordinate systems (Thompson, 2006). The Heliocentric Coordinate System, whose origin is the center of the disk, measures the distances in physical units from this center. Here, the solar coordinates could be represented by a cartesian (x, y, z) or radial (ρ, Ψ) coordinate system. The Helioprojective Coordinate System, the one which HMI uses for data science, makes a projection the heliographic system, replacing the physical grid coordinates by angles. These coordinates transformations allow to have longitude and latitude to describe the data. Finally the Heliographic Coordinate System takes into account the solar equator as the reference for the latitude Θ; unlike the other coordinates, does not set the center as the center of the disk. For the longitude, there are two perspectives: the *Stonyhurst*, which marks the origin of longitude as the intersection of the solar equator and the central meridian as seen from Earth, and the *Carrington* one, which considers the mean rotation of the Sun (27.2753 synodic days, 25.38 sidereal days) starting from November 9, 1853 (Stix, 2004). Each intersection of the Carrington and Stonyhurst prime meridian, marks the beginning of a new *Carrington rotation*, measured in Carrington numbers. For example, the Carrington number for January 1, 2020 was 2226. The grid of figure **3-3** rep-

resents the heliocentric/helioprojective (cartesian grid) and the heliographic (lines of solar latitude/longitude) coordinate systems.

3.2.2. Maps Projection

In order to track regions over time, images are remapped onto an azimuthal perspective, the *zenithal equidistant* projection also known as the *Postel* projection. This projection is useful from a geometrical point of view because, when mapped over a region, it deprojectes the image as if the instrument of observation were directly on top of the region.

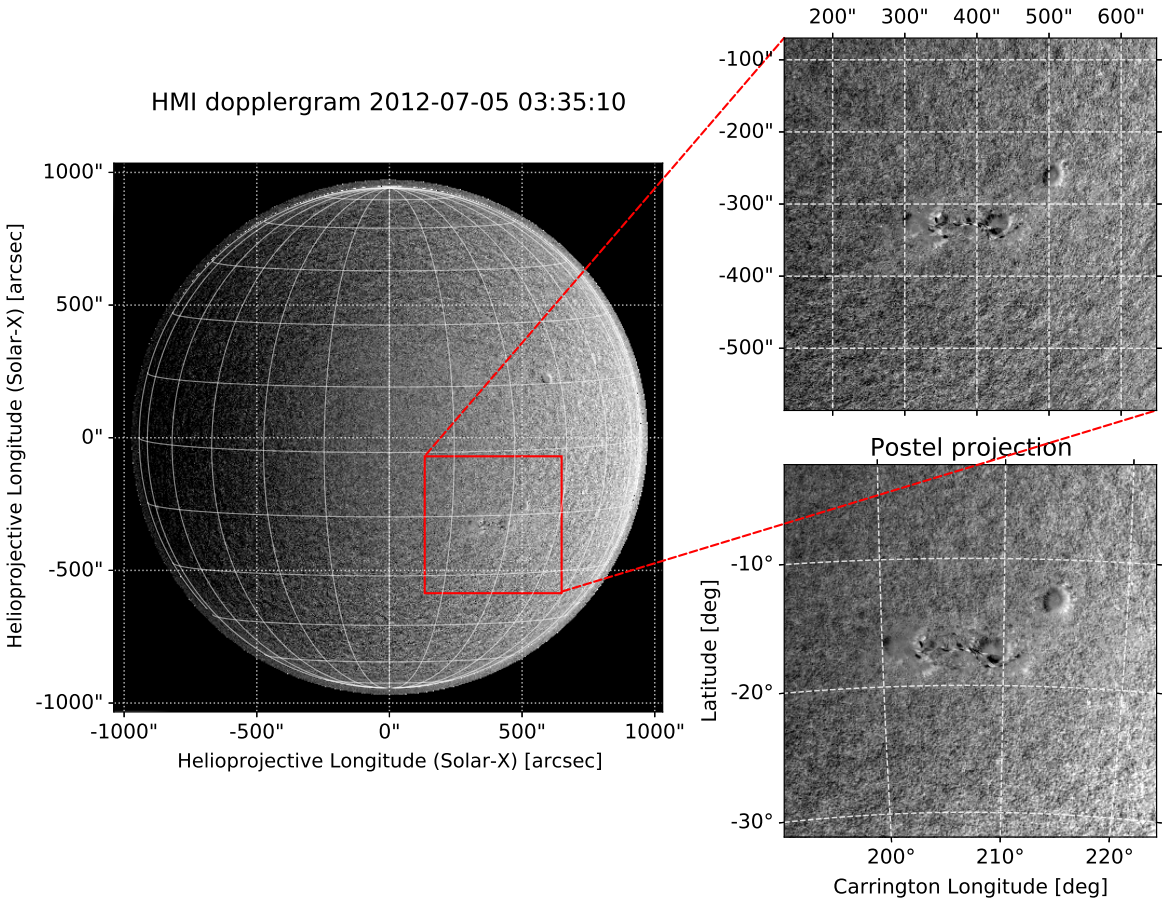

Figure **3-4.**: *Left:* HMI dopplergram of July 5th, 2012 at 03:35 UT. A red square is drawn to indicate the Field-of-View specifying an active region. The top right image represents the cut in the FoV with inherited helioprojective cartesian coordinate system from the full disk image. The Postel-projected map of the FoV at bottom right highlights the change in area and angles in comparison to the top image. The left image has been rotated $\sim 180°$.

To construct a Postel-projected map, we select a Field – of – View (FoV), which consists of

a rectangular region centered on the feature to study, for example an active region on the Sun where a solar flare took place. On the FoV, a reference point is selected in order to determinate the tangent plane whereby the points of the sphere are to be mapped into it. These points are mapped in such a way that they preserve radial distance from the reference point, i.e., azimuthal distances are properly scaled when measured from the center of the projection.

This projection does not keep equal areas over the map (not equivalent) nor is conform (does not keep the angles). However, for nearby points, the projection is reliable in areas and angles. Figure **3-4** shows a helioprojective and Postel projections for the same FoV region. The image on the left is represented in the original helioprojective cartesian coordinate system, in which a heliographic grid is overplotted on the solar disk.

3.2.3. Data processing

According to the stage of data processing of HMI images, different "levels" are defined: the *level 0* represent raw images taken directly from the CCD, which are subsequently corrected for bad pixels and flatfielding giving rise to *level 1* images, also known as filtergrams. *Level 1.5* are the three downloadable observables, obtained by applying the MDI-like algorithm to level 1 images. Finally, the *level 2* are images with additional user processing, performed for a specific analysis.

In this work, further corrections to produce level 2 images include:

(a) rotation counterclockwise for the observables due to the roll angle of both the SDO spacecraft and the telescope respect to the heliographic north,

(b) limb darkening correction for intensity images,

(c) measure of the solar rotation and mean velocity signature to be subtracted from the Doppler maps,

(d) coordinate transformation from helioprojective cartesian to the heliographic in the perspective of Carrington longitude, and

(e) Postel projection around some point specified in the selected FoV.

Item (d) allows a straightforward tracking of the region in the FoV across time; when calculating the Postel projection it is only required to keep the Carrington Longitude constant in time for each frame.

3.3. Flare selection criteria

In order to study depth and frequency dependence of acoustic maps of solar flares and photospheric magnetic fields associated to the acoustic source, we selected five solar events from the past 24$^{\text{th}}$ solar cycle. The flare peak fluxes of the events in the GOES 1.0 − 8.0 Å range covered from M1.5 to X2.2 class. The locations of the events were selected in such a way that the solar flare positions were $\mu > 0.6$, where $\mu = \cos\theta$ with θ the heliocentric viewing angle. The selection spans a period of time from 2011-02-15[1] to 2012-07-05, which corresponds to the first part of the 24$^{\text{th}}$ solar cycle. The selection of events was made from the list of solar flares of Buitrago-Casas et al. (2015) and Castellanos Durán et al. (2018), which covers a wide range of power outputs and locations on the solar disk (Table **3-1**).

Table **3-1**.: Solar flare selection. The class is given by the GOES X-ray flux in the 1.0 − 8.0 Å range. The NOAA number represents a numerical classification given to Active Regions since January 5, 1972. The helioprojected coordinates are given in arcsec from the solar center from which μ is estimated. These events witnessed both white light enhancement and permanent LOS magnetic field changes in the neighborhood of the active regions. Each solar flare hosted at least one sunquake event as detected by time-distance diagrams.

Class	NOAA	Date	Time/UT			Position		μ
			Start	End	Peak	X	Y	
X2.2	11158	2011-02-15	01:44	02:06	01:55	171	-293	0.84
M9.3	11261	2011-07-30	02:04	02:12	02:09	-525	170	0.61
M6.1	11429	2012-07-05	11:39	11:49	11:44	483	-347	0.74
M4.7	11515	2012-07-05	03:25	03:39	03:36	439	-343	0.60
M1.3	11515	2012-07-04	14:35	14:42	14:40	278	-341	0.74

The acquisition of the observables is made trough a Python script with the `sunpy/drms` module (*Data Record Management System*, Glogowski et al. (2019), version 0.6.2 as of November 2021). `drms` accesses data from the JSOC (Joint Science Operation Center) server at Stanford University through a JSON interface supplied by JSOC. This module provides an easy to use interface to download SDO data; to download full disk images from HMI it is only required the time interval and the physical observable.

Since the spectral study of solar flares involves maps in discrete time series, this wide range of time allows a good spectral resolution. One has to bear in mind that this Fourier transformation in the time dimension is the direct result of applying the Fast Fourier Transform technique (FFT), which is faster if the number of time steps -the number of frames- is a power of 2. Aiming to retrieve holographic calculations, for each solar flare we downloaded 256 full disk images with 45 s cadence around the GOES peak flux. This results in 01 h 36

[1]The first X-class solar flare of the past solar cycle registered by the HMI camera.

min of data files before and after the peak.

4. Analysis: Subphotospheric ultra-impulsive acoustic sources

In this chapter, we present observational analysis of the seismically active flaring regions at high frequencies calculated at different depths measured from the solar surface. This is performed with computational helioseismic holography (section 2.1.2) whose Doppler signatures correspond to the *Line – Of – Sight* (LOS) Doppler filtergrams from SDO/HMI at Fe I 6173 Å absorption line with a cadence of 45 s (section 3.1). We discuss the morphology and dynamics of the acoustic transients, as well as its location and relationship with the continuum intensity, LOS velocity, and LOS magnetic field maps for each source region.

4.1. SOL2011-07-30T02:09 M9.3

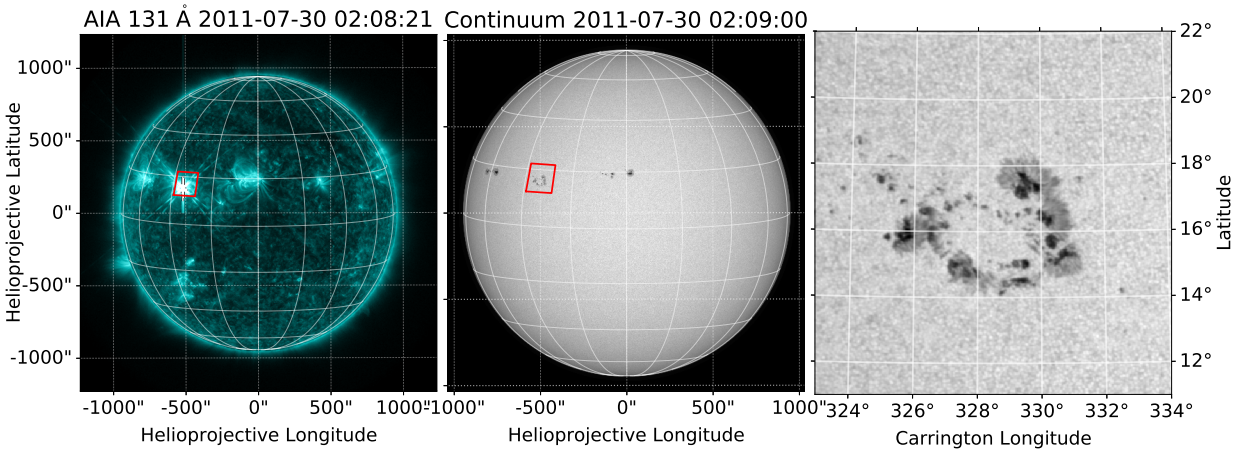

Figure **4-1**.: SOL2011-07-30T02:09 M9.3 solar flare as seen from SDO. The left panel shows an EUV channel from AIA in 131 Å approximately one minute before the flare peak. The middle panel corresponds to the HMI full disk continuum intensity at 6173 Å at the flare peak, whose postel projected image, which is enclosed by the red polygon, shows a close-up view of NOAA AR 11621 in the right panel where holographic calculations were performed.

On 30 July, 2011, NOAA AR 11621 hosted a X-Ray M9.3 class solar flare observed by HMI

at helioprojective coordinates X = −525″ and Y = 170″ (Figure 4-1). The beginning of the impulsive phase took place at 02:04 UT, ending at 02:12 UT, and with the peak at 02:09 UT in the spectral band (1 − 8) Å. This flaring region witnessed a remarkable sunquake whose impact which, according to Sharykin and Kosovichev (2015), does not correlate with the strongest HXR emission source (∼ 300 keV), and could not be produced by a flux rope model due to the absence of a Coronal Mass Ejection. We examined the coherent acoustic transient emitted by the flare radiated into the solar interior via acoustic holography (Martínez et al., 2020).

4.1.1. Ultra-impulsive Analysis

In order to reconstruct egression power maps, we applied computational helioseismic holography (Section 2.1.2) on the Doppler images up to 1 h after the GOES peak of the flaring region. The specific form of the acoustic-power holograph is the subjacent-vantage holography, were we consider radiation that propagates inward and then refracts back to the surface into the overlying pupil. The annular pupil used in the calculations extends from an inner

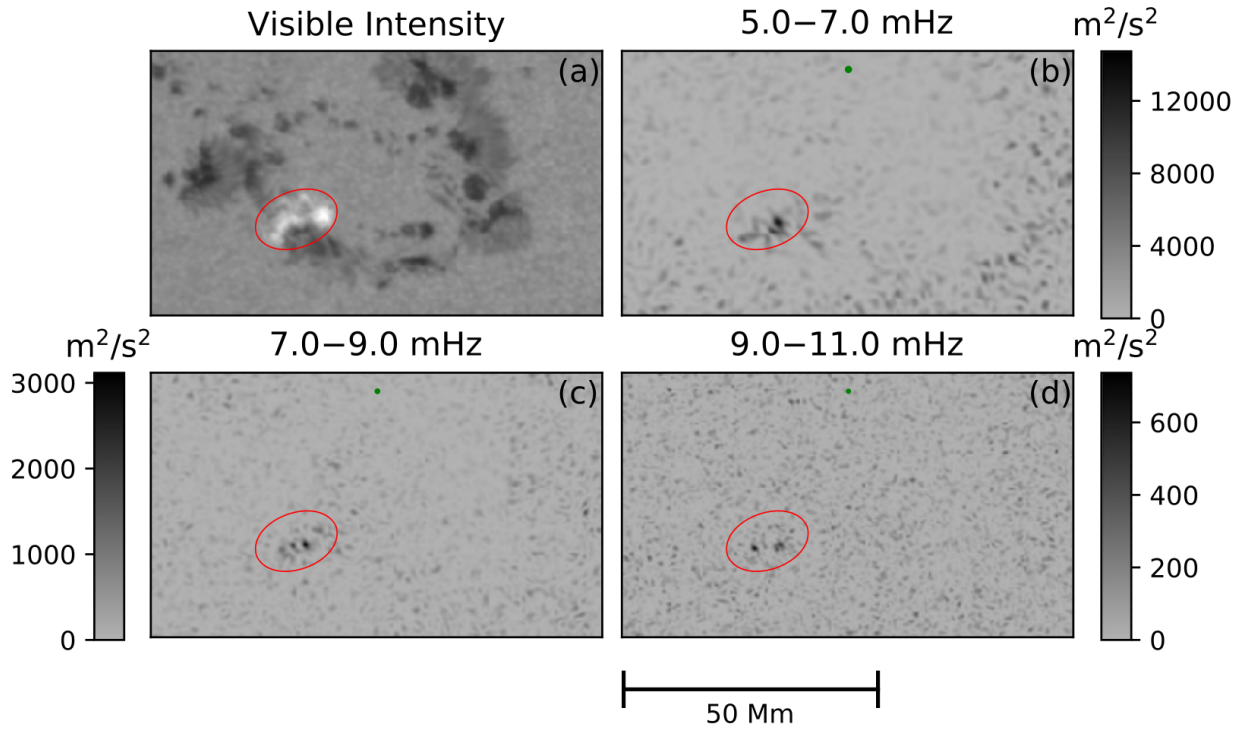

Figure **4-2**.: Source density maps from helioseismic holographic calculations of the transient released by SOL2011-07-30T02:04-M9.3 at 02:04 UT. The panel (a) is a zoomed view of the middle panel of Figure 4-1 with white-light emission enhanced by a factor of 5.0 on the red region. Panels (b), (c), and (d) show source density maps of the acoustic transient released in bands of 2 mHz width centered at 6, 8, and 10 mHz.

radius of value 7 Mm to an outer radius of 84 Mm. The source density maps are displayed on Figure 4-2. As seen from panel (a), the flaring region is a white-light flare, spatially related with the location of transients on source density maps at bandpasses of 2 mHz width centered at 6, 8, and 10 mHz (signatures encompassed by the red ellipses).

The green dots above panels (b), (c), and (d) represent diffraction limited responses to point sources located at the base of the photosphere; the greater the frequency is the sharper are the acoustic transients, and so the spatial resolution improves.

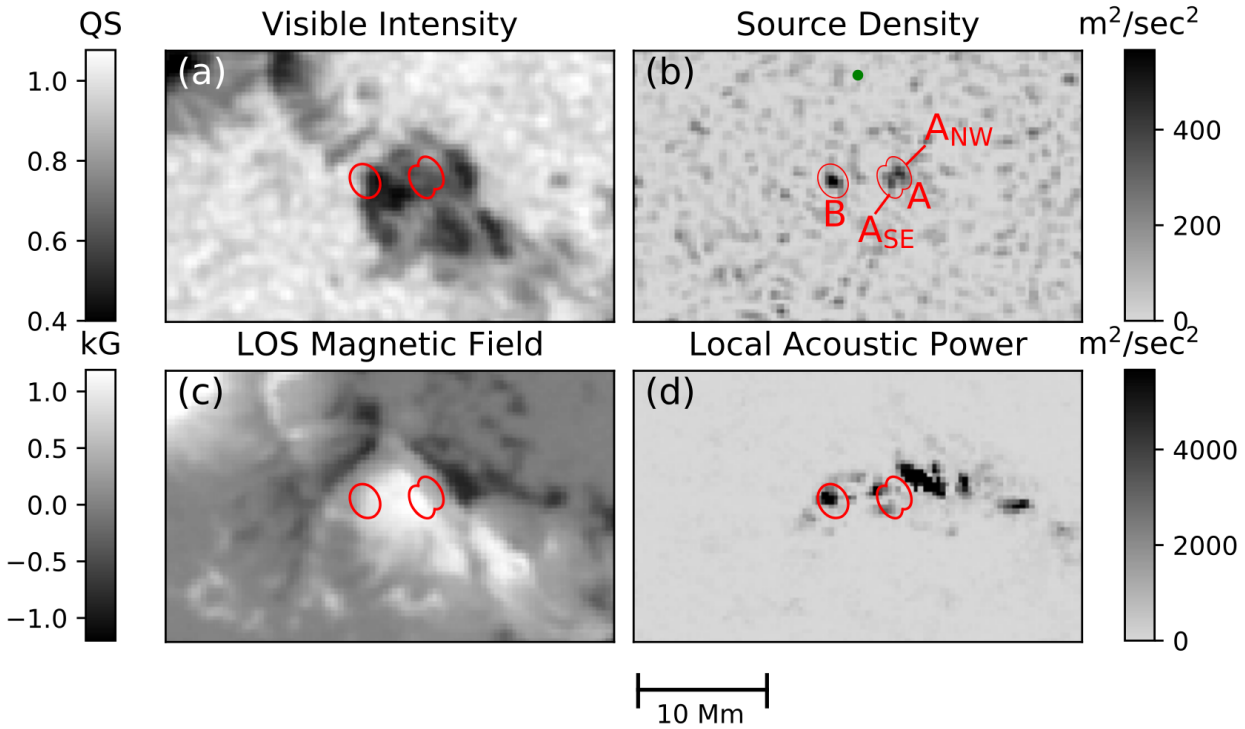

Figure **4-3**.: Comparison of the 10 mHz spectral bandwidth of Figure 4-1(d) with visible intensity normalized to the Quiet Sun (a), LOS magnetic field (c), and local acoustic power of the timeseries of the same band (d). One can distinguish two sources, source B, sitting on the northeastern boundary of the north-polar umbra, and source A, which kernels A_{SE}, and A_{NW} straddle a sharp penumbral magnetic boundary separating the northern and southern magnetic umbrae. Magnetic induction increases from $\sim$ 900 G in kernel A_{SE} to $\sim$ 1200 G in kernel A_{NW}.

Figure 4-3 is a close-up view of the transient region in intensity (upper left), LOS magnetic field (bottom left), and local acoustic power (bottom right) whose contours indicate the components of 4-2(d) centered at 10 mHz. In panel (b) we can identify two notorious components, which we call source A, located approximately 8 Mm west source B. From panels (a) and (c), the source B lies on the eastern (left) boundary of the umbra of northern magnetic polarity. On the other side, source B lies in the penumbra on the other side of the same umbra. Source A is seen to be composed of two kernels, denoted by A_{SE}, and A_{NW}, whose centroids are separated by $\sim$ 2 Mm. Source A straddles the boundary of the

penumbral region, separating the inner S-E region of up to 1200 G, from a surrounding N-W region of $\sim$ 750 G LOS. We cannot regard LOS Doppler or magnetic field signatures to be reliable in quantitative detail in the impulsive phase given the complications on atmospheric observations of active regions (Martínez Oliveros et al., 2014). However, these signatures serve as indicators of transients from the preflare Doppler or magnetic disposition of the locality, even when analyzing in the impulsive phase. From panel (d), the domain region of source B seems to coincide closely with a local Doppler disturbance suggesting that this is related to the acoustic transient released from that general locality. Conversely, source A is devoid of a significant acoustic-power anomaly.

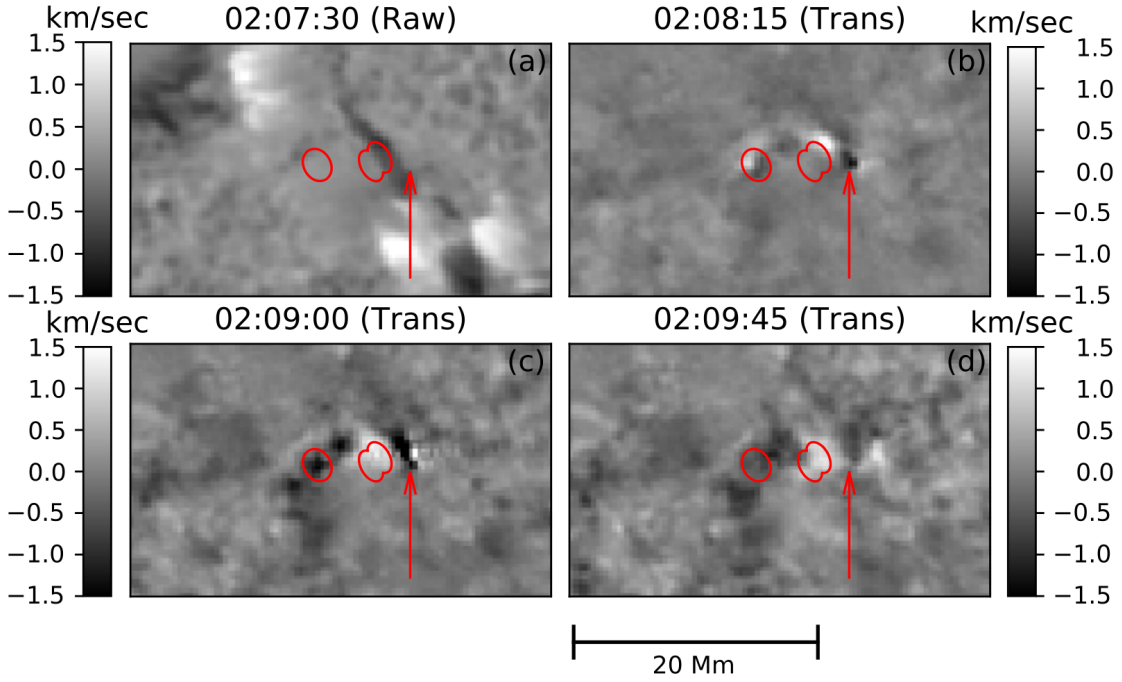

Figure **4-4**.: Preflare raw and transient signatures from the region defined in Figure **4-2**(d). The transient represents the consecutive difference between the raw and the raw-preflare Doppler maps. The contours are the same as Figure **4-3**, with arrows marking the locations of a strong transient on frames (b) and (c). The greatest transients, located next to source A, do not coincide to the sites marked by the ellipses.

Figure **4-4** shows a temporal evolution of preflare raw and transient signatures on LOS Doppler maps in the early impulsive phase. Panel (a) shows the raw-preflare signature. Panels (b)-(d) show the transient component, (difference between the respective raw and the raw-preflare Doppler maps, at intervals of 45 s). In panel (c), it could be distinguished a Doppler transient of positive sign (this corresponds to a red-shift) inside the domain of kernel A_{NW} (Figure **4-2**, (b)), followed directly by transient anomalies of both positive and negative sign appearing in the domains of kernels A_{SE} and A_{NW} in panel (d). The red arrows mark the location of the strongest Doppler transient, only visible in panels (b) and

(c). Sharykin et al. (2015) propose to associate such a Doppler feature with what they recognize as the general seismic source of the flare. However, this location is devoid of any significant indication in panels (b)–(d) of a source of acoustic emission in any part of the acoustic spectrum.

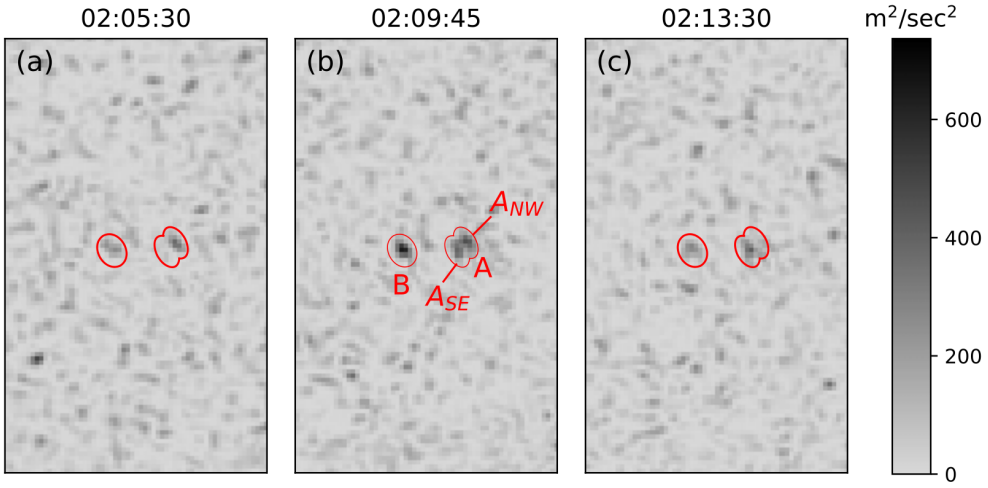

Figure **4-5**.: Temporal progression of acoustic transients from the source density at (10 ± 1) mHz of flare SOL20110730T02:09-M9.3. The emission from kernel A_{NW} in panel (a) precedes the one from A_{SE} in panel (b). Source B appears to peak halfway between peaks of kernels A.

Figure 4-5 shows the temporal progression of the source density of the acoustic transient in the $9 - 11$ mHz band. Evolution of the sources reveals a significant difference between the temporal progression of the two kernels of the western source. Signatures in a high frequency band, such as the (10 ± 1) mHz we presented, enjoy the benefits of better spatial resolution (see the top green dots on Figure 4-2), and so, sources can be discriminated rather than its counterparts at lower frequencies. Furthermore, as the bandpasses are 2 mHz width, this sets a temporal resolution to $1/(2\text{ mHz}) = 500$ s (8.3 minutes). This, somewhat ironically, obscures some of the transient nature of the acoustic radiation released. Figure 4-5 nevertheless shows that the temporal profile of kernel A_{NW} leads that of kernel A_{SE} by ~ 200 s. As seen from panel (b), in comparison to panels (a) and (c), source B seems to peak approximately halfway between the temporal peaks of kernels A_{SE} and A_{NW}. The timing of the acoustic-source density signatures represents an indication of when the emission reaches the pupil instead of when the seismic emission was emanated from its source.

Discussion

The improvement in spatial resolution allows to discriminate different morphologies of source distributions of transient seismic emission from acoustically active flares. We find a conspicuous compact transient acoustic source straddling a magnetic boundary. Since source A bifurcates into two kernels, one has to suspect that the sharp magnetic boundary located at

A has to play some dynamical role in the whole process, as well as it has to have some dynamical connection with the emission from kernel A_{SE} leading the one from A_{NW} by ~ 200 s. Due to the projection made on the Doppler maps, and since the location of the active region 11261 is 35° from the center of the solar disk ($\mu \approx 0.8$), the region of greater LOS magnetic field could not be entirely related to the region of greater magnetic flux density strength, nor the region of greater Wilson depression if present. The region in which kernel A_{NE} sits appears to be the neutral line separating opposite magnetic polarity (Polarity Inversion Line).

Moreover, of all of the regions that show strong transient perturbations in velocity, magnetic field, and apparent heating (white light), only from relatively compact regions a significant amount of transient acoustic energy is released into the solar interior, reinforcing mysterious qualities of other acoustic transients (Alvarado-Gómez et al., 2012); in addition, for some of the released acoustic transients in source A, there is a weak signature of perturbations in the outer atmosphere. This will be discouraging to hypotheses that propose to model transient acoustic sources as acoustic disturbances generated in the Sun's outer atmosphere that are simply transmitted downward through the source photosphere by the rules of linear acoustics. This is based on an understanding that the spectrum of the disturbances that arrived at length in the outlying pupil were simply inherited from that which was injected into the solar interior through the photosphere at the source location.

Another remarkable finding regarding the acoustic transient from the SOL2011-07-30T02:09 M9.3 solar flare, is the presence of a submerged source related to the kernel A. We now study the depth dependence of the acoustic transients in kernels A_{SE} and A_{NW} of Figure **4-3** based on the relative focus-defocus perspective in the acoustic egression maps (Lindsey et al., 2020).

4.1.2. Depth analysis

To follow an analysis on vertical depth dependence in computational holography, the submersion of some acoustic source is treated as a change in the optical focal plane where the field is being extrapolated (Lindsey and Braun, 1998, 2000). Figure **4-6** shows the change of the focal plane applied to the kernels A_{SE} and A_{NW} of Figure **4-3** (top row). The left panel at the 0 km stamp represents the placing of the focal plane directly at the solar surface. This is the same focal plane used for the ultra-impulsive analysis in subsection 4.1.1. From left to right, the focal plane lowers following an increase in depth of the acoustic field as a multiple of 420 km. As the focal plane submerges, the kernel A_{NW} is seen to defocus and fade, while its counterpart A_{SW} contracts into a compact region marked by the red arrow. From 1260 km this becomes the distinctly dominant feature, located 60 m southwest of its original centroid at 0 km.

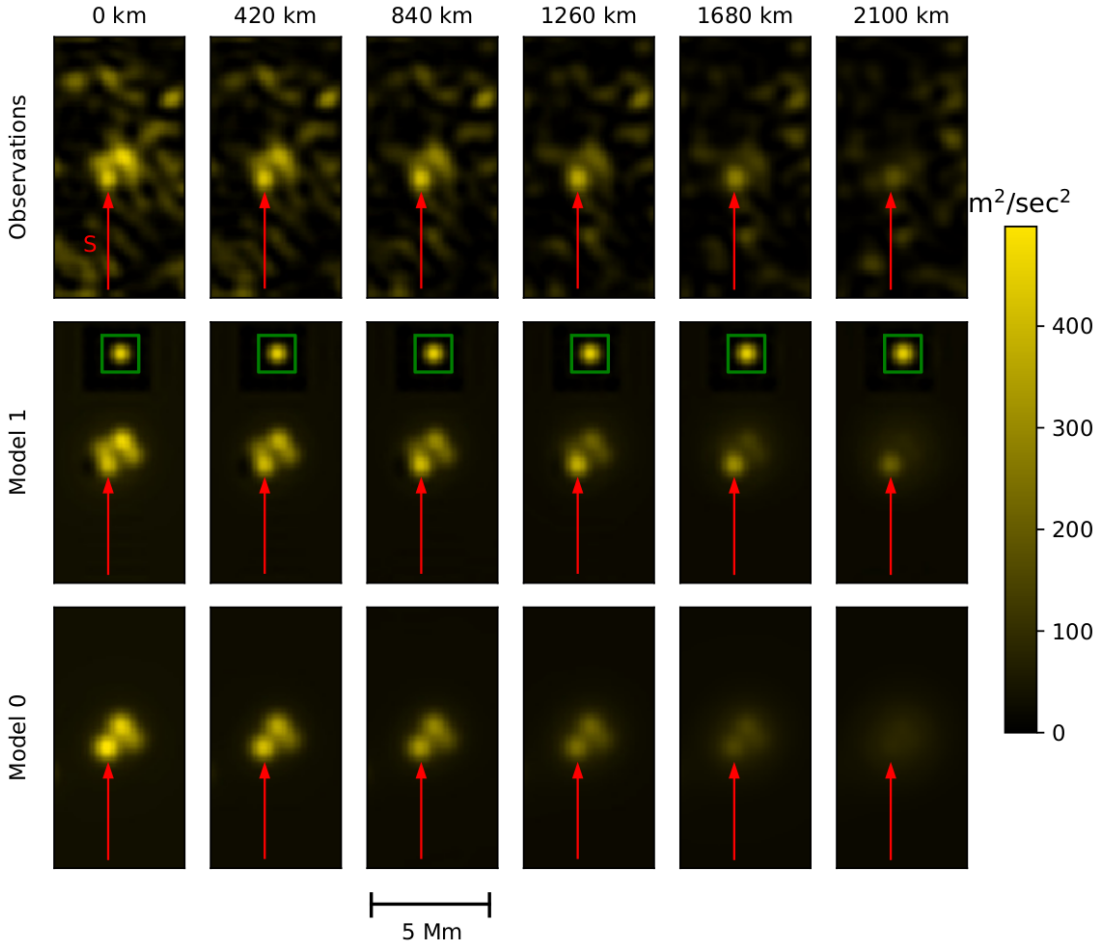

Figure **4-6**.: Top row: depth focus submersion from the acoustic signature labeled A in Figure **4-3**(b). The red arrow marks the location of kernel A_{SE} which is the dominant source beyond 1260 km. The middle row correspond to the density maps for the Model 1, modeled as two emitters at different depths of (200±100) km and (1150±120) km. The bottom row represents a control model, Model 0, whose deeper emitter is forced to be at the same depth of the shallow one.

The idea of this depth analysis is to show that the signatures in the top row of Figure **4-6** can be modeled by a simple model with acoustic sources that are dipole emitters distributed over a finite set of separate horizontal planes. In a first model we consider that most of the emission of kernel A_{NW} and some of the A_{SE} is distributed over a shallow plane. The primary component that contributes to the signature in kernel A_{SE}, to which the red arrow points in Figure **4-6**, is distributed in a second horizontal deeper plane respect to the first one. The acoustic emission from these source distributions is propagated outwardly downward, being after refracted back to the surface in the same way that the Green's function extrapolates the source field. Then, the same computational method is applied to the prescribed emitters as we did for the observations in the top row of Figure **4-6** and the source density maps of the the ultra-impulsive analysis. Subsequently the distance between the two emitters are

adjusted as well as its distributions in each plane, to minimize the mean square deviation in focal planes at depths 0.2 and 1.1 Mm. This corresponds to the "Model 1" in middle row of Figure 4-6. The best fit of these maps to those in the top row of Figure 4-6 was accomplished by fixing the shallow-source plane (200±100) km beneath the quiet photosphere, and the deep one (1150±120) km beneath the same.

For a control of Model 1, we now place the deep source at the same depth of the shallow one, 200 km beneath the photosphere. Then the same procedure of Model 1 is applied to generate the source density maps. This is labeled as "Model 0" and is shown in the bottom row of Figure 4-6. While the signatures from the surface up to 840 km depth shows an equivalent shape to the original source maps, from 1260 km this model does not match the signatures of kernel A_{SE} of that shown in the top row. Model 1 prescribes a planar distribution of emitters at depths (1150±120) km to account for the deep source, and (200±100) km beneath the solar surface. Although sources with some vertical degree of extension would be more realistic to model regarding the physics in 3D subphotospheric active regions, the essential result here is the finding of a component of flare-triggered transient seismic emission extended about a Mm beneath the solar surface.

Discussion

A highly compact acoustic signature embedded in the solar interior suggests a concentration of localized free energy provided with some measure of transient acoustic potentiality beneath the solar surface. The hypothesis is that the morphology of the source signature is indicative not only of the local compaction of the energy in the acoustic disturbance in the source region, but likewise of the original supply of free energy that fed it. The temporal relationship between the energy release and the solar flare of the associated event establishes a causal relationship between them. This can be seen as if the part of the disturbance caused by a flare penetrated into the subphotosphere from the above atmosphere acting as a trigger to release confined free energy in deeper layers of the solar interior.

On the question regarding the possible submerged free energy source to drive the acoustic transient, it is evocative to think on Lorentz forces playing a role in acoustic transient emissions. This argument relies upon the observations of strong magnetic fluxes in the regions where the acoustic transient takes place. It is possible that magnetic fields play a crucial role in the energy release of acoustic transients if some of the magnetic fluxes submerged in the solar environment stored sufficient energy to drive an acoustic transient. This would require a transfer from magnetic to acoustic energy, a condition met when the gas and magnetic pressures are comparable (Spruit and Bogdan (1992), Schunker et al. (2008) and references therin).

4.2. SOL2011-02-15T01:56 X2.2

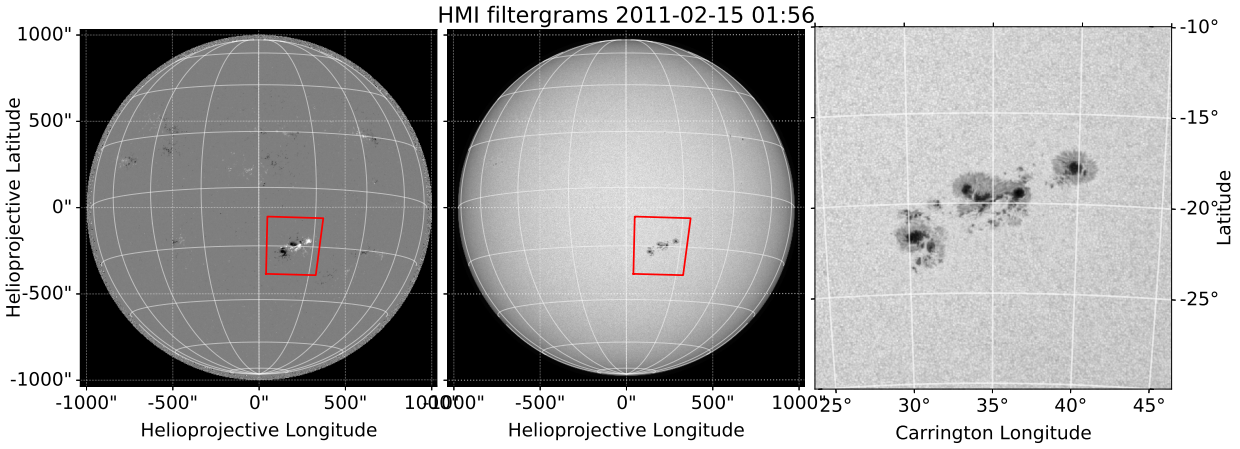

Figure **4-7**.: SOL2011-02-15T01:56 X2.2 solar flare from the SDO/HMI perspective. *Left panel*: LOS magnetogram scaled in the range [-1,+1] kG. *Middle panel:* Continuum intensity. *Right panel:* Postel projection of the NOAA 11158 shown in red on the full disk images. The timing associated to these maps is set at GOES the flare peak at 01:56 UT.

On 15 February, 2011, the Sun released the first X-class solar flare of the past solar cycle 24 observed by HMI (Figure 4-7). This event, hosted by the Active Region NOAA AR 11158 at heolioprojective coordinates X=178", Y=-211", reported a sunquake about 19 minutes after the peak in the GOES 1−8 Å band at 01:56:00 UT (Kosovichev, 2011).

Kosovichev (2011) suggests that such wave mechanical disturbance in the photosphere can

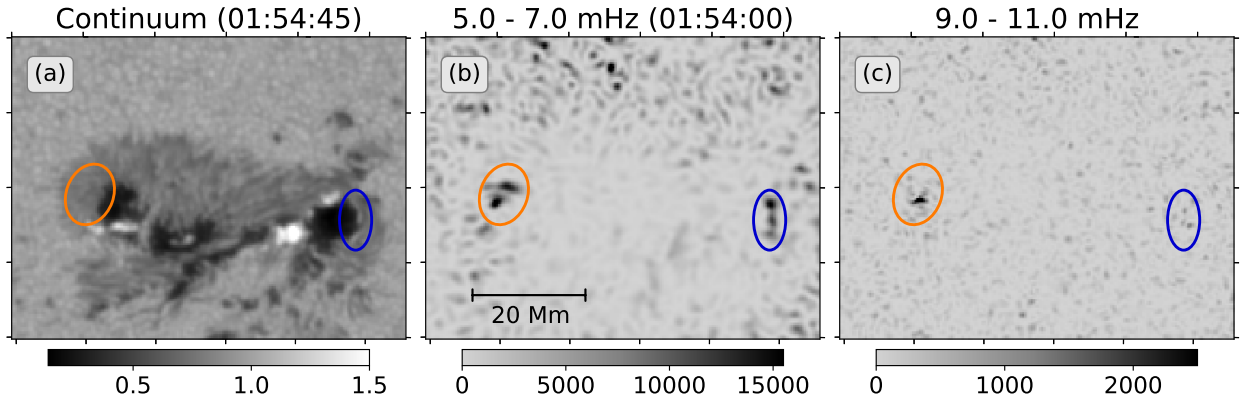

Figure **4-8**.: Location of the two acoustic transients in 6±1 and 10±1 mHz. The 6±1 mHz bandwidth shows, besides the conspicuous penumbral East component, a umbral-penumbral boundary signature with no clear indication in the 10±1 mHz one. Panel (a) shows the continuum intensity with superposed enhanced white light emission on it.

be understood as the result of a penumbral impact in a weak magnetic field region. However, using holographic techniques, Zharkov et al. (2011) found the acoustic emission detected by Kosovichev to be about 3 – 5 minutes prior to the peak of the HXR sources measured with RHESSI. They also found a second source mainly visible in the 6±1 mHz spectral bandwidth (panel (b) of Figure 4-8), both of which show no spatial correlation to the sources of HXR emission in 12 – 25 and 6 – 12 keV. These observations led Zharkov et al. to exclude particle precipitation as the primary trigger for any of the two detected sunquake wavefronts. Instead, since the endpoints of the sigmoid-like structure rely on the same place of the transients, they suggest that these seismic signatures are driven at the footpoints of the flux rope eruption.

On the other hand, Alvarado-Gómez et al. (2012) calculated the work done by the Lorentz force on the main acoustic source of the 6±1 mHz according to Hudson et al. (2008) and Fisher et al. (2012). They estimated the work to account only for the 6% of the total energy released by the transient which can be up to 23% if is considered a null vertical ΔB component. Here, in a procedure similar to the SOL2011-07-30T02:09 flare, we calculate high-frequency acoustic egression maps to the projected active region in Figure 4-7, describing its depth dependence and relationship to LOS observables.

4.2.1. Ultra-impulsive Analysis

To construct egression maps we used computational holography over the projected enclosed region of Figure 4-7. Given the extent of the sunquake wavefront, we used an annular pupil with an inner radius of 7 Mm and outer radius of 84 Mm centered on the holographic Carrington Longitude and Latitude coordinates 34.59° and -19.80°, respectively. The spectral band 6±1 mHz in Figure 4-8(b) shows two acoustic transients located in their respective penumbrae with no spatial correlation to the emission in white light at Fe-I 6173Å from the X2.2 flare of panel (a). The 2 mHz bandwidth centered at 10 mHz of panel (c) exhibits only a sharper Eastern component while all of the emission from the Western one is at least no greater than three times the standard deviation of the background to be considered as signal. The signature of the East source in panel (c) is considerably smaller than that of (b), which actually seems to be composed by two separate kernels. However, while the transient is more compact, it enjoys of better spatial resolution at about 760 km (Martínez et al., 2020), and describes faster processes happening in the solar environment.

Source density map at 9±11 mHz in Figure 4-9(a) presents a maximized view of the East component of Figure 4-8(c). The transient has a shape close to an oval with geometry of ∼2.2 Mm width and ∼1.0 Mm height. A red ellipse encompasses the signature to reference its location with the observables provided by HMI. The penumbra where this transient takes place corresponds to a LOS magnetic field region smoothly spanning from -700 to ∼-800 G in panel (b). The Doppler map in panel (c) represents the difference between the field at 01:51:00 UT and one frame forward in time. This Doppler change indicates a red-shift of

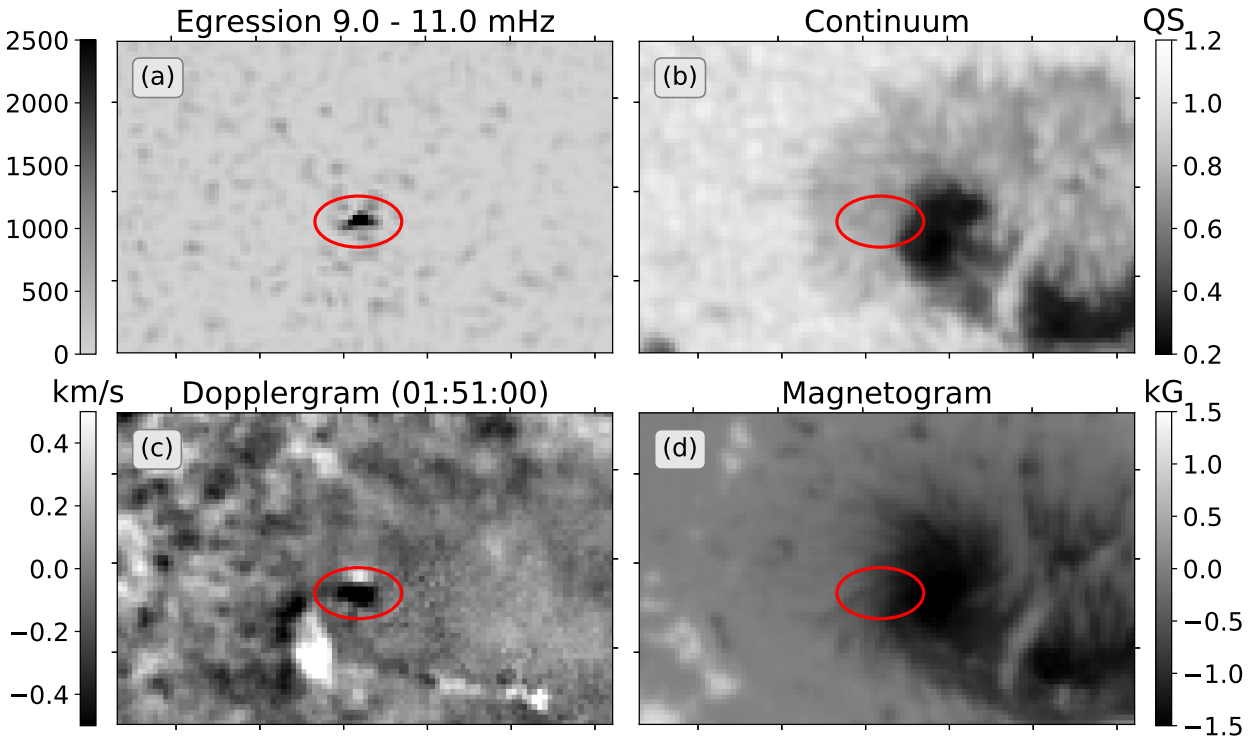

Figure **4-9**.: Location of the acoustic transient of Figure 4-8(c) released by SOL2011-02-15T01:56 X2.2 calculated with computational helioseismology. Panel (a) represents the 10±1 mHz spectral band of the egression power, where a noticeable acoustic transient peaks at the location of the penumbra of the sunspot shown in panel (b). Panels (c) and (d) mark the site of the transient related to the Doppler change and magnetic field, respectively. All times except for the Doppler filtergram are set to the flare peak at 01:56 UT.

about -800 m/s in the integrated region. This change takes place approximately 5 minutes before the flare peak, associated to a transient downward with minimum at 01:52:30 UT. At the South East of the oval there is a region with a blue-shift which is devoid of any acoustic signatures and does not seem to manifest any conspicuous change in intensity or magnetic field. This compact source does not seem to be composed of several individual kernels, although its signature is significantly greater than its counterpart found by Martínez et al. (2020).

Temporal progression of the single source is displayed as snapshots in Figure 4-10. To contrast possible variations with succeeding or preceding frames, the green circle centered at the centroid of panel (c) is overplotted in the others. No significant changes in morphology nor displacements are discernible as the acoustic source evolves. In fact, it is likely to keep a similar shape along its emission process, showing definitely a strong compact source.

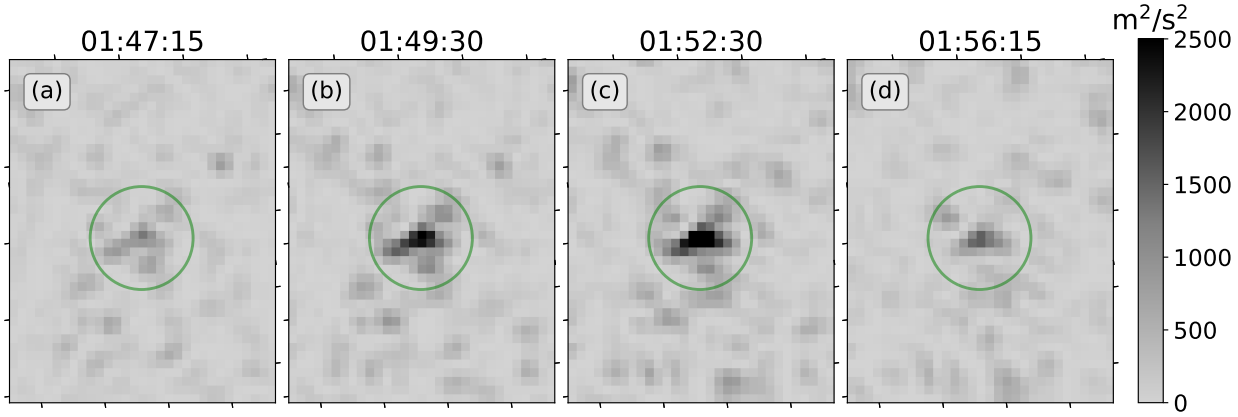

Figure **4-10**.: Temporal progression of the transient of Figure **4-9**(a). The green circle encompasses the transient whose center is properly located at the center of the centroid that of panel (c). The snapshots do not show significant changes between frames.

4.2.2. Depth analysis

To study the depth dependence of the acoustic transient found in the 10±1 mHz bandpass, we employ a wave mechanical focus-defocus diagnosis similar to the one previously presented in the SOL2011-07-30T02:09 solar flare. Figure **4-11** represents a progressive sinking of the horizontal sampling surface every 600 km. The remarkable compact transient found in panel (a) of figure **4-9** at 0.0 km is shown to have a great vertical submersion up to ∼2 Mm. A red arrow points to the site where the seismic acoustic signal shows its maximum emission as depth increases. From this depth structure, we see how the morphology of the transient at 0 km changes, where only a fraction of the original shape of energy release is discernible in deeper layers. The faded acoustic source in 3 Mm is the defocused and blurred image from a transient located above it. In the case of signatures up to a depth of ∼2 Mm, starting from the solar surface, they present a sharp diffraction-limited image of the acoustic source, while for the 2.4 Mm signature it seems to be rather some out of focus view of an upper signature.

The reason to sequentially extrapolate acoustic maps up to 3 Mm is based upon an argument of computational acoustic holography. A a single egression map calculated some distance beneath the solar surface may be inadequate to account for the location of the acoustic transient given the diffuse (defocused) nature of the method applied to sources out of their focal plane (Lindsey and Braun, 2000).

For each frame in Figure **4-11**, the time in which the maps are referenced determine the greatest emission of energy of the acoustic transient respect to its surroundings. The peak at each depth arises at succeeding time frames around the flare maximum at 01:54:00 UT. It can be thought as if some trigger could have a repercussion on the apparent downward energy

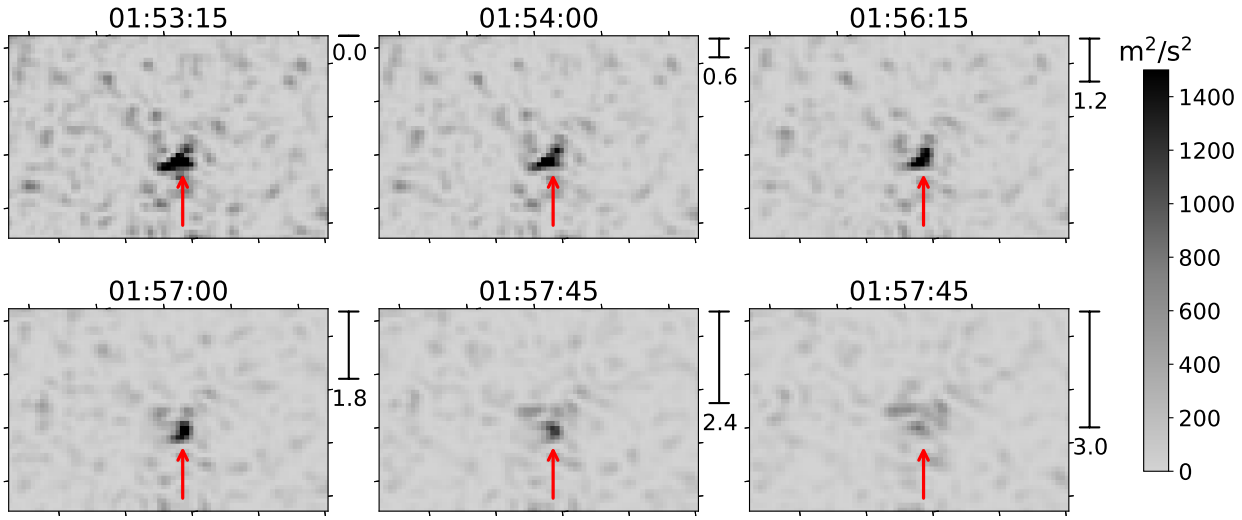

Figure **4-11**.: Vertical submersion of the acoustic transient at 10±1 mHz of Figure **4-9**(a). The right vertical bars indicate the focus depth of the computational holography measured in Mm beneath the photosphere. It suggests an acoustic source immersed in up to 2000 km. The time stamps on top of each frame indicate when the emission from the source region reached a maximum.

release of the acoustic source into deep layers of the solar interior. A direct comparison with the source of SOL2011-07-30-02:09 of top row of Figure **4-6** shows this acoustic transient of the X2.2 flare to be not only of greater signature emission but also with seeming deeper vertical extent embedded in the solar interior, approximately up to one full Mm into the solar interior.

Discussion

We report a second acoustic source extending well beyond 6±1 mHz with some degree of vertical extension inside the solar interior in addition to that one found by Martínez et al. (2020). In this instance, the acoustic transient was found to lie in the penumbra of the active region where the magnetic field spatially presents a smooth variation of 100 G. The LOS velocity in the source region indicates a red-shift associated to a photospheric impact of about 800 m/s, remarkably different to what was discovered in SOL2011-07-30T02:09 in which the strongest transient was found to lie a couple Mm at West of the composite kernels. The Doppler signature in this event can be thought to have a dynamical relationship with the acoustic sources emanated by SOL2011-02-15T01:56.

It is important to notice that, while the spectral bandwidth of 2 mHz centered at 10 mHz provides us with a better spatial resolution in the source maps, the bandwidth of 2 mHz ensues a temporal resolution in the source density maps of $\Delta t = 500$ s. That is, the acoustic

signatures could be dilated in time long before and after the energy release, even if this process took place in an arbitrarily short amount of time. However, we take advantage of time differences between maximum signal emission, which in the case of this event showed almost no compelling variation.

The acoustic source manifested to be submerged in the solar interior as well. According to a focus-defocus procedure of diffraction-limited images, it is likely to be immersed up to ∼2 Mm beneath the solar surface. The signature focuses on a tight region denoted by the red arrow of Figure 4-11 which differs from the morphology of the source at 0 Mm. Depth focal planes along with time sequence acoustic maps raise the idea of a single compact 3D kernel transient releasing energy into the solar interior being after refracted back into the surface as a visible seismic signature.

4.3. Three M-Class solar flares from NOAA 11515

We now examine three solar flares emanating from active region NOAA 11515. This particular active region witnessed several M- and C-Class solar flares, many of which hosted sunquake events detected by time-distance diagrams Buitrago-Casas et al. (2015).

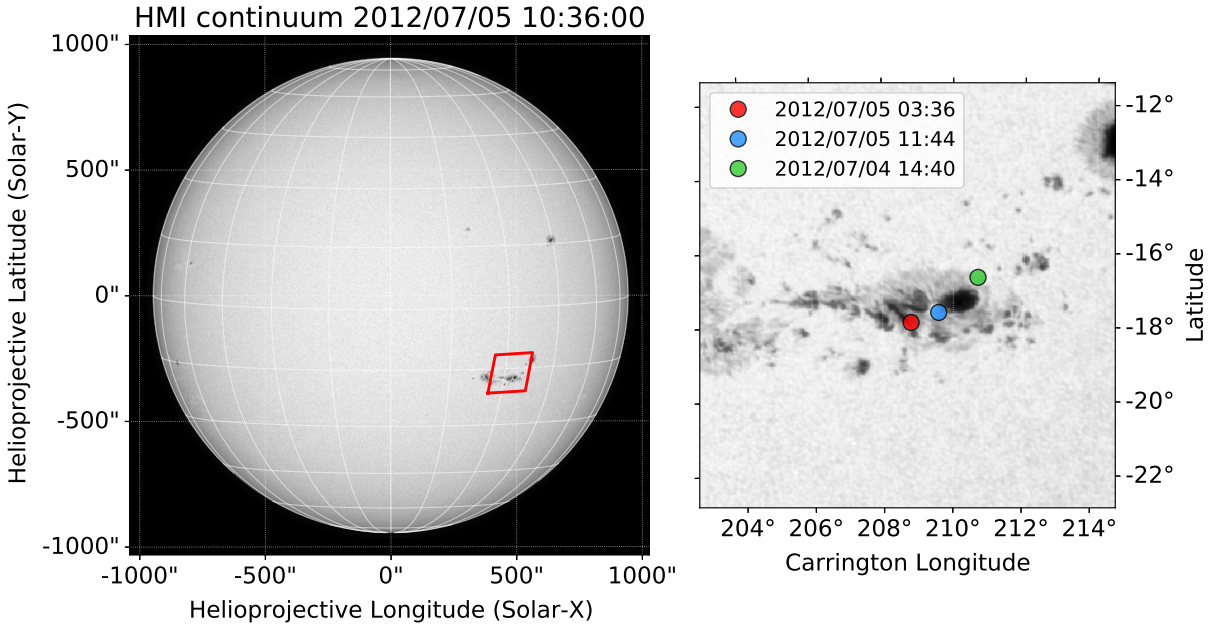

Figure **4-12**.: NOAA 11515 as seen from HMI's continuum Fe I line on 2012/07/05 at 10:36:00 UT. The location of this active region is at helioprojective coordinates $X = 439$", $Y = -343$" which results in a location from the solar center of $\mu = 0.60$. The Postel projection of the red polygon in the full disk image shows the approximate location from where the different solar flares were projected.

Figure **4-12** shows the location of the active region in a continuum solar disk image from HMI, along with the Postel projected map of the region. Color dots in the right panel indicate the places where the tangent plane of the Postel projection is set for the solar flare events. The selected events are: SOL2012-07-05 03:36 of class M4.7, SOL2012-07-05 11:44 of class M6.1, and the M1.3 class SOL2012-07-04 14:40 solar flare.

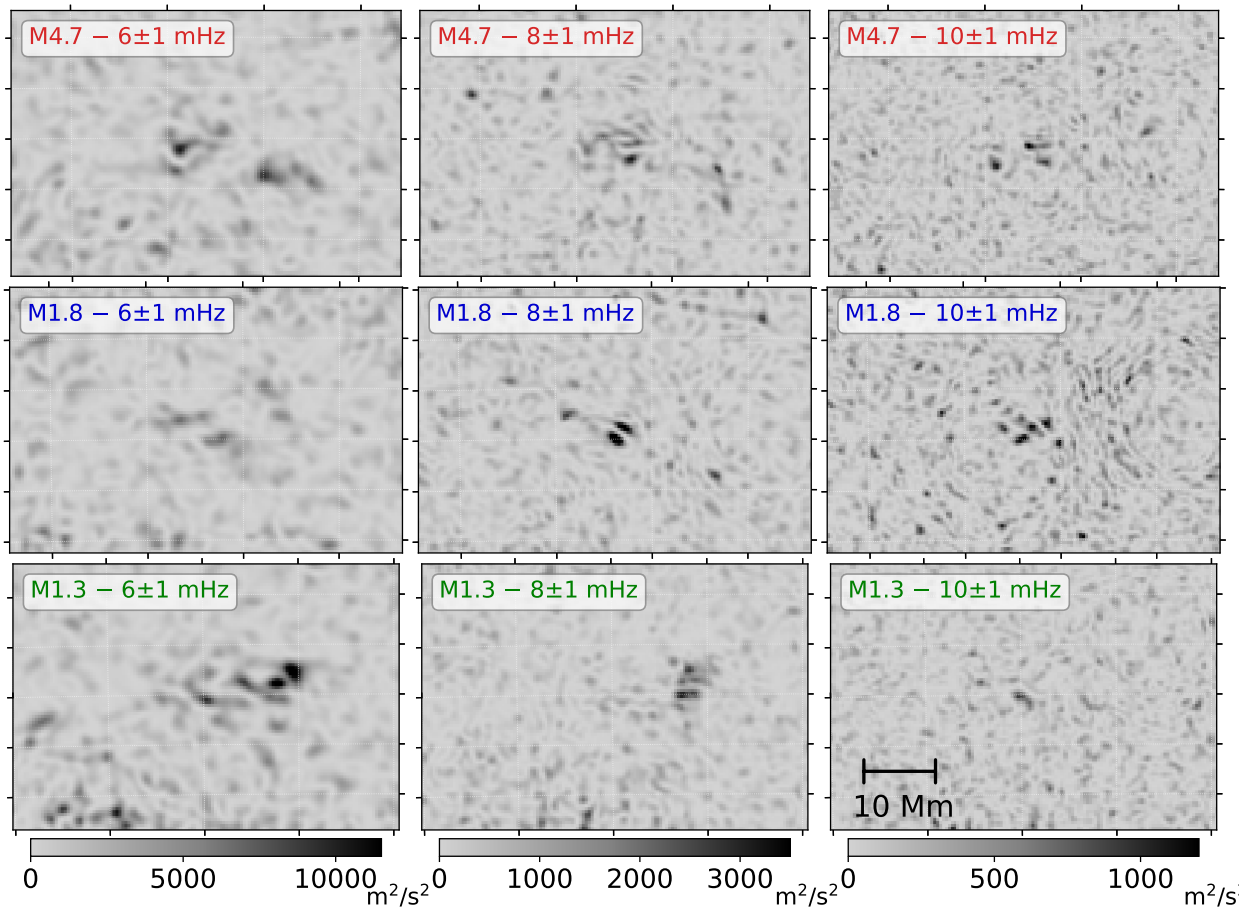

Figure **4-13**.: Source density maps for three solar flares of NOAA 11515 at bandpasses 6±1, 8±1, and 10±1 mHz. The rows denote holographic calculations for a single flare. The color range for each frequency is located in the colorbar at the bottom of each column. The bottom right panel indicates the scale which is the same for all frames.

The signatures from 5 to 11 mHz evenly spaced with a spectral resolution of 2 mHz are shown for the three solar flares in Figure **4-13**. Top row of Figure **4-13** shows the source density maps for SOL2012-07-05 03:36 (M4.7). It is noticeable transient emissions for the selected bandpasses. The middle row shows the transients for what in principle is the SOL2012-07-05 11:44 M6.1 solar flare however, no visible signature is appreciable. Nevertheless, there is an acoustic transient (with remarkable emission in the 8±1 mHz) which is also visible in (9-11) mHz for the same acoustic region at 10:48:00, approximately 56 min before the original

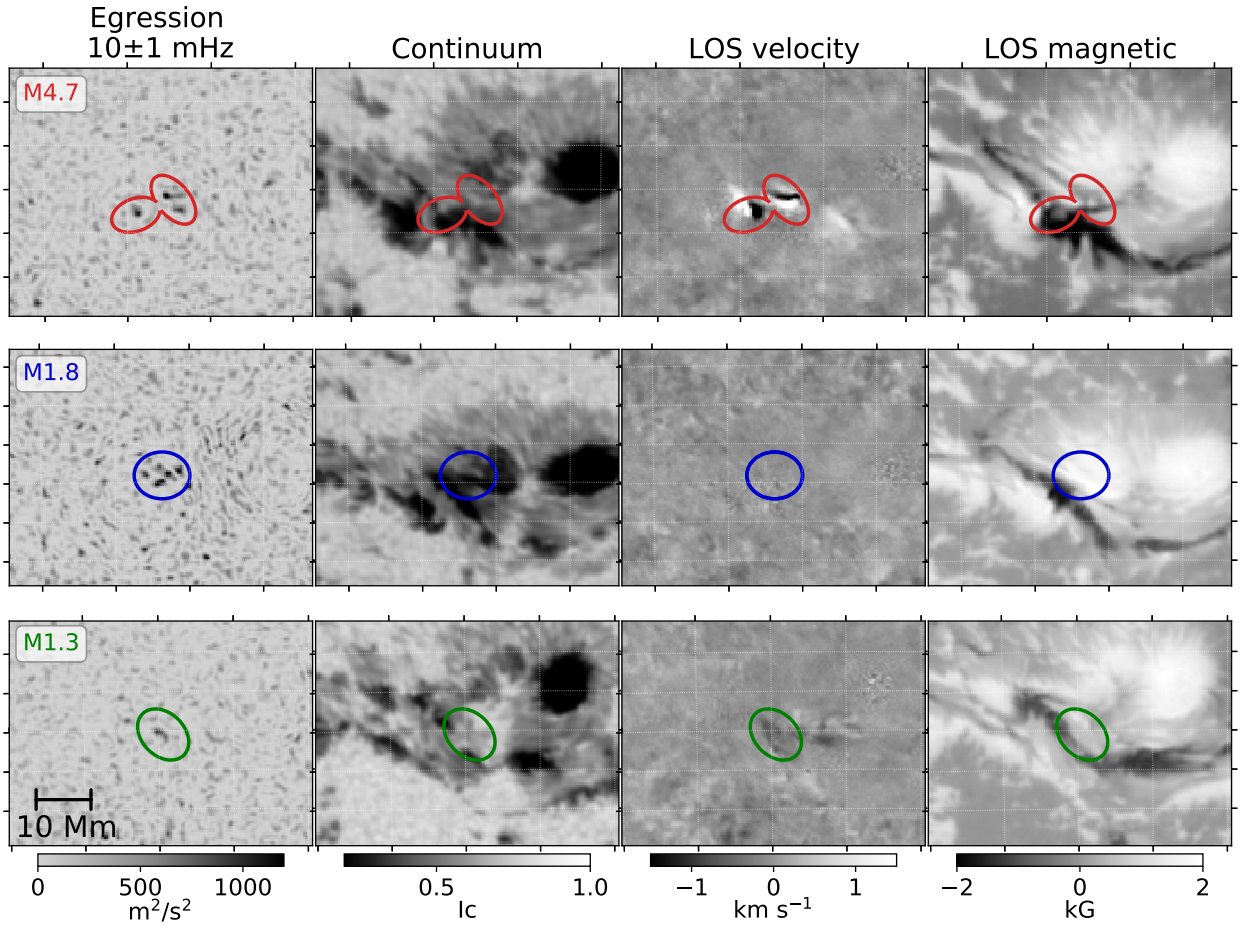

Figure **4-14**.: Position of the signatures of 10±1 mHz on HMI observables. The second column is the normalized intensity continuum. The third column represents the LOS velocity transient between the flare peak and one successive image in the range [-1.2,1-2] km/s. The last column shows the LOS magnetic field measured in kG.

flare. According to the GOES X-ray satellite in the 1 – 8 Å passband, the flux at this time is an M1.8-Class solar flare. The bottom row shows the field extrapolations for SOL2012-07-04 14:40 M1.3, where a strong signature is visible in 6±1 and 8±1 mHz. In 10±1 mHz, the signature is barely recognizable and is located right in the center of the map.

Figure 4-14 shows the location of the acoustic sources in column 3 of Figure 4-13 on top of HMI maps. The top row, associated to the M4,7 event, shows a mechanical relationship with both the change in LOS velocity and the compact distribution of LOS magnetic field in the enclosed region. However, this Doppler change is not remarkable for the M1.8 and M1.3 flares. Furthermore, the magnetic field of these two acoustic transients smoothly changes along each identifiable kernel. The location of the M4.7 and M1.3 events (top and bottom rows) lies on a penumbral region, while for the flare M1.8 it has kernels located in the

umbra-penumbra penumbra of the sunspot.

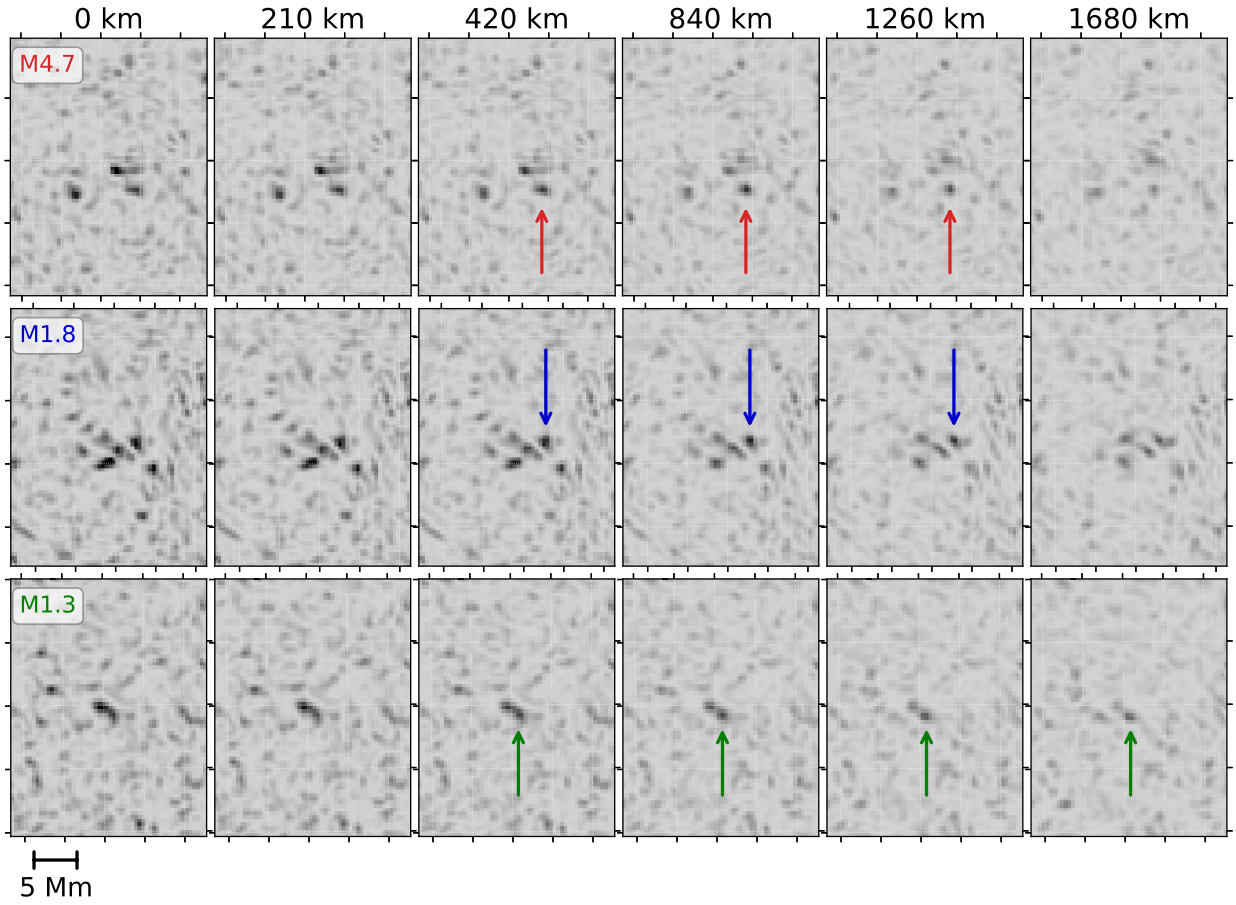

Figure **4-15**.: Field extrapolations at different focal planes below the solar surface. The columns denote the depth at which the calculations are made ranging from 0 km to 1680 km. The rows indicate the depth calculation for each event, the distance of which is labeled at the bottom left. The acoustic power maps of the top and middle rows range from 0 to 1200 m^2/s^2, while for the bottom row it ranges from 0 to 900 m^2/s^2.

Source density maps extrapolated at different depths are shown in Figure **4-15**. It is important to note here that, regarding the focus-defocus diagnosis, the sources appear to have a vertical extension. The bottom row has been remapped into the amplitude range 0 to 900 m^2/s^2 to illustrate its morphology at layers below the solar surface. The green arrow points to the location of a dominant feature beneath 840 km, which shows two separate kernels. The red arrow in the top row and the blue arrow in the middle one represent the acoustic transients with the sharpest component at 1260 km.

5. Numerical simulation

In this chapter we present a numerical magnetohydrodynamic (MHD) simulation to test the emergence of an acoustic transient driven in the solar interior. We describe the possibility of thermodynamical disturbances in the magnetic field to be the trigger of such disturbances. For this purpose, we use the PLUTO code to solve the set of conservative equations attached to a solar model structure.

5.1. The PLUTO code

PLUTO (Mignone et al., 2007, 2012) is a shock-capturing Godunov-type numerical scheme written in C/C++ intended to solve high-Mach number problems in compressible flow dynamics. The code offers a Python written user interface in which separate parts of the numerical and physical parameters can be effortlessly set up thanks to its modular architecture.

PLUTO solves the following system of equations related to the conservation laws:

$$\frac{\partial \boldsymbol{U}}{\partial t} = -\nabla \cdot \boldsymbol{T}(\boldsymbol{U}) + \boldsymbol{S}(\boldsymbol{U}), \tag{5-1}$$

where $\boldsymbol{U}$ represents a vector of conserved quantities, $\boldsymbol{T}(\boldsymbol{U})$ is the rank-2 flux tensor and $\boldsymbol{S}(\boldsymbol{U})$ is related to the source term. The flux tensor accounts for the hyperbolic flux (wave propagation) and the parabolic (diffusive physics) terms. The standard version of the code employs a Finite-Volume Method (FVM) to integrate the set of conservation laws above, although high-order Finite-Difference schemes can be enabled. The code is distributed under the GNU general public license, and can be downloaded freely at http://plutocode.ph.unito.it/ along with its manual. For this work, we used the updated version 4.4-patch1 of November 2020.

The vector quantities in equation (5-1) depend on the physical module to be selected. Since the purpose of this study is based on the simulation of thermodynamic variables in the presence of magnetic flux densities, we take advantage of the MHD magnetohydrodynamic module. This module solves the ideal/resistive non$-$relativistic MHD equations. In this formalism, the set of equations (5-1) are written:

$$\begin{aligned}
\frac{\partial \rho}{\partial t} &+ \rho \nabla \cdot \boldsymbol{v} + \boldsymbol{v} \cdot \nabla p &&= 0 \\
\frac{\partial \boldsymbol{m}}{\partial t} &+ \rho \boldsymbol{v} \cdot \nabla \boldsymbol{v} - \frac{1}{4\pi}\big[\boldsymbol{J} \times \boldsymbol{B}\big] + \nabla p &&= -\rho \nabla \Phi + \rho \boldsymbol{g} \\
\frac{\partial \boldsymbol{B}}{\partial t} &+ \nabla \times (c\boldsymbol{E}) &&= 0 \\
\frac{\partial p}{\partial t} &+ \boldsymbol{v} \cdot \nabla p + \rho c_s^2 \nabla \cdot \boldsymbol{v} &&= 0
\end{aligned} \tag{5-2}$$

where ρ represents the density of mass, $\boldsymbol{v}$ its velocity, $\boldsymbol{m} = \rho \boldsymbol{v}$ the momentum per unit volume, p the gas pressure, $\boldsymbol{B}$ the magnetic field vector, and $c_s^2 = \sqrt{\Gamma p/\rho}$ the adiabatic sound speed in the case of the ideal equation of state. The first equation is related to the mass continuity with the compressible condition. The second equation represents the momentum equation for a magnetically active medium, where the magnetic field follows Ampère's law:

$$\boldsymbol{J} = \frac{c}{4\pi}(\nabla \times \boldsymbol{B}) \tag{5-3}$$

The right hand side of the momentum equation relates to body forces written as functions of the time-independent gravitational potential $\Phi(\boldsymbol{r})$ and gravity $\boldsymbol{g}(\boldsymbol{r})$. The third of equations (5-2), Faraday's law, together with Ampère's law, yield the induction equation.

In the present work, the plasma is treated with a large electrical conductivity, i.e., the magnetic Reynolds number can be numerically considered as infinity. Then, the electric field is:

$$c\boldsymbol{E} = -\boldsymbol{v} \times \boldsymbol{B}. \tag{5-4}$$

The last of the equations (5-2), referred to the energy conservation takes into account the calorically ideal gas approximation, where the internal energy, e, yields the closure of an equation of state in the magnetohydrodynamic equations:

$$\rho e = \frac{p}{\Gamma - 1}, \tag{5-5}$$

where Γ is the adiabatic exponent for an ideal gas. For a monatomic gas – in a region where the gas pressure far exceeds the radiation pressure –, the ratio of heat capacities at constant pressure and volume takes the value of 5/3. This is close to the value of the adiabatic exponent Γ_1 in regions close to the solar photosphere.

On the other hand, when inserting equation (5-4) into (5-2), arises the expression $\nabla \cdot \boldsymbol{B}$. The control of the condition $\nabla \cdot \boldsymbol{B} = 0$ adds another constrain to the solution of equations (5-2), and depends on the formalism and the physics module used.

5.1.1. Numerical Scheme

The following items relate to the basic structure to construct the header of the simulation. Further details can be reviewed in the userguide provided by the module.

- **Physics**: *MHD*
- **Geometry**: *POLAR/CARTESIAN*. The choice depends on how the magnetic field is set in the solar interior.
- **Body Force**: *VECTORIAL*. Since the plasma is embedded in a magnetized solar interior, a magneto-hydrostatic equilibrium condition is needed. This guarantees the plasma to be confined inside the simulation box preserving the profiles given by density and pressure gradients. This is equivalent to solve for the gravity in the second of equations (5-2).
- **Reconstruction**: For a spatial interpolation of volume averaged quantities, we select a piecewise TVD *LINEAR* reconstruction. It is a 3-point stencil, with a 2^{nd} order accuracy in space.
- **Time stepping**: A second order *RK2* TVD Runge Kutta timestepper is used. It evolves as:

$$\boldsymbol{U}^{*} = \boldsymbol{U}^{n} + \Delta t^{n} \boldsymbol{\mathcal{L}}$$
$$\boldsymbol{U}^{n+1} = \frac{1}{2}\left(\boldsymbol{U}^{n} + \boldsymbol{U}^{+} * + \Delta t^{n} \boldsymbol{\mathcal{L}}^{*}\right)$$

  where $\Delta t^{n} = t^{n+1} - t^{n}$ is the time step and $\boldsymbol{\mathcal{L}}$ is the spatial operator at the right hand side of equation (5-1).
- **Riemann Solver**: Since the onset of the numerical simulation involves discontinuity regions and strong variations until a relaxation time, we decided to use a *tvdlf* scheme for the sake of code robustness. This is a diffusive solver and is useful to avoid zones of negative energies.
- $\nabla \cdot \boldsymbol{B}$ **Control**: The constrain used to control this condition is the *EIGHT_WAVES* formalism. Here, the magnetic field has a cell-centered average representation. This method keeps $\nabla \cdot \boldsymbol{B} = 0$ at a truncation level, not to the machine accuracy.

In addition to the set of parameters described above, a vector of primitive quantities $\boldsymbol{U}$ has to be specified as initial conditions in the simulation. The variables specify the scalar density and pressure and the 3-dimensional velocity and magnetic field vectors. It is also possible to specify the temperature instead of the pressure or density via the equation of state. To avoid overflow/underflow errors in the computation, PLUTO offers the possibility to normalize the variables avoiding the use of large/small floats.

5.2. Physics Setup

We now describe the physical parameters of the simulation. The idea is to embed a magnetic field flux tube in some background model of the solar structure.

5.2.1. Background model

To model immersed magnetic flux tubes beneath the photosphere, we use the Solar Standard Model from Christensen-Dalsgaard (Model S, Christensen-Dalsgaard et al., 1996). This model can be obtained at https://phys.au.dk/~jcd/solar_models/. It provides a set of limited variables containing the density, pressure, sound speed, temperature, and the adiabatic exponent as functions of the normalized solar radius.

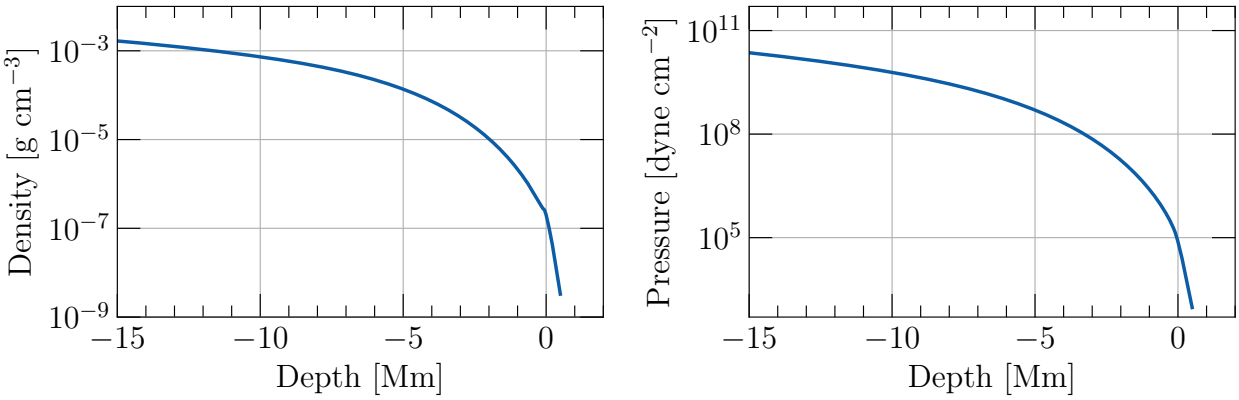

Figure **5-1**.: Density and pressure in the solar interior according to Model S of Christensen-Dalsgaard et al. (1996).

Figure 5-1 shows the scalar variables to be considered in the vector of primitive variables in equations (5-2). At a depth of $z = 0$ Mm, since there is an important change in the local medium, we interpolate a smooth varying function. The model calculates the structure variables up to ∼500 km above the $z = 0$ Mm plane.

Model S, though is convectively unstable, allows us to set adequate conditions in the solar interior to evolve magnetic fields; the temporal range and the spatial extent of the simulation is just to maintain a vertical tube stable for several hours, and no clear bouyancy-driven flows are measurable. In this work, we go only as far to simulate the solar structure up to 10 Mm in depth.

5.2.2. Magnetic flux tube

Since Model S accounts for a solar structure with no magnetic fields, we employ a theoretical approach to embed a magnetic tube into it.

We consider the simple model of a straight, axis-symmetric poloidal magnetic field tube with azimuthal symmetry and constant cross-section following the review of Moradi et al. (2010). This is a model which takes into consideration the equilibrium condition of the momentum equation, and is referred as a Magneto-Hydrostatic Model. Solving for this condition, according to equation (5-2) yields:

$$-\nabla p + \rho \boldsymbol{g} + \frac{c}{4\pi}\big[(\nabla \times \boldsymbol{B}) \times \boldsymbol{B}\big] = 0. \tag{5-6}$$

Several constrains can be applied to solve for $\boldsymbol{B}$ in equation 5-6. The approximation used in this simulation is the so called *self-similar field*. We follow a similar procedure taken in section 4.2 of Moradi et al. (2010).

According to the self-similarity field, the magnetic field in cylindrical coordinates is written as:

$$B_z(r,z) = f(\zeta)B_0(z), \tag{5-7}$$

$$B_r(r,z) = -\frac{1}{2} r f(\zeta)\frac{dB_0(z)}{dz}, \tag{5-8}$$

being $\zeta = r\sqrt{B_0(z)}$, and $f(\zeta)$ a radial profile of the magnetic tube. Inserting radial and vertical equations (5-7) and (5-8) into the equilibrium condition (5-6), results for the horizontal component:

$$0 = -\frac{\partial p}{\partial r} + \frac{B_z}{4\pi}\left(\frac{\partial B_r}{\partial z} - \frac{\partial B_z}{\partial r}\right).$$

Integration of the equation above from 0 to a large value yields:

$$\Delta p(z) = p_e(z) - p_i(z) = -\frac{1}{8\pi}\left(\frac{\Phi}{2\pi} y \frac{\mathrm{d}^2 y}{\mathrm{d}z^2} - y^4\right), \tag{5-9}$$

with $y = \sqrt{B_0(z)}$ and Φ the magnetic flux. The values $p_e(z)$ and $p_i(z)$ are the pressure for the non-magnetized region and for the inside of the flux tube, respectively. Selecting a slowly varying function of the magnetic field, at least for greater depths, the equation (5-9) can be approximated to:

$$p_e - p_i = \frac{B_0^2}{8\pi}, \tag{5-10}$$

condition known as the lateral balance pressure condition. The pressure outside, p_e, is given by Model S. For the pressure inside the tube, we can approximate the vertical component of equation (5-6) as:

$$\frac{dp_i}{dz} = \rho_i g, \tag{5-11}$$

where ρ_i follows:

$$\rho_i(r,z) = s\rho_e(z)\big[1 - \xi(r)\big], \qquad \xi(r) = \frac{1}{2}\left\{1 - \tanh\left[\left(\frac{r}{R} - 1\right)b\right]\right\}. \tag{5-12}$$

Here, R is the radius of the flux tube, and s is a fraction which expresses the density of the tube as a fraction of that of Model S. $\xi(r)$ represents a function which makes a smooth transition between the exterior and interior of the magnetic flux, with b representing the width of this transition layer. Calculations for the density, eq. (5-12), pressure eq. (5-11), and magnetic field eq. (5-10) at $z = 0$ Mm are shown in Figure **5-2**

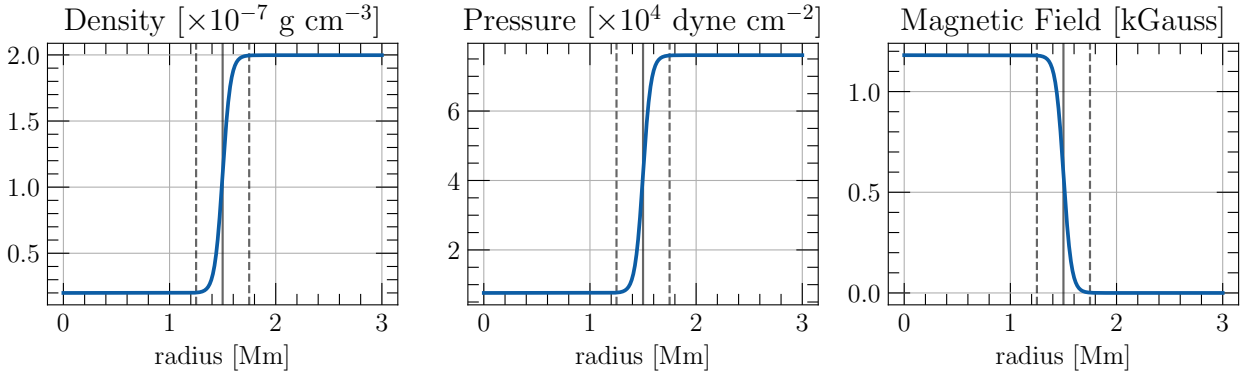

Figure **5-2**.: Radial profiles of the magnetic flux tube. The fraction s here has been set to 10%. The left side of the plots represent the magnetic flux tube, with a radius set to $R = 1.3$ Mm. Dashed vertical lines represent the width b in which the variables smoothly vary from the outside of the tube to the inside.

With this setup, the magnetic field strength has the vertical profile as shown in Figure **5-3**. It corresponds to a magnetic field that increases its magnitude with depth, reaching values of order of magnitude 10^5 G at 15 Mm. This magnetic field agrees with semi-empirical models of the magnetic field (see Cameron et al. (2011) and references therein).

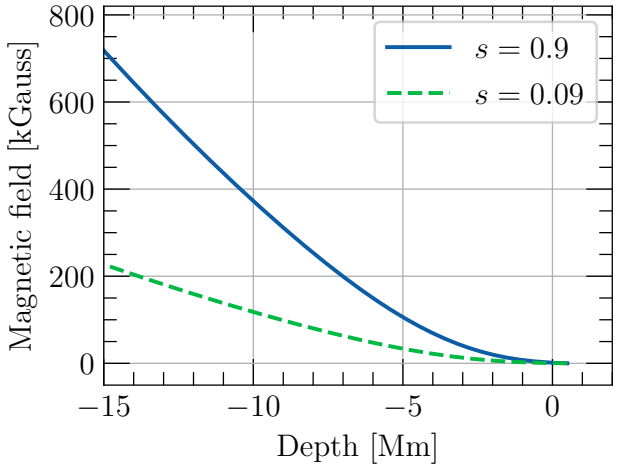

Figure **5-3**.: Magnetic field as function of depth for a self-similarly scheme according to equation (5-10). The solid blue curve is for a fraction $s = 0.9$, while the dashed curve shows the magnetic field for $s = 0.09$. For depths greater than 5 Mm, it can be approximated as a linear function.

5.3. Simulation

5.3.1. 2D structure

The simulation consists of a rectangular box with with defined boundary conditions as explained in the following. Since the gravity is set in the vertical direction, we use reflective boundary conditions in the bottom and top walls. In addition to these vertical boundaries, we also employ "cooling" blocks near the walls in a procedure similar to that one used by Cameron et al. (2011). They consist of thick layers whose usefulness is to prevent upper and lower reflections from perturbed waves into the region of interest. They also help to stabilize the magnetic field structure preserving its vertical profile as in Figure **5-3**. These layers act as an absorptive material by strongly attenuating wave energies. On the other hand, the lateral walls have an outflow boundary condition. In contrast, this boundary ensures the flow to escape if needed and not to be accumulated in the simulation box compromising the resulting waves. The selection above encloses the plasma in the computational grid and shows stability upon considerable changes related to the beginning of the code until a relaxation time is reached.

In this subsection, before applying magnetic field instabilities, we test the stability of the simulation (stability of the magnetic field flux tube) as well as a pressure driven perturbation in the background model.

Stabilization

In order to examine the stability of the chosen scheme, we run a first trial up to 90 min. This helps to verify the identity of the thermodynamical variables as time evolves. For this purpose, we select a simulation box with dimensions [-8.0,8.0] Mm in the x-direction evenly distributed across 300 pixels. This ensures a spatial resolution of 53.33 km/pix. In the z-direction, the grid has dimensions [-8.0,1.4] Mm along 300 pix for a vertical resolution of 31.33 km/pix. The upper block of attenuating waves has a width of $\sim$900 km starting from $z = 500$ km, while the lower block starts from -6 Mm to have 2 Mm of width.

Figure **5-4** shows two snapshots of the pressure, density and magnetic field. The top row indicates the onset of the simulation at 00:00:00, while the second row shows its evolution at 01:30:00. Since we selected two upper/lower additional layers to prevent destabilization and wave reflections, the magnetic field also freezes in those layers, although has no considerable effects in the evolution. The vector field in the bottom left indicates the velocity field for such time. For visualization, the images are colorbar-plotted in logarithmic scale, being the black color the region above $z = 0$ Mm for density and pressure. The boundary layers of magnetic field tube diffuses along the horizontal direction. This is mostly due to the selection of *tvdlf* as the Riemann solver.

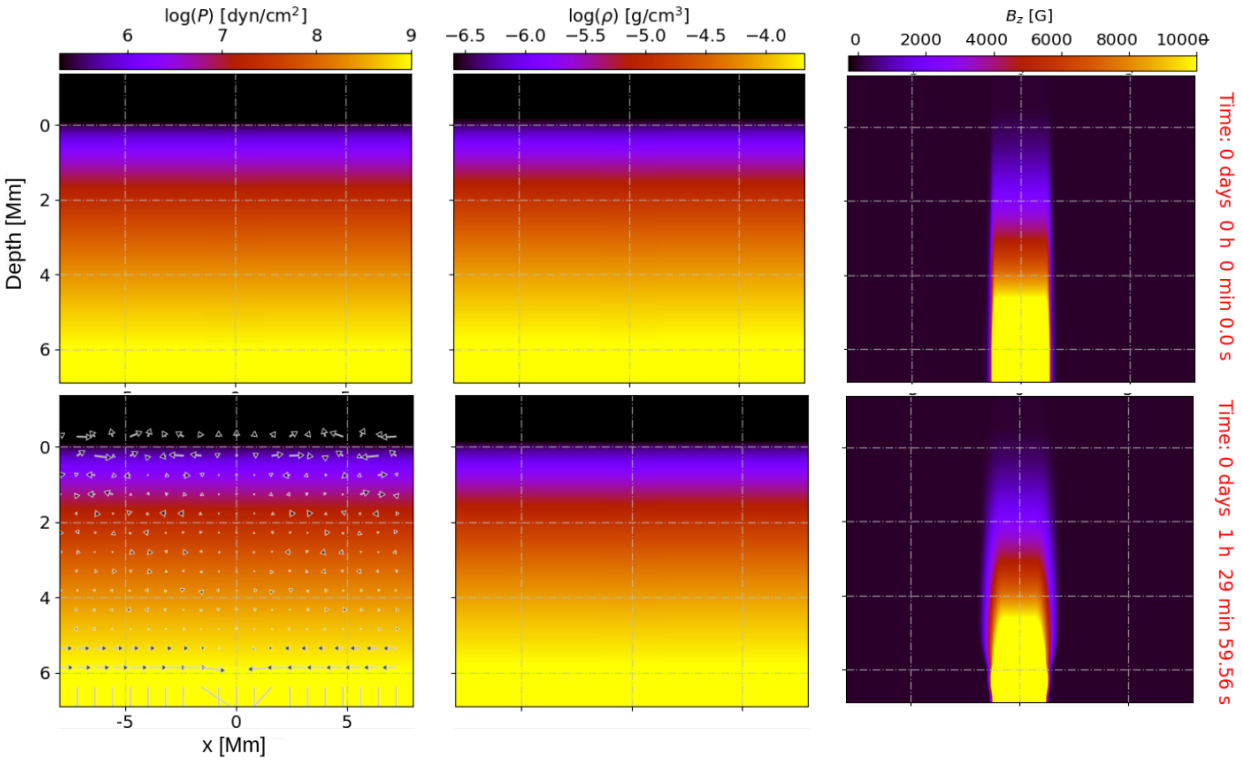

Figure **5-4**.: Pressure, density and magnetic field for the first trial. The box has spatial resolutions of 53.33 km/pix in a horizontal direction and 31.33 km/pix in the vertical one.

Pressure perturbation

In a second trial, we induce a pressure perturbation in the non-magnetic region of the simulation domain. For this scheme, the horizontal extent is increased respect to trial one to cover a larger area to contrast with theoretical wave-paths. The vertical depth, however, is kept the same. The perturbation has an ellipsoidal shape whose temporal profile (the pulse itself) behave as a gaussian function with FWHM of 0.01 s with a maximum peak of 0.005% the mean pressure at the site of the pulse.

Figure **5-5** shows the wavefront after a perturbation has been triggered in a depth $z = 1$ Mm below the solar surface at 01:00:09. The white arrows in the top row indicate the place of the induced perturbation in running velocity maps. The arrows in the bottom row mark the location of the strongest wavefront component, headed toward the photosphere, in a time of 70 s after the transient.

The time-distance diagram in the left of Figure **5-6** shows the calculations of the wave travel across the layer $z = 0$ Mm. An evident wave propagation is seen as the lower *ripple*. Succeeding wave travels are also observed as the upper weaker ripples. In the right panel the overplotted theoretical ray-path approximation shows to have a one-to-one correspondence with the first disturbance.

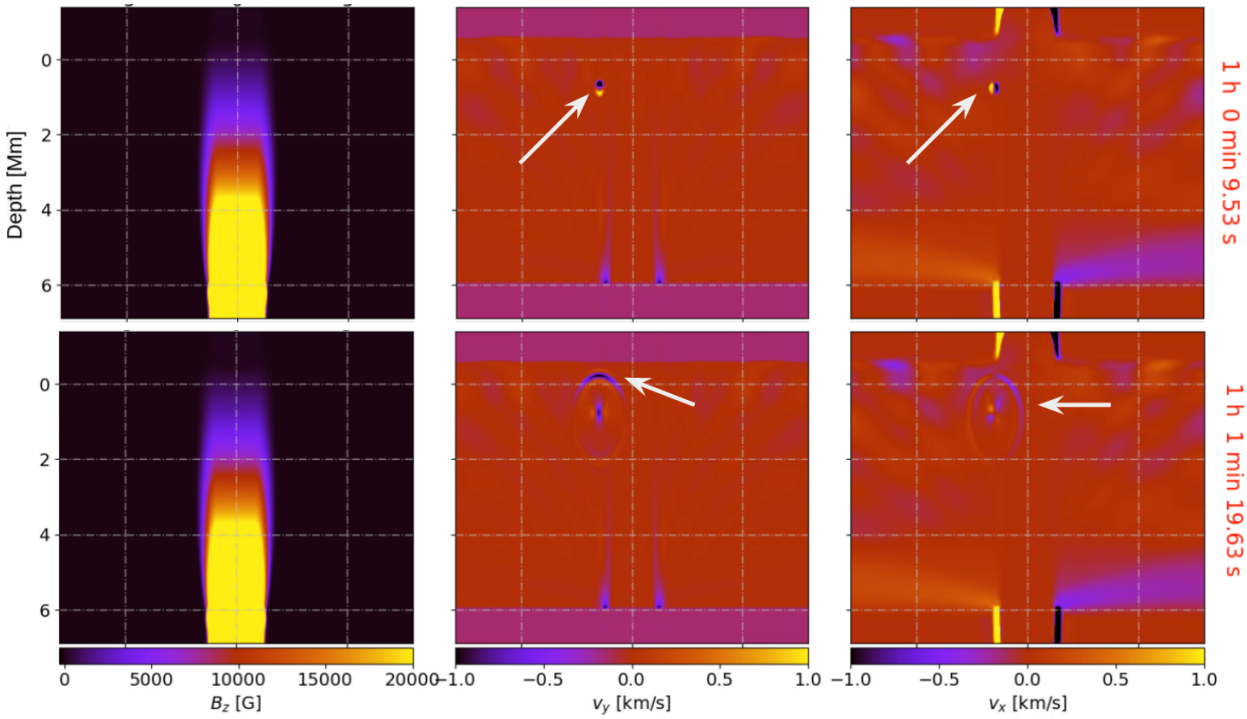

Figure **5-5**.: Pressure perturbation at $z = 1$ Mm. Columns 2 and 3 denote the velocity, measured in km/s in the vertical and horizontal directions, respectively. The top row stands for the time of the perturbation, showing the wavefronts 70 s later in the bottom row.

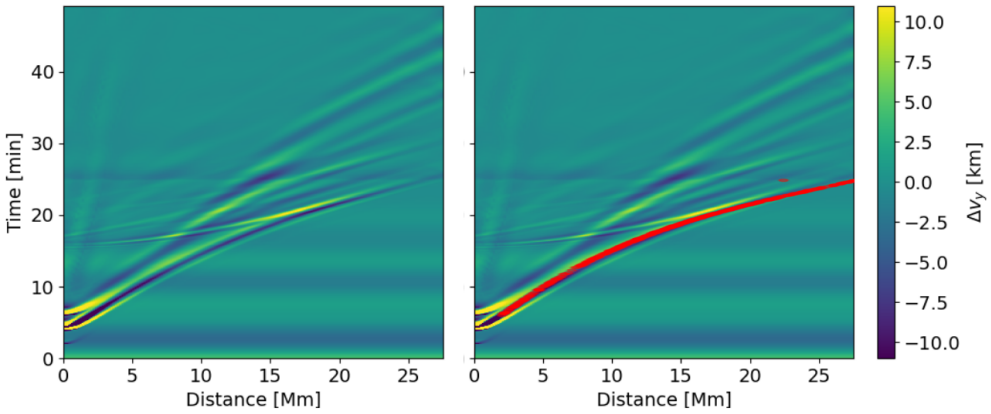

Figure **5-6**.: Time-distance diagram of the perturbed wave. The red dotted line indicate the theoretical value according to the ray-path approximation.

Magnetic perturbation

With the two tests properly ran, we now proceed to add small perturbations in the magnetic flux tube to check seismic emissions.

The new simulation grid is now 400 pixels height and 500 pixels width, spanning [-8,8] Mm in

the horizontal direction and [-10,1.4] Mm in the vertical one. This translates into an effective resolution of 32 km/pix in coordinate x and 28.5 km/pix in the z one. In this configuration, we consider two separate magnetic field perturbations to the thermodynamical structure of the solar interior. The first one corresponds to a circle-like shape with a gaussian pulse located at $z = 1$ Mm beneath the solar interior. The maximum magnetic field change of the Gaussian correspond to 0.01% the value of the mean magnetic field at that depth. The second perturbation is located 500 km deeper, at $z = 1.5$ Mm, whose shape is now an ellipse with the major axis aligned parallel to the axis of the tube. The associated maximum of the Gaussian pulse change is 0.005% the mean magnetic field, which is the half value of the circle-like transient. Both of these pulses have a duration of 0.01 s.

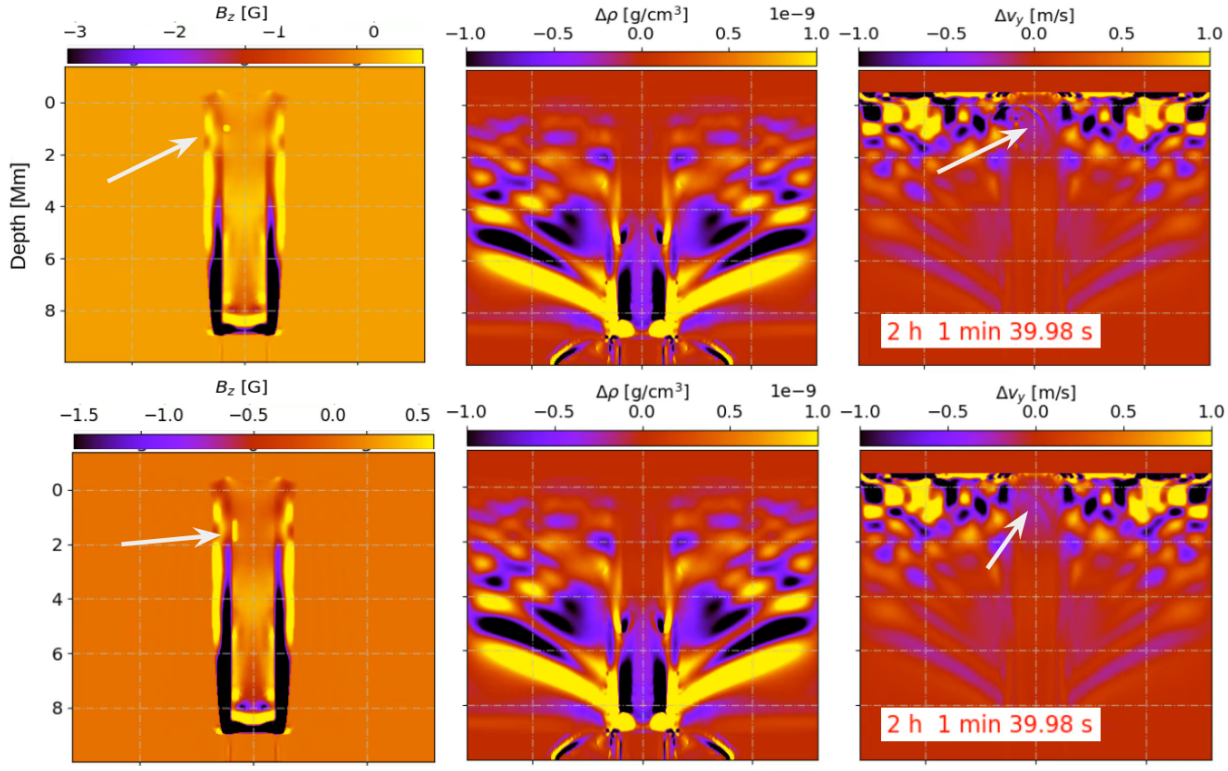

Figure **5-7**.: Magnetic field perturbations at two different depths $z = 1$ and $z = 1.5$ Mm beneath the photosphere. These pulses cause the wavefronts of the third column approximately ninety seconds after the trigger. The second column shows difference maps of density.

The first column of Figure 5-7 shows the action of the magnetic disturbances marked with white arrows. The two signals are located 800 km from the tube axis, where the magnetic field has an order of magnitude of $\sim 10^3$ G. ninety seconds after the transients, wavefronts are visible on running velocity maps in the vertical direction. These are shown with arrows in column 3, where the first pulse is the most conspicuous.

It is also noticeable the almost total suppression of the vertical and horizontal flows inside the magnetic flux tube, except for shallower regions were the wavefronts have its maximum

amplitude and the magnitude of the magnetic field is smaller. Density changes in deep layers of column two show strong variations. This is, however, a consequence of the choice of the bottom layers and does not have significance in the wave propagated perturbations.

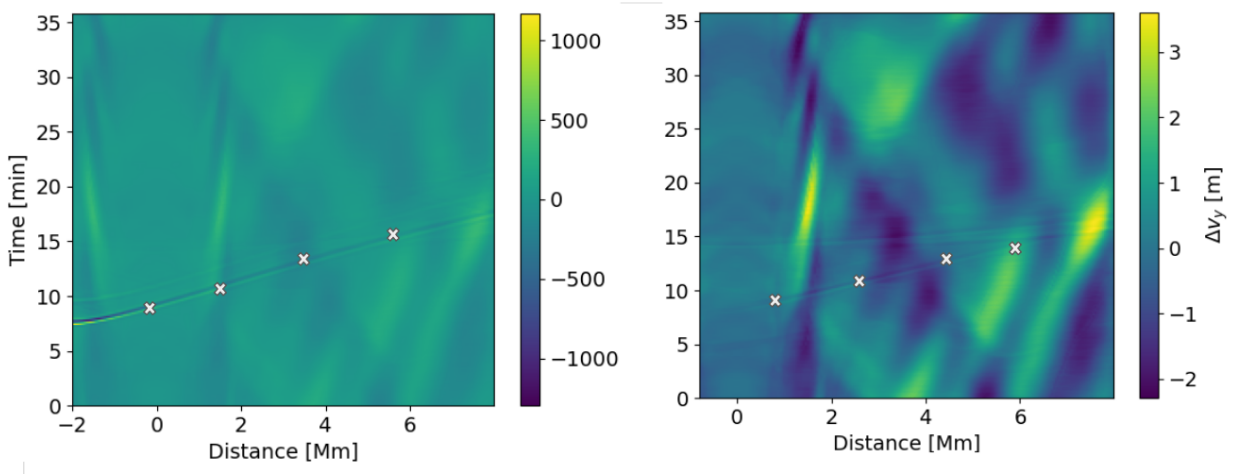

Figure **5-8**.: Time-distance diagrams for the wavefronts detected in column 3 of 5-7. White crosses follow the path of the wavefront in both diagrams.

Figure 5-8 represents the calculated time distance diagrams for these two magnetic instabilities. The greater one (the one in top row of Figure 5-7, mapped in the left) shows a significant wave traveling in the plane $z = 0$ Mm. The colorbar has been set to the velocity range [-1200,1100] m/s. The right diagram shows its counterpart for the second perturbation. The wavefront is not as visible as the shallower perturbation, though in travel have similar with a close related appearance. The white crosses are guides following the path of the wavefront.

5.3.2. 3D structure

Additionally, we set the geometry to perform a 3D version of the simulation. In this setup, we select a *CYLINDRICAL* coordinate system in which the flux tube is directed along the z-coordinate. The selected dimensions span 12 Mm in the radial direction in 128 pixels, 48 pixels in the full azimuthal direction, and 11.4 Mm in 256 pixels in the vertical component. This results in resolutions of 93.75 km/pix, 7.5°/pix, and 44.53 km/pix along ρ, ϕ and z, respectively. To save computational time, near the pole axis at $\rho = 0$, we employ the ring average technique, in which the variables near the poles are averaged in groups specified by an integer power of two. The boundary conditions at the top walls are maintained the same. The magnetic field disturbance is selected to have an elliptical shape with a similar Gaussian profile as in the 2-dimensional case. The strength of the perturbation is the mean value of the magnetic field as in the runs above. However, the vertical extent covert almost a Mm with center at $z = 1.5$ Mm and a radius $\rho = 800$ km from the center of the z-axis.

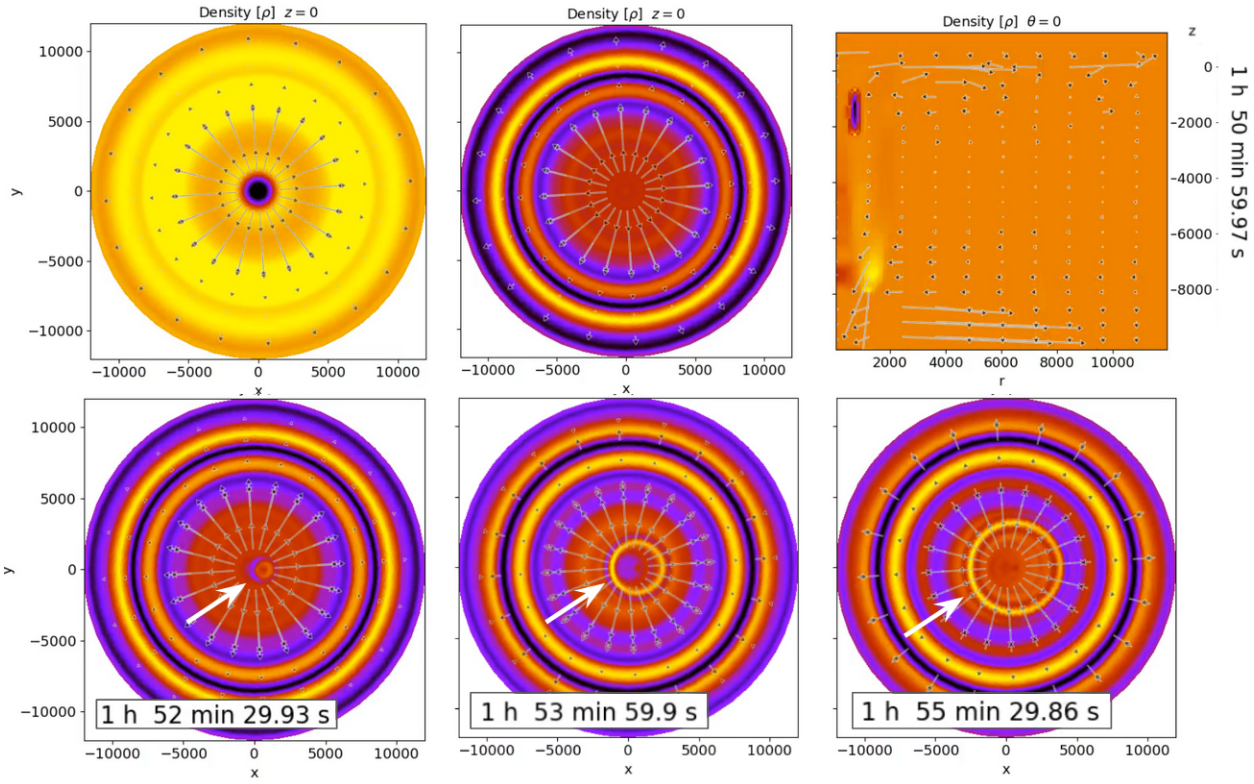

Figure **5-9**.: Magnetic field perturbation for the 3 dimensional configuration. The third image of the top row is the profile view of the perturbation, while the rest represent a top view of the region. The middle image of the top row represents the consecutive difference of the density as well as for the images in the bottom row. The arrows on the bottom row mark the position of the wavefront triggered by the disturbance as succeeding snapshots.

Figure 5-9 represent the results of this configuration. The top row indicate the disturbance onset at 01:51:00 provided as density maps. The first column indicates the density scaled to $\sim[8.8,9.5]\times10^{-8}$ g/cm^3. The second column of top row is the consecutive density difference. These densities, as well as the ones presented in the bottom row, are cuts at $z = 0$ Mm. The concentric rings centered at $r = 0$ in the difference maps relate to horizontal flows in the radial direction from the magnetic tube and has no significant relevance in the triggered action. The third column is the vertical profile of the density difference map for $\phi = 0°$. It indicates the location of the transient inside the magnetic field tube, which is more prominent than the 2 dimensional case due to its larger extent. The bottom frames show, successively, snapshots taken every 90 s of the wave propagation into the surface. It propagates radially outward from the projection of the perturbation in $z = 0$ Mm with a very prominent signature.

Discussion

Using the numerical code PLUTO we embedded a magnetic flux tube into the Solar standard model of Christensen-Dalsgaard (Christensen-Dalsgaard et al., 1996). The magnetic model considered a axisymmetric poloidal self-similar structure of the field tube according to Moradi et al. (2010). Here we did not deal with the anchoring problem associated to magnetic fluxes in deeper regions of the solar interior. Instead, we considered a constant cross-sectional structure of the flux tube with increasing depth as we go only as far to simulate transients and its wave disturbances in the photosphere.

To test the physical/numerical setup we first induced a 2 dimensional pressure perturbation to contrast pressure driven waves and its signatures on the solar surface. For this purpose, a Gaussian shallow perturbation is set in regions outside the magnetic tube, into Model S. The time-distance diagrams of Figure **5-6** agree with what is the first bounce of theoretical ray-path approximation.

The inclusion of a magnetic disturbance leads to the 2-dimensional signatures included in Figures **5-7** and the 3-dimensional one in Figure **5-9**. These setups considered several perturbations in the magnetic field tube at different depths below the surface. The trigger of the magnetic pulses followed a temporal Gaussian profile whose maximum perturbed value was given by some fraction of the magnetic field at such depth.

From the 2-dimensional magnetic perturbation it was possible to observe wave signatures traveling outwardly from the site of the transient. White crosses in Figure **5-7** denote similar travels for the two configurations with different depths as observed by running differences in the vertical direction in a manner similar to what is done with Line – of – Sight HMI Dopplergrams. The wave profile has a similar profile to the ray-path approximation in the 2-6 Mm range.

In the case of a 3-dimensional structure, a similar wave signature was appreciable in the density maps of Figure **5-9**. It is also important to note that these magnetically generated waves are not suppressed in any of the magnetic and background regions as seen in the bottom row of **5-9**, propagating isotropically from the source region in a horizontal plane until it diminishes approximately in 6 Mm.

These two numerical implementations showed, as a first approximation, how the waves emanated from magnetic disturbances in the magnetic structure. To perform most realistic simulations, non-ideal effects related to the magnetized solar interior should be included as well as improvements in spatial resolution of the computational grid. This undoubtedly would increase the simulation time, requiring greater machine capabilities, an issue left for further studies.

6. Conclusions

This work focused on the generation and detectability of subphotospheric acoustic sources associated to seismic events detected in the past solar cycle 24^{th}. At the present, mechanisms related to solar atmospheric phenomena have been proposed to account for seismic signatures observable in the solar surface. We propose an embedded mechanism in the solar interior closely related to the storage of magnetic energy in it.

In chapter 4, using acoustic holographic source density reconstructions applied to HMI Dopplergrams (chapter 3), we detected ultra-impulsive signatures for the solar flare SOL2011-07-30T02:09 M9.3 (Martínez et al., 2020). This is the second flare we know of to have such seismic signatures after the one found by Zharkov et al. (2011) for the solar flare SOL1012-02-15T01:56 X2.2. The detectability at 10 ± 1 mHz lies in the spectral limit of the Nyquist frequency of the HMI instrument, whose temporal cadence of 45 s results in a maximum sampling frequency of about 11.1 mHz. It is likely that equivalent seismic signatures at even higher frequencies can be retrieved, and that 11 mHz is not the upper limit.

Additionally we report three more ultra impulsive conspicuous signatures for M1.3, M1.8 and M6.1 class solar flares from NOAA 11515. The existence of acoustic transient sources with spectral counterpart at $9 - 11$ mHz opens numerous possibilities in the study of flare seismology: according to the analogous we have in familiar lens optics, observations at high frequencies ensures a better spatial resolution to discriminate smaller, diffraction-limited features in the solar environment of acoustic sources; at 10 ± 1 mHz, the diffraction limit is $\sim$760 km, which is somewhat finer than the one usually seen at 6 ± 1 mHz.

For each of the detected events, we found multiple layers where these acoustic transients can potentially drive seismic sources signatures (Lindsey et al., 2020). For this purpose, we used the focus-defocus technique of computational acoustic holography at the new 10 ± 1 mHz bandwidth in which the field extrapolations were applied over sequentially different depths below the solar surface; we recall that acoustic sources detected over greater depths can refer to defocused images of a same shallower source, thus the importance of the focus-defocus techinque. The results of the extrapolations allowed to discriminate embedded sources in depths with order of magnitude of megameters for the analyzed events. In this scope, we propose a mechanism in which there is a compact, subphotospheric confined region with potentially free magnetic energy capable to drive a sunquake after the action of *some* trigger with succeeding energy conversion from magnetic to acoustic. The existence of deep sources

opens additional prospects in the study of the behavior of the main mechanisms beyond the release of acoustic transients and its relationship with the solar structure.

We developed an ideal 2D/3D magnetohydrodynamical simulation to test this hypothesis of whether a perturbation in the subphotospheric magnetic field structure is able to drive an acoustic transient. We selected different setups in order to contrast the differences between wave travel across the photosphere. Here, we embedded a 2 dimensional self-similar magnetic field according to Moradi et al. (2010) into a 2D and 3D background model whose vertical dependence given by the solar standard model, Model S of Christensen-Dalsgaard et al. (1996). The disturbances had a Gaussian temporal profile with a maximum perturbation values of about 0.01% the mean magnetic field magnitude at said depths. The results of the numerical simulations show the possibility to drive solar quakes followed after perturbations in the magnetic flux tube, signatures of which depend on the depth and strength of the perturbation. Simulations including non-ideal MHD effects along with an increase in spatial resolution are left for further studies. The goal of the simulation was as a first approximation to test the hypothesis stated in Chapter 4 about the appearance and generation of seismic signatures of deeply immersed magnetic sources.

We demonstrated that it is possible for a submerged source embedded in magnetohydrodynamical conditions to drive acoustic signatures. This represents only the beginning of new prospects in the field of solar seismology and asteroseismology at the National Astronomical Observatory.

A. Acoustic Holography

In this appendix we briefly discuss the acoustic holography method used to obtain the source density maps in Chapter 4.

Helioseismic holography represent a phase-coherent reconstruction of the acoustic field at any depth in the solar interior by measuring wave disturbances in the photosphere. The description of the computational method is extensively described in Lindsey et al. (1996), Lindsey and Braun (1997), Lindsey and Braun (2000), and Braun et al. (2004). Here we describe the basics of the computational method and as well as some examples from the review of Lindsey and Braun.

Basic principles

The idea of computational helioseismic holography is to extrapolate source density maps at different depths of obtain diffraction-limited images of acoustic transients. Figure **A-1** shows an example of its direct application.

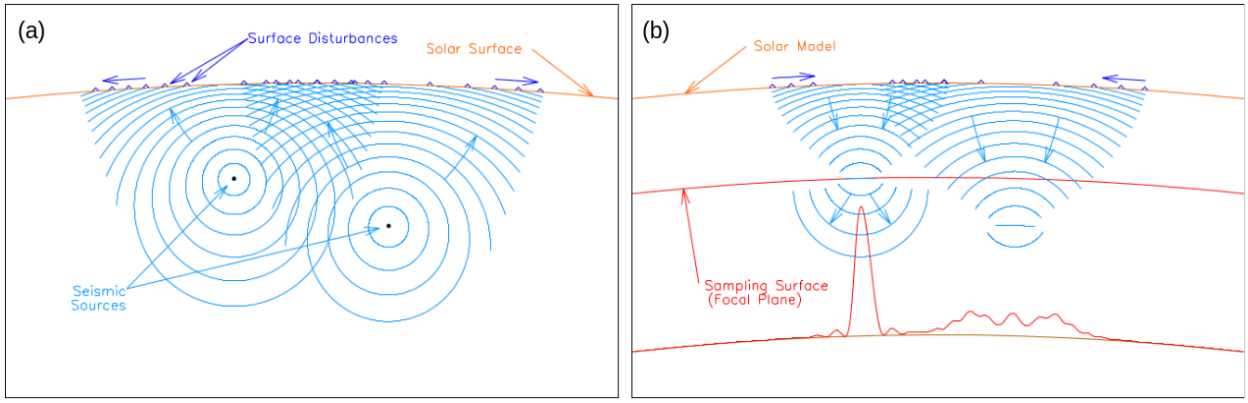

Figure **A-1**.: Panel (a): deep seismic signatures with its corresponding wavefront surface disturbances seen as ripples. Panel (b): Computational acoustic holography with the focal plane at a depth of the shallower source, showing a diffraction-limited image of the source. Image taken from Lindsey (2017).

Panel (a) of Figure **A-1** shows two seismic sources, left and right, immersed in the solar interior. These two seismic signatures emit waves whose propagation rules are given by the

how acoustic waves propagate in a solar standard medium. Part of the wavefronts reach the photosphere with visible surface disturbances propagating outwardly from the sites of the onset of the embedded sources. Panel (b) shows the field extrapolation at a depth where the shallower source is located. In the following, the plane at which field extrapolations are calculated is referred as the focal plane, in analogy to electromagnetic optics. The bottom plot of panel (b) illustrates how the seismic signatures are mapped in the focal plane; instead of getting a sharp pulse shape, the left seismic signature is presented as a diffraction-limited image. In fact, it is even possible to identify the right signature as a defocused image, though the focal plane is located far above it.

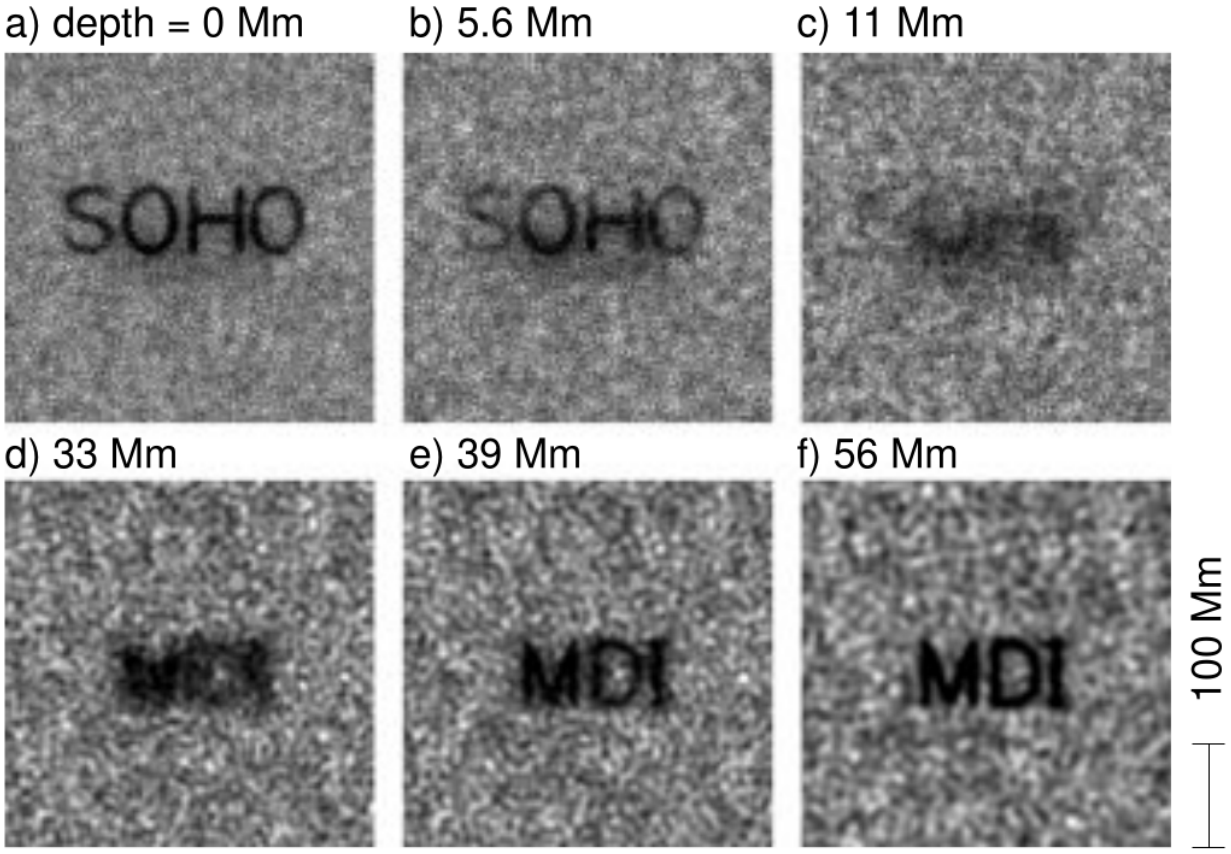

Figure **A-2**.: Focus-defocus diagnostic applied to the case of alphabetic characters at different depths.

This techinque applies the basic concepts of electromagnetic wave optics to solar oscillations: in a similar way our eyes perceive and recreate source images of electromagnetical ripples arriving the cornea, computational holography reconstruct images of the sources of acoustic radiation by measuring mechanical ripples on the solar surface. The biological task in this sense is accomplished by lenses. The helioseismic holography method calculates in time reverse the seismic source from taking its surface signatures following a model of acoustic wave propagation in a solar model back to the locations from where the source emanated.

To discriminate images in layers beneath the solar surface, helioseismic holography employs a focus-defocus diagnostic. It consists of consecutively lower the focal plane aiming to identify a focused diffraction-limited source. Figure **A-2** shows an example of progressively extrapolate the acoustic map to different depths until the different alphabetic characters focus. It is noticeable how the lowering the focal plane defocuses the word "SOHO" into a blurred shape at the midpoint, focusing after in the word "MDI" whose acoustic signature was set at 56 Mm.

Computational task

The main computational purpose is to compute a quantity called the "acoustic egression", H. The acoustic egression refers to a coherent reconstruction of the acoustic field emanated at some point beneath the surface where the focal plane is set. The egression takes the form:

$$H_+(\boldsymbol{r}, z, t) = \int dt' \int_{a<|\boldsymbol{r}-\boldsymbol{r}'|<b} d^2\boldsymbol{r} G_+(|\boldsymbol{r}-\boldsymbol{r}'|, z, t-t_0)\Phi(\boldsymbol{r}', t_0), \tag{A-1}$$

where the Green's function $G_+(|\boldsymbol{r}-\boldsymbol{r}'|, z, t-t_0)$ relates to the wave travel from the surface to $(\boldsymbol{r}, z, t)$. The travel time of an acoustic source wave is:

$$T(r, z) = \int_{\Gamma(r,z)} \frac{ds}{c(z)} \tag{A-2}$$

with $\Gamma(r, z)$ being the travel path which represents the path of minimum energy of the propagation.

In the spatial integral of equation A-1, an annulus region of integration has been selected. This region is called the *pupil* and represents the place in which holographic calculations are performed. The election of this annular pupil has to do with reasons regarding the type of signature to be observed. There are two main vantage points to be considered, the subjacent and the superjacent vantage holography. In the subjacent vantage, waves emanating radially outward refract as a result of increase in the sound speed with depth, and then reflect into the outlying pupil of observation. With this setup, the inner radius of the pupil is much larger than the depth at which calculations are being made. On the other had, if we wanted to study acoustic disturbances from sources whose acoustic source travels directly upward, a superjacent vantage would be required.

Additional aberrations regarding the projection of the curvature of the solar surface into a plane are taken into account. They depend on the extent of the pupil and some of them can not be completely removed if it has a great radius of integration.

Figure **A-3** encompasses the similitude between the acoustic holographic method and the electromagnetic optics as seen by a lens. Rays with certain inclination propagate into the

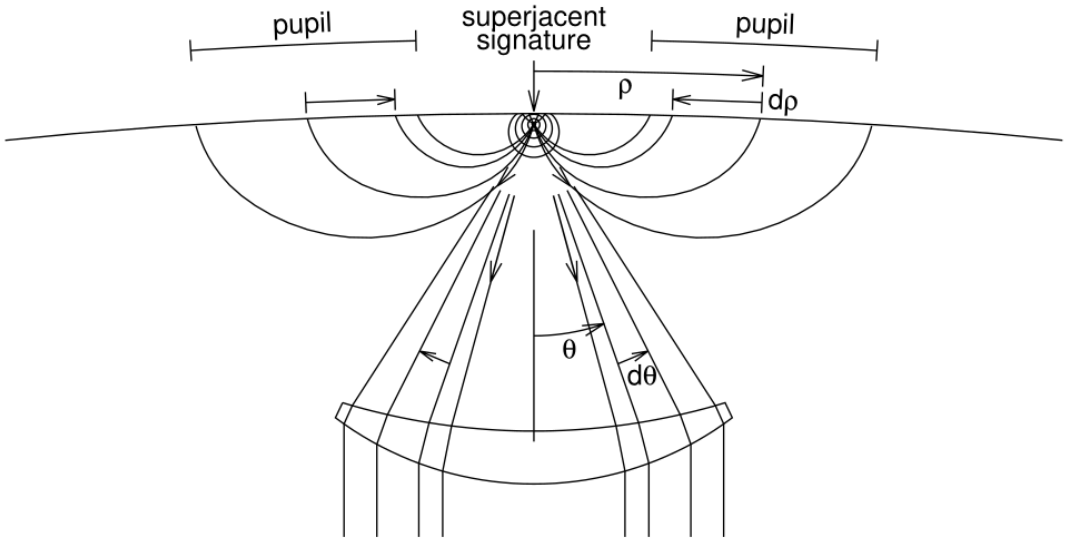

Figure **A-3**.: Sujacent signature of a disturbed source in the solar interior. The superadjacent vantage is included if inference of the source field for a direct upward propagation is required.

solar interior to be then refract back to the surface into the pupil. In the analogous, it is represented as a lens whose angle of illumination, the aperture θ, is given by the inner radius of the pupil. Images in the lenses focuses at the focal point or depth of observation. If the extrapolations are made for deeper layers, this would correspond to lower the optical lens.

A numerical example of this application is seen in Figure **2-3**. For the document, a subjacent perspective is used to extrapolate the source density egression maps.

Bibliography

Conny Aerts, Jørgen Christensen-Dalsgaard, and Donald W. Kurtz. *Asteroseismology*. 2010.

J. D. Alvarado-Gómez, J. C. Buitrago-Casas, J. C. Martínez-Oliveros, C. Lindsey, H. Hudson, and B. Calvo-Mozo. Magneto-Acoustic Energetics Study of the Seismically Active Flare of 15 February 2011. *Solar Phys.*, 280(2):335–345, October 2012. doi: 10.1007/s11207-012-0009-6.

John N. Bahcall, Aldo M. Serenelli, and Sarbani Basu. New Solar Opacities, Abundances, Helioseismology, and Neutrino Fluxes. *Astrophys. J. Lett.*, 621(1):L85–L88, March 2005. doi: 10.1086/428929.

Sarbani Basu. Global seismology of the Sun. *Living Reviews in Solar Physics*, 13(1):2, August 2016. doi: 10.1007/s41116-016-0003-4.

Arnold O. Benz. Flare Observations. *Living Reviews in Solar Physics*, 14(1):2, December 2017. doi: 10.1007/s41116-016-0004-3.

D. C. Braun. Scattering of p-Modes by Sunspots. I. Observations. *Astrophys. J.*, 451:859, October 1995. doi: 10.1086/176272.

D. C. Braun, Jr. Duvall, T. L., and B. J. Labonte. Acoustic Absorption by Sunspots. *Astrophys. J. Lett.*, 319:L27, August 1987. doi: 10.1086/184949.

D. C. Braun, Jr. Duvall, T. L., B. J. Labonte, S. M. Jefferies, J. W. Harvey, and M. A. Pomerantz. Scattering of p-Modes by a Sunspot. *Astrophys. J. Lett.*, 391:L113, June 1992. doi: 10.1086/186410.

D. C. Braun, A. C. Birch, and C. Lindsey. Local Helioseismology of Near-Surface Flows. In D. Danesy, editor, *SOHO 14 Helio- and Asteroseismology: Towards a Golden Future*, volume 559 of *ESA Special Publication*, page 337, October 2004.

J. C. Buitrago-Casas, J. C. Martínez Oliveros, C. Lindsey, B. Calvo-Mozo, S. Krucker, L. Glesener, and S. Zharkov. A Statistical Correlation of Sunquakes Based on Their Seismic and White-Light Emission. *Solar Phys.*, 290(11):3151–3162, November 2015. doi: 10.1007/s11207-015-0786-9.

R. H. Cameron, L. Gizon, H. Schunker, and A. Pietarila. Constructing Semi-Empirical Sunspot Models for Helioseismology. *Solar Phys.*, 268(2):293–308, February 2011. doi: 10.1007/s11207-010-9631-3.

H. Carmichael. *A Process for Flares*, volume 50, page 451. 1964.

R. C. Carrington. Description of a Singular Appearance seen in the Sun on September 1, 1859. *Mon. Not. Roy. Astron. Soc.*, 20:13–15, November 1859. doi: 10.1093/mnras/20.1.13.

J. S. Castellanos Durán, L. Kleint, and B. Calvo-Mozo. A Statistical Study of Photospheric Magnetic Field Changes During 75 Solar Flares. *Astrophys. J.*, 852(1):25, January 2018. doi: 10.3847/1538-4357/aa9d37.

Subrahmanyan Chandrasekhar. *Radiative transfer*. 1960.

Christensen-Dalsgaard. Lecture Notes on Stellar Oscillations, Fifth Edition. January 2014. URL https://users-phys.au.dk/jcd/oscilnotes/Lecture_Notes_on_Stellar_Oscillations.pdf.

J. Christensen-Dalsgaard, D. Gough, and J. Toomre. Seismology of the Sun. *Science*, 229 (4717):923–931, September 1985. doi: 10.1126/science.229.4717.923.

J. Christensen-Dalsgaard, W. Dappen, S. V. Ajukov, E. R. Anderson, H. M. Antia, S. Basu, V. A. Baturin, G. Berthomieu, B. Chaboyer, S. M. Chitre, A. N. Cox, P. Demarque, J. Donatowicz, W. A. Dziembowski, M. Gabriel, D. O. Gough, D. B. Guenther, J. A. Guzik, J. W. Harvey, F. Hill, G. Houdek, C. A. Iglesias, A. G. Kosovichev, J. W. Leibacher, P. Morel, C. R. Proffitt, J. Provost, J. Reiter, Jr. Rhodes, E. J., F. J. Rogers, I. W. Roxburgh, M. J. Thompson, and R. K. Ulrich. The Current State of Solar Modeling. *Science*, 272(5266):1286–1292, May 1996. doi: 10.1126/science.272.5266.1286.

Jørgen Christensen-Dalsgaard. Helioseismology. *Reviews of Modern Physics*, 74(4):1073–1129, November 2002. doi: 10.1103/RevModPhys.74.1073.

Sébastien Couvidat, S. P. Rajaguru, Richard Wachter, K. Sankarasubramanian, Jesper Schou, and Philip H. Scherrer. Line-of-Sight Observables Algorithms for the Helioseismic and Magnetic Imager (HMI) Instrument Tested with Interferometric Bidimensional Spectrometer (IBIS) Observations. *Solar Phys.*, 278(1):217–240, May 2012a. doi: 10.1007/s11207-011-9927-y.

Sébastien Couvidat, Jesper Schou, Richard A. Shine, Rock I. Bush, John W. Miles, Philip H. Scherrer, and Richard L. Rairden. Wavelength Dependence of the Helioseismic and Magnetic Imager (HMI) Instrument onboard the Solar Dynamics Observatory (SDO). *Solar Phys.*, 275(1-2):285–325, January 2012b. doi: 10.1007/s11207-011-9723-8.

Margarida S. Cunha. Theory of Stellar Oscillations. In Tiago L. Campante, Nuno C. Santos, and Mário J. P. F. G. Monteiro, editors, *Asteroseismology and Exoplanets: Listening to the Stars and Searching for New Worlds*, volume 49, page 27, January 2018. doi: 10.1007/978-3-319-59315-9_2.

A. C. Donea and C. Lindsey. Seismic Emission from the Solar Flares of 2003 October 28 and 29. *Astrophys. J.*, 630(2):1168–1183, September 2005. doi: 10.1086/432155.

A. C. Donea, D. C. Braun, and C. Lindsey. Seismic Images of a Solar Flare. *Astrophys. J. Lett.*, 513(2):L143–L146, March 1999. doi: 10.1086/311915.

Jr. Duvall, T. L. A dispersion law for solar oscillations. *Nature*, 300(5889):242–243, November 1982. doi: 10.1038/300242a0.

Jr. Duvall, T. L., S. M. Jefferies, J. W. Harvey, and M. A. Pomerantz. Time-distance helioseismology. *Nature*, 362(6419):430–432, April 1993. doi: 10.1038/362430a0.

A. S. Eddington. *The Internal Constitution of the Stars*. 1926.

G. H. Fisher, D. J. Bercik, B. T. Welsch, and H. S. Hudson. Global Forces in Eruptive Solar Flares: The Lorentz Force Acting on the Solar Atmosphere and the Solar Interior. *Solar Phys.*, 277(1):59–76, March 2012. doi: 10.1007/s11207-011-9907-2.

L. Fletcher, B. R. Dennis, H. S. Hudson, S. Krucker, K. Phillips, A. Veronig, M. Battaglia, L. Bone, A. Caspi, Q. Chen, P. Gallagher, P. T. Grigis, H. Ji, W. Liu, R. O. Milligan, and M. Temmer. An Observational Overview of Solar Flares. *Space Sci. Rev.*, 159(1-4): 19–106, September 2011. doi: 10.1007/s11214-010-9701-8.

Laurent Gizon and Aaron C. Birch. Local Helioseismology. *Living Reviews in Solar Physics*, 2(1):6, December 2005. doi: 10.12942/lrsp-2005-6.

Kolja Glogowski, Monica G. Bobra, Nitin Choudhary, Arthur B. Amezcua, and Stuart J. Mumford. drms: A python package for accessing hmi and aia data. *Journal of Open Source Software*, 4(40):1614, 2019. doi: 10.21105/joss.01614. URL https://doi.org/10.21105/joss.01614.

Peter Goldreich, Norman Murray, and Pawan Kumar. Excitation of Solar p-Modes. *Astrophys. J.*, 424:466, March 1994. doi: 10.1086/173904.

D. O. Gough. Theory of Solar Oscillations. In Erica Rolfe and Bruce Battrick, editors, *Future Missions in Solar, Heliospheric & Space Plasma Physics*, volume 235 of *ESA Special Publication*, page 183, June 1985.

D. O. Gough and M. J. Thompson. *The inversion problem.*, pages 519–561. 1991.

D. O. Gough and J. Toomre. On the Detection of Subphotospheric Convective Velocities and Temperature Fluctuations. *Solar Phys.*, 82(1-2):401–410, Jan 1983. doi: 10.1007/BF00145579.

Frank Hill. Rings and Trumpets—Three-dimensional Power Spectra of Solar Oscillations. *Astrophys. J.*, 333:996, October 1988. doi: 10.1086/166807.

T. Hirayama. Theoretical Model of Flares and Prominences. I: Evaporating Flare Model. *Solar Phys.*, 34(2):323–338, February 1974. doi: 10.1007/BF00153671.

H. S. Hudson, G. H. Fisher, and B. T. Welsch. Flare Energy and Magnetic Field Variations. In R. Howe, R. W. Komm, K. S. Balasubramaniam, and G. J. D. Petrie, editors, *Subsurface and Atmospheric Influences on Solar Activity*, volume 383 of *Astronomical Society of the Pacific Conference Series*, page 221, January 2008.

R. A. Kopp and G. W. Pneuman. Magnetic reconnection in the corona and the loop prominence phenomenon. *Solar Phys.*, 50(1):85–98, October 1976. doi: 10.1007/BF00206193.

A. G. Kosovichev. Helioseismic Response to the X2.2 Solar Flare of 2011 February 15. *Astrophys. J. Lett.*, 734(1):L15, June 2011. doi: 10.1088/2041-8205/734/1/L15.

A. G. Kosovichev and V. V. Zharkova. X-ray flare sparks quake inside Sun. *Nature*, 393 (6683):317–318, May 1998. doi: 10.1038/30629.

A. G. Kosovichev, Jr. Duvall, T. L. ˛Jr., and P. H. Scherrer. Time-Distance Inversion Methods and Results - (Invited Review). *Solar Phys.*, 192:159–176, March 2000. doi: 10.1023/A:1005251208431.

John Leibacher, Takashi Sakurai, Carolus J. Schrijver, and Lidia van Driel-Gesztelyi. Solar Observation Target Identification Convention for use in Solar Physics. *Solar Phys.*, 263 (1-2):1–2, May 2010. doi: 10.1007/s11207-010-9553-0.

Robert B. Leighton, Robert W. Noyes, and George W. Simon. Velocity Fields in the Solar Atmosphere. I. Preliminary Report. *Astrophys. J.*, 135:474, March 1962. doi: 10.1086/147285.

James R. Lemen, Alan M. Title, David J. Akin, Paul F. Boerner, Catherine Chou, Jerry F. Drake, Dexter W. Duncan, Christopher G. Edwards, Frank M. Friedlaender, Gary F. Heyman, Neal E. Hurlburt, Noah L. Katz, Gary D. Kushner, Michael Levay, Russell W. Lindgren, Dnyanesh P. Mathur, Edward L. McFeaters, Sarah Mitchell, Roger A. Rehse, Carolus J. Schrijver, Larry A. Springer, Robert A. Stern, Theodore D. Tarbell, Jean-Pierre Wuelser, C. Jacob Wolfson, Carl Yanari, Jay A. Bookbinder, Peter N. Cheimets, David Caldwell, Edward E. Deluca, Richard Gates, Leon Golub, Sang Park, William A. Podgorski, Rock I. Bush, Philip H. Scherrer, Mark A. Gummin, Peter Smith, Gary Auker,

Paul Jerram, Peter Pool, Regina Soufli, David L. Windt, Sarah Beardsley, Matthew Clapp, James Lang, and Nicholas Waltham. The Atmospheric Imaging Assembly (AIA) on the Solar Dynamics Observatory (SDO). *Solar Phys.*, 275(1-2):17–40, January 2012. doi: 10.1007/s11207-011-9776-8.

C. Lindsey and D. C. Braun. Helioseismic Holography. *Astrophys. J.*, 485(2):895–903, August 1997. doi: 10.1086/304445.

C. Lindsey and D. C. Braun. Acoustic Signatures of Subphotospheric Structure Underlying Sunspots. *Astrophys. J. Lett.*, 509(2):L129–L132, December 1998. doi: 10.1086/311766.

C. Lindsey and D. C. Braun. Basic Principles of Solar Acoustic Holography - (Invited Review). *Solar Phys.*, 192:261–284, March 2000. doi: 10.1023/A:1005227200911.

C. Lindsey, D. C. Braun, S. M. Jefferies, M. F. Woodard, Y. Fan, Y. Gu, and S. Redfield. Doppler Acoustic Diagnostics of Subsurface Solar Magnetic Structure. *Astrophys. J.*, 470: 636, October 1996. doi: 10.1086/177895.

Charles Lindsey. Helioseismology Presentation, Curso de Astrofísica 2017-I, Observatorio Astronómico Nacional, Universidad Nacional de Colombia. January 2017.

Charles Lindsey and Douglas C. Braun. Helioseismic Imaging of Sunspots at Their Antipodes. *Solar Phys.*, 126(1):101–115, March 1990. doi: 10.1007/BF00158301.

Charles Lindsey, J. C. Buitrago-Casas, Juan Carlos Martínez Oliveros, Douglas Braun, Angel D. Martínez, Valeria Quintero Ortega, Benjamín Calvo-Mozo, and Alina-Catalina Donea. Submerged Sources of Transient Acoustic Emission from Solar Flares. *Astrophys. J. Lett.*, 901(1):L9, September 2020. doi: 10.3847/2041-8213/abad2a.

D. Lynden-Bell and J. P. Ostriker. On the stability of differentially rotating bodies. *Mon. Not. Roy. Astron. Soc.*, 136:293, January 1967. doi: 10.1093/mnras/136.3.293.

Marcos E. Machado, A. Gordon Emslie, and Eugene H. Avrett. Radiative Backwarming in White-Light Flares. *Solar Phys.*, 124(2):303–317, September 1989. doi: 10.1007/BF00156272.

Angel D. Martínez, Valeria Quintero Ortega, J. C. Buitrago-Casas, Juan Carlos Martínez Oliveros, Benjamín Calvo-Mozo, and Charles Lindsey. Ultra-impulsive Solar Flare Seismology. *Astrophys. J. Lett.*, 895(1):L19, May 2020. doi: 10.3847/2041-8213/ab9173.

J. C. Martínez-Oliveros and A. C. Donea. Magnetic field variations and seismicity of solar active regions. *Mon. Not. Roy. Astron. Soc.*, 395(1):L39–L42, May 2009. doi: 10.1111/j.1745-3933.2009.00637.x.

J. C. Martínez-Oliveros, H. Moradi, and A. C. Donea. Seismic Emissions from a Highly Impulsive M6.7 Solar Flare. *Solar Phys.*, 251(1-2):613–626, September 2008. doi: 10.1007/s11207-008-9122-y.

J. C. Martínez Oliveros, C. Lindsey, H. S. Hudson, and J. C. Buitrago Casas. Transient Artifacts in a Flare Observed by the Helioseismic and Magnetic Imager on the Solar Dynamics Observatory. *Solar Phys.*, 289(3):809–819, March 2014. doi: 10.1007/s11207-013-0358-9.

A. Mignone, G. Bodo, S. Massaglia, T. Matsakos, O. Tesileanu, C. Zanni, and A. Ferrari. PLUTO: A Numerical Code for Computational Astrophysics. *Astrophys. J. Suppl.*, 170 (1):228–242, May 2007. doi: 10.1086/513316.

A. Mignone, C. Zanni, P. Tzeferacos, B. van Straalen, P. Colella, and G. Bodo. The PLUTO Code for Adaptive Mesh Computations in Astrophysical Fluid Dynamics. *Astrophys. J. Suppl.*, 198(1):7, January 2012. doi: 10.1088/0067-0049/198/1/7.

H. Moradi, C. Baldner, A. C. Birch, D. C. Braun, R. H. Cameron, T. L. Duvall, L. Gizon, D. Haber, S. M. Hanasoge, B. W. Hindman, J. Jackiewicz, E. Khomenko, R. Komm, P. Rajaguru, M. Rempel, M. Roth, R. Schlichenmaier, H. Schunker, H. C. Spruit, K. G. Strassmeier, M. J. Thompson, and S. Zharkov. Modeling the Subsurface Structure of Sunspots. *Solar Phys.*, 267(1):1–62, November 2010. doi: 10.1007/s11207-010-9630-4.

Dermott Mullan. *Physics of the Sun*. 2009. doi: 10.1201/b15843.

Valery M. Nakariakov. Coronal waves and oscillations. In Volker Bothmer and Ahmed Abdel Hady, editors, *Solar Activity and its Magnetic Origin*, volume 233, pages 464–471, January 2006. doi: 10.1017/S174392130600250X.

W. D. Pence, L. Chiappetti, C. G. Page, R. A. Shaw, and E. Stobie. Definition of the Flexible Image Transport System (FITS), version 3.0. *Astron. Astrophys.*, 524:A42, December 2010. doi: 10.1051/0004-6361/201015362.

W. Dean Pesnell, B. J. Thompson, and P. C. Chamberlin. The Solar Dynamics Observatory (SDO). *Solar Phys.*, 275(1-2):3–15, January 2012. doi: 10.1007/s11207-011-9841-3.

David I. Pontin and Gunnar Hornig. The Parker problem: existence of smooth force-free fields and coronal heating. *Living Reviews in Solar Physics*, 17(1):5, August 2020. doi: 10.1007/s41116-020-00026-5.

F. Roddier. Principle of production of an acoustic hologram of the solar surface. *Academie des Sciences Paris Comptes Rendus Serie B Sciences Physiques*, 281(4):93–95, July 1975.

A. J. B. Russell, M. K. Mooney, J. E. Leake, and H. S. Hudson. Sunquake Generation by Coronal Magnetic Restructuring. *Astrophys. J.*, 831(1):42, November 2016. doi: 10.3847/0004-637X/831/1/42.

J. Schou, H. M. Antia, S. Basu, R. S. Bogart, R. I. Bush, S. M. Chitre, J. Christensen-Dalsgaard, M. P. Di Mauro, W. A. Dziembowski, A. Eff-Darwich, D. O. Gough, D. A. Haber, J. T. Hoeksema, R. Howe, S. G. Korzennik, A. G. Kosovichev, R. M. Larsen, F. P. Pijpers, P. H. Scherrer, T. Sekii, T. D. Tarbell, A. M. Title, M. J. Thompson, and J. Toomre. Helioseismic Studies of Differential Rotation in the Solar Envelope by the Solar Oscillations Investigation Using the Michelson Doppler Imager. *Astrophys. J.*, 505 (1):390–417, September 1998. doi: 10.1086/306146.

J. Schou, P. H. Scherrer, R. I. Bush, R. Wachter, S. Couvidat, M. C. Rabello-Soares, R. S. Bogart, J. T. Hoeksema, Y. Liu, T. L. Duvall, D. J. Akin, B. A. Allard, J. W. Miles, R. Rairden, R. A. Shine, T. D. Tarbell, A. M. Title, C. J. Wolfson, D. F. Elmore, A. A. Norton, and S. Tomczyk. Design and Ground Calibration of the Helioseismic and Magnetic Imager (HMI) Instrument on the Solar Dynamics Observatory (SDO). *Solar Phys.*, 275 (1-2):229–259, January 2012. doi: 10.1007/s11207-011-9842-2.

Carolus J. Schrijver and George L. Siscoe. *Heliophysics: Space Storms and Radiation: Causes and Effects*. 2010.

H. Schunker, D. C. Braun, C. Lindsey, and P. S. Cally. Physical Properties of Wave Motion in Inclined Magnetic Fields within Sunspot Penumbrae. *Solar Phys.*, 251(1-2):341–359, September 2008. doi: 10.1007/s11207-008-9142-7.

Harlow Shapley. On the Nature and Cause of Cepheid Variation. *Astrophys. J.*, 40:448, December 1914. doi: 10.1086/142137.

I. N. Sharykin and A. G. Kosovichev. Dynamics of Electric Currents, Magnetic Field Topology, and Helioseismic Response of a Solar Flare. *Astrophys. J.*, 808(1):72, July 2015. doi: 10.1088/0004-637X/808/1/72.

I. N. Sharykin, A. G. Kosovichev, and I. V. Zimovets. Energy Release and Initiation of a Sunquake in a C-class Flare. *Astrophys. J.*, 807(1):102, July 2015. doi: 10.1088/0004-637X/807/1/102.

K. Shibata. Reconnection Models of Flares. In T. S. Bastian, N. Gopalswamy, and K. Shibasaki, editors, *Proceedings of the Nobeyama Symposium*, pages 381–389, December 1999.

Kazunari Shibata and Tetsuya Magara. Solar Flares: Magnetohydrodynamic Processes. *Living Reviews in Solar Physics*, 8(1):6, December 2011. doi: 10.12942/lrsp-2011-6.

E. A. Spiegel and J. P. Zahn. The solar tachocline. *Astron. Astrophys.*, 265:106–114, November 1992.

H. C. Spruit and T. J. Bogdan. The Conversion of p-Modes to Slow Modes and the Absorption of Acoustic Waves by Sunspots. *Astrophys. J. Lett.*, 391:L109, June 1992. doi: 10.1086/186409.

Michael Stix. *The Sun: An Introduction*. Astronomy and Astrophysics Library. Springer-Verlag Berlin Heidelberg, 3 edition, 2004.

P. A. Sturrock. Model of the High-Energy Phase of Solar Flares. *Nature*, 211(5050):695–697, August 1966. doi: 10.1038/211695a0.

J. J. Sudol and J. W. Harvey. Longitudinal Magnetic Field Changes Accompanying Solar Flares. *Astrophys. J.*, 635(1):647–658, December 2005. doi: 10.1086/497361.

M. Tassoul. Asymptotic approximations for stellar nonradial pulsations. *Astrophys. J.s*, 43: 469–490, August 1980. doi: 10.1086/190678.

W. T. Thompson. Coordinate systems for solar image data. *Astron. Astrophys.*, 449(2): 791–803, April 2006. doi: 10.1051/0004-6361:20054262.

Charles L. Wolff. Free Oscillations of the Sun and Their Possible Stimulation by Solar Flares. *Astrophys. J.*, 176:833, September 1972. doi: 10.1086/151680.

M. F. Woodard. Solar Subsurface Flow Inferred Directly from Frequency-Wavenumber Correlations in the Seismic Velocity Field. *Astrophys. J.*, 565(1):634–639, January 2002. doi: 10.1086/324546.

S. Zharkov, L. M. Green, S. A. Matthews, and V. V. Zharkova. 2011 February 15: Sunquakes Produced by Flux Rope Eruption. *Astrophys. J. Lett.*, 741(2):L35, November 2011. doi: 10.1088/2041-8205/741/2/L35.

S. Zharkov, L. M. Green, S. A. Matthews, and V. V. Zharkova. Properties of the 15 February 2011 Flare Seismic Sources. *Solar Phys.*, 284(2):315–327, June 2013. doi: 10.1007/s11207-012-0169-4.